50-2 MARCH 1981

Low Enrichment Fuel Evaluation and Analysis Program

Summary Report for the Period
January, 1980 - December, 1980

WILLIAM KERR, Project Director

Department of Nuclear Engineering
and the
Michigan-Memorial Phoenix Project

(8)

PROJECT PARTICIPANTS

William Kerr

John S. King

John C. Lee

William R. Martin

Reed R. Burn

Forrest B. Brown

David C. Losey

Joao Moreira

James Rathkopf

James Sheridan

Gayle Stankiewicz

John Tucker

David Wehe

Roger Wigent

TABLE OF CONTENTS

LIST OF FIGURES

LIST OF TABLES

I. INTRODUCTION

The University of Michigan Department of Nuclear Engineering and the Michigan-Memorial Phoenix Project have been engaged in a cooperative effort with Argonne National Laboratory to test and analyze low enrichment fuel in the Ford Nuclear Reactor (FNR). The effort was begun in 1979, as part of the Reduced Enrichment Research and Test Reactor (RERTR) Program, to demonstrate, on a whole-core basis, the feasibility of enrichment reduction from 93% to below 20% in MTR-type fuel designs. Testing of low enrichment uranium (LEU) fuel in the FNR core is currently scheduled to begin in September, 1981.

The key technical basis of the LEU fuel is to reduce the uranium enrichment while increasing, at the same time, the uranium loading of each fuel element in order to compensate for the reactivity loss due to the larger ^{238}U content. The required uranium loading can be achieved by increasing the uranium density in the fuel meat and by increasing the fuel volume fraction. At the same time it is necessary to insure that fuel elements operate within their thermal-hydraulic limits.

The first phase in our investigation performed in preparation for the LEU fuel testing at the FNR core included (a) initiation of development of experimental and analytical techniques applicable for neutronic evaluation of the MTR-type fuel elements, (b) selection of a LEU design for the FNR, (c) preparation of a preliminary FNR license amendment, and (d) a thermal-hydraulic testing program for the MTR-type fuel elements. These initial efforts undertaken in our LEU project are summarized in our first Annual Summary Report[1] for the year 1979.

In continuation of these initial efforts, further improvements and validation of the experimental and analytical methods were carried out in 1980. The experimental work was centered around spatial flux

measurements in and out of the core, and ex-core flux spectrum measurements. The analytic efforts included improvement of various computer codes and development of calculational models for reactivity coefficients as well as further analysis of LEU fuel designs. During the present reporting period, a series of thermal hydraulics tests were performed for the MTR-type fuel elements. Amendments to a safety analysis submitted as part of a requested license amendment to permit the use of LEU fuel in the FNR were also submitted to the U. S. Nuclear Regulatory Commission in 1980. Approval was granted in February, 1981.

Detailed papers on the experimental and analytical efforts performed under the LEU project for the FNR core were presented at the International Meeting on Development, Fabrication and Application of Reduced-Enrichment Fuels for Research and Test Reactors, held on November 12-14, 1980 at Argonne National Laboratory, and are included here as Appendices A and B. Hence, this report aims primarily at summarizing those efforts performed during 1980, which were not adequately covered in the papers, and at providing a brief review of the project status. We begin with a review of the activities related to the LEU demonstration experiments in Section II. Various efforts undertaken in support of the development and verification of the neutronic methods for generic analysis of MTR-type fuel elements are then summarized in Section III, while comparisons between the calculational results and the FNR experimental data are presented in Section IV. Design analysis of the LEU fuel and comparisons between the LEU and high enrichment uranium (HEU) fuels are presented in Section V. A review of the activities related to the FNR license amendment is then given in Section VI, followed by a summary of the thermal-hydraulics test results in Section VII. A summary of the project activities for the year 1980 and a brief review of the project status are then presented in Section VIII. In addition to Appendices A and B discussed earlier, a limited

selection of a reference cross-section library is included in Appendix C.

II. DEMONSTRATION EXPERIMENTS PROGRAM

The Demonstration Experiments Program, designed to measure the significant differences between HEU and LEU cores, was continued in order to characterize the HEU FNR core. The work performed through January of 1980 is described in the first Annual Summary Report[1]. The work performed during the period January, 1980 - December, 1980 has involved primarily the implementation and extension of the concepts developed in Reference 1. Appendix A, "The RERTR Demonstration Experiments Program at the Ford Nuclear Reactor," contains many of the results from the experiments which have been performed during the past year. These efforts, summarized below, are by no means completed and work is continuing in all areas at this time.

A. Spatial Measurements

1. Rhodium Self-Powered Neutron Detector Thermal Flux Mapping

The two major problems with the rhodium detector thermal flux mapping identified in Reference 1 have been addressed and are described below.

a) Epithermal Neutron Contribution to Detector Signal

Analysis of the epithermal neutron contribution to the detector signal for the HEU core has continued during this period. The results of the measurements performed during 1979 and the analysis in 1980 were presented at the June 1980 ANS meeting[2]. While the major part of this effort is completed, it would be helpful to repeat some of these measurements using beta counting in our 4-π proportional counter, at various reactor power levels, and at the beginning, middle, and end of the operating cycle.

b) Time Delay to Reach Equilibrium Signal

This problem was identified in Reference 1 as one of the more serious drawbacks in using the rhodium detector for extensive flux mapping. A technique was developed at the University of Michigan to determine the flux at a particular time (and hence, position) from the detector current known at all previous times[3]. The technique has been codified in the RHODI computer program and has been applied to data taken at various positions and detector speeds through the FNR. The results were quite acceptable, and were presented at the November 1980 ANS meeting[4]. Further work in this area has led to a dramatic simplification of the governing equations, but at the price of a surprising decrease in accuracy. While the technique has been developed adequately for use on the FNR, it would be useful to "fine tune" the codes by varying K_p, the prompt sensitivity of the detector, and to continue work on simplifying the analysis. These two efforts should yield increased accuracy and decreased computational requirements.

2. In-core Power Distribution Measurements

In order to measure the axial temperature rise of the water flowing through each fuel assembly in the FNR core, a thermocouple probe was designed, built, and tested. The probe consisted of a copper and constantan thermocouple that was designed so that it could be inserted into the regular fuel elements of the FNR[5].

Two nearly complete and two partial core maps were made using the probe. The temperature difference across a given fuel assembly was taken as the difference between the temperature readings one inch above and one inch below the fuel region of the assembly. Readings were taken at regular time intervals for several minutes and were averaged. Typical measurements had a variation of about 0.6 degrees Fahrenheit.

As mentioned above, the temperature drop across some elements was measured on four separate occasions. The data indicates that the reproducibility of the measured temperature drop across an element is good for the majority of these elements (i.e., less than 10 percent variation from the average temperature drop measured on that element). However, there were a few elements where a measured value differed by more than 20 percent from the average temperature drop measured across that element.

The temperature differences were also compared to the midplane thermal flux measured by the rhodium detector[1] in order to compare the radial power distribution that each predicts. We assume, in our preliminary discussion, that the mass flow rates and macroscopic fission cross sections are constant in the regular fuel elements so that the normalized temperature differences can be directly compared with the measured normalized fluxes. Again, agreement in most cases is good (less than 10% difference), although there were cases of serious disagreement (more than 20% difference). In addition, the <u>average</u> coolant temperature rise in the elements measured was approximately twice as large as the readings taken by the FNR control room system instrumentation. A possible source of this error is heat conduction from the fuel cladding to the tip of the probe. This would cause an error in the measurement of the outlet temperature, which <u>is</u> where the principal disagreements exist. In addition, there is uncertainty concerning the bypass flow around the active core and the relative flow through the regular and special elements. As a result, we presently view the temperature difference data with some skepticism.

3. In-core Wire Activation Experiments

In-core wire activation experiments were also made during this reporting period to provide additional

verification of earlier results for axial flux distributions. The equipment and data analysis techniques are presented in detail in Reference 1. The recent measurements yielded results which do not differ significantly from those presented there.

B. Spectral Measurements

1. In-core Spectral Measurements

This phase of the experimental program was first addressed in Reference 1. Additional work has continued along those lines. In addition to the SAND-II code, we have also acquired and implemented the SANDANL, WINDOWS, and FERRET code packages. These codes are much more recent, and provide additional unfolding capabilities, including sophisticated error analysis subroutines. New ENDF-IV and -V cross sections were obtained from Brookhaven National Laboratory, along with the INTEND code which is required to formulate the cross section libraries into a standard SAND-II compatible format. In addition, a complete set of foils was acquired in order to carry out the experimental program on both the HEU and LEU cores.

The results of unfolding a set of measurements made with five trial foils activated in the FNR are presented in Appendix A. The lessons learned from this experiment led to the design and construction of an in-core sample holder which fits into a special fuel element, and displaces nearly all of the water in the central hole. Experiments are continuing in this area.

2. Excore Spectral Measurements

a) Crystal Diffraction Measurements

The initial measurements performed on the crystal spectrometer to determine the beam port thermal flux

spectrum are summarized in Reference 1. Since measurements of the neutron temperature are strongly dependent on the crystal mosaic width, a secondary spectrometer was set up in order to do double crystal rocking measurements of the mosaic width. A perfect crystal was initially borrowed from the University of Missouri for this purpose. The results of the experiment gave an effective mosaic width which is too large to be consistent with a realistic neutron temperature. Because of this problem and the difficulty in accurately determining the crystal reflectivity, a perfect crystal was ordered from the University of Missouri. We have just received this crystal and are redesigning the spectrometer for a new set of measurements.

b) Thermal Spectrum Unfolding from Foil Activations

In theory, it should be possible to unfold the thermal spectrum at a beam port by foil activations in the manner discussed in Section B.1 above. Cross sections for non-1/v materials were obtained from Brookhaven National Laboratory, and some initial experiments have been done. The activation data have been unfolded using the FERRET and SANDANL codes and comparisons are just now being made. While this is the first time thermal spectrum unfolding has been attempted through foil activations, the preliminary results obtained seem to warrant additional work. As with the experiments mentioned above, considerable work still remains to be done in this area.

C. Reactivity Measurements

Besides the standard rod worth measurements which are done routinely on the FNR, we also performed a xenon transient experiment this past year to determine the equilibrium xenon worth in the FNR. The results agreed well with the values measured in previous experiments. In addition, a number of other conventional experiments (such

as critical loading and reactivity coefficient measurements) were performed in conjunction with our nuclear reactor laboratory course.

III. GENERIC METHODS DEVELOPMENT AND VERIFICATION

The basic calculational model used to analyze both HEU and LEU fuels has been fully described in Reference 1 and Appendix B. The following sections describe completed and current efforts to extend and improve the model. These efforts fall into four general areas: First, our methods and data base for the generation of few-group diffusion theory constants have undergone continuing development and improvement. We continue to rely upon the LEOPARD[6] and EPRI-HAMMER[7] codes for routine calculations, although two new codes-- the EPRI-CINDER[8] code and the ROD code-- have extended our computational capabilities. A new ENDF/B-IV data base has been developed for the LEOPARD code. Test results appear promising, although general use of the new library awaits the updating of many physical constants "hardwired" into the LEOPARD code. Second, many of the previous extensions of the two-dimensional diffusion theory capabilities of the 2DB[9] code have been consolidated into the 2DBUM code, with particular emphasis on user convenience and computational speed. New modifications of the 2DBUM code have been made to accomodate new and specialized applications. Third, new calculational methods have been investigated for both reducing computer costs and extending the model to particularly difficult FNR problems. Fourth, significant effort has been expended on the documentation of our LEOPARD-LINX-2DBUM code system and on the development of a reference data bank for the FNR.

A. Generation of Few-Group Constants

1. Modifications to the LEOPARD Code

Recent changes in LEOPARD have involved primarily improvements or corrections to previous capabilities. The restart capability has been generalized to permit the generation of derivative cross-sections for power defect

calculations (see Section II.E in Appendix B). The thermal expansion effects on uranium number density were changed to allow for expansion of input isotopic uranium densities. Previously, LEOPARD corrected uranium densities only when present in UO_2. To allow for the effects of flux peaking variations due to depletion on the spectrum, an additional input option has been added to provide for burnup-dependent non-lattice peaking factors (NLPF's). The binary few-group cross-section burnup library passed to LINX was improved by including more complete identifying parameters. Finally, improved printout has made interpretation of LEOPARD results much easier.

2. New ENDF/B-IV LEOPARD Library

Differences (for analyses of MTR-type fuels) between the results of the LEOPARD code and those of more sophisticated codes, such as the EPRI-HAMMER code, are primarily due to differences in the libraries used.[10] The LEOPARD code uses an early industrial data set while the other codes employ the ENDF/B-IV data. In order to remedy this inherent difference, a new library for LEOPARD was assembled from the ENDF/B-IV data.

A new code SPITS, a heavily rewritten version of the SPOTS code, processed data supplied by W.B. Henderson[11] of Westinghouse Electric Corporation into a form compatible with the LEOPARD code. The Westinghouse data were created from the original ENDF/B-IV files by the ETOT-5[12] and ETOG-5[13] codes. The SPITS code copied data for three of the 25 LEOPARD nuclides from the original LEOPARD library. Data for the remaining 22 nuclides were read from the Westinghouse tape. Cross-sections for deuterium and the lumped fission products were taken from the old library because they are not included in the Westinghouse data; the new Westinghouse hydrogen data were not used because the scattering cross-sections are based on free rather than the

desired bound hydrogen. Plots for the various cross-sections versus energy for the 23 standard nuclides were made, both for the 54-group fast library and the 172-group thermal library. Figures 1-4 illustrate the differences between the two libraries for some important nuclides.

The original LEOPARD library includes bias factors which allow results of LEOPARD analyses of critical and experimental lattices to agree with the experimentally obtained parameters. The bias is implemented in the SPOTS code by increasing the number of neutrons released per fission by 0.36%. A second bias is introduced by decreasing the number of neutrons released by ^{235}U undergoing fast fission by 1.22%. Although the latter effect is minor, the former effectively biases the calculated multiplication factor by 0.36%. Comparison of the LEOPARD results obtained using a new library incorporating these biases and those calculated using a new library without the biases with the corresponding results of more sophisticated codes indicate that the biases are not needed in the new LEOPARD library because both the library and the codes used for comparison consistently use the ENDF/B-IV data.

In order to determine the usefulness of the new library and its differences from the old library, extensive comparisons and studies were made. The two LEOPARD libraries were compared with benchmark codes, the important differences between the two libraries were deduced using a sensitivity method. In addition, an experimental critical lattice was analyzed, and both HEU and LEU FNR fuel depletion studies were performed with the 2DBUM code.

The benchmark codes used for comparisons between the LEOPARD results using the old and new libraries were the EPRI-HAMMER, VIM[14], and EPRI-CELL[15] codes. The sample cases analyzed were typical HEU and LEU plate-type MTR fuels.[16] Comparison of the microscopic cross-sections generated by these codes indicate that for the fast energy range those

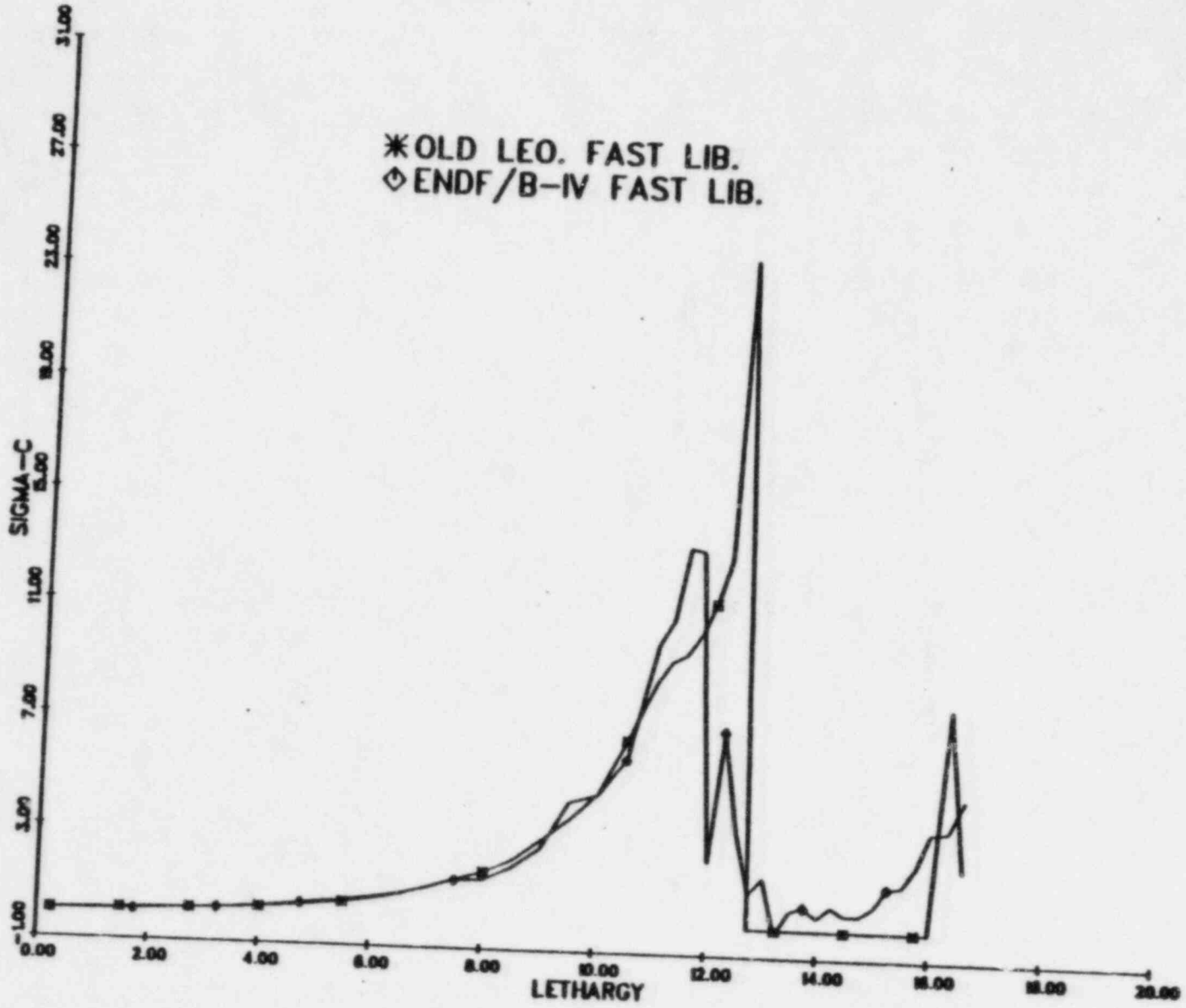

Figure 1. LEOPARD Library Comparison: ^{235}U Capture Cross-Section vs. Lethargy

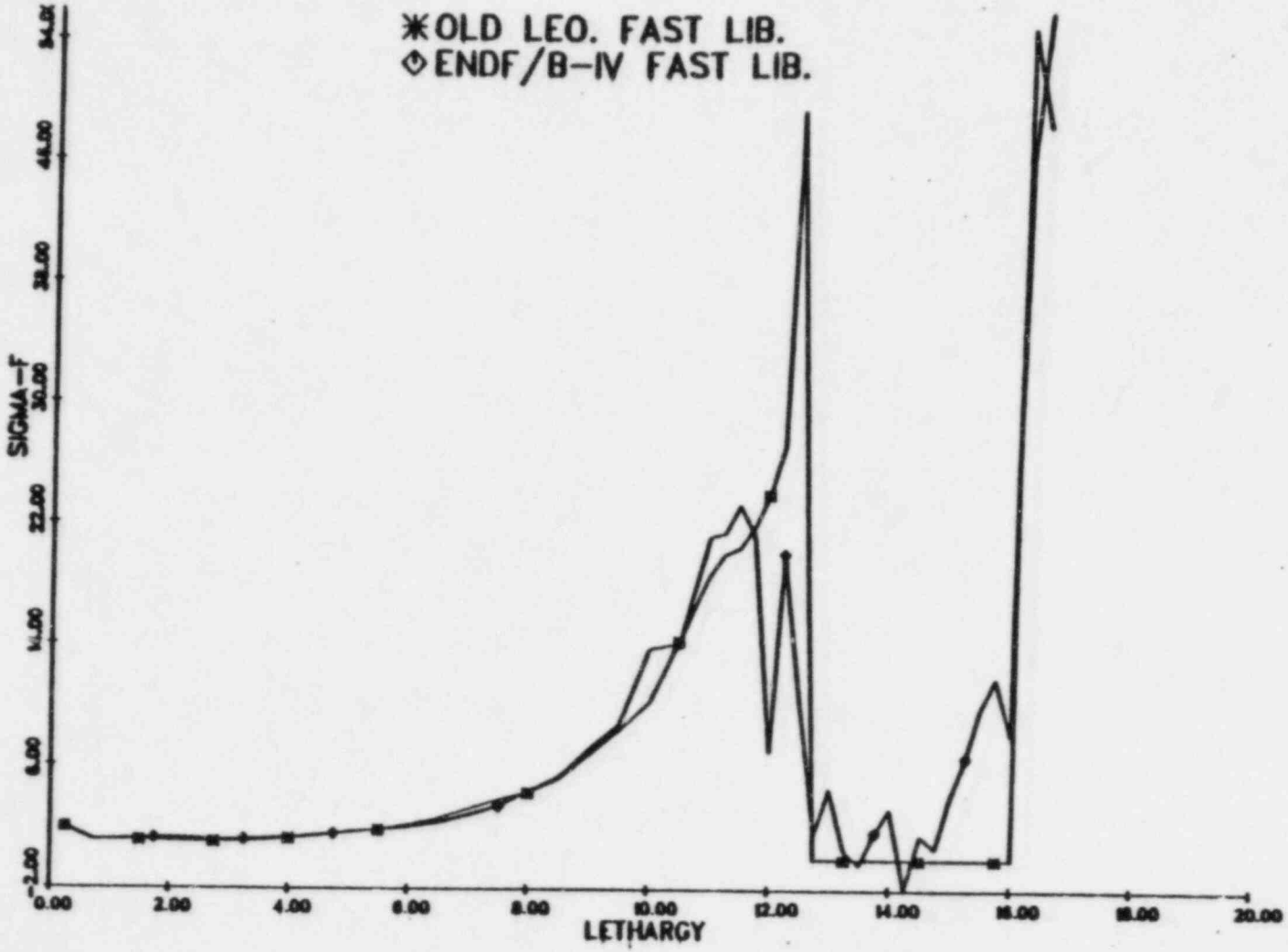

Figure 2. LEOPARD Library Comparison; ^{235}U Fission Cross-Section vs. Lethargy

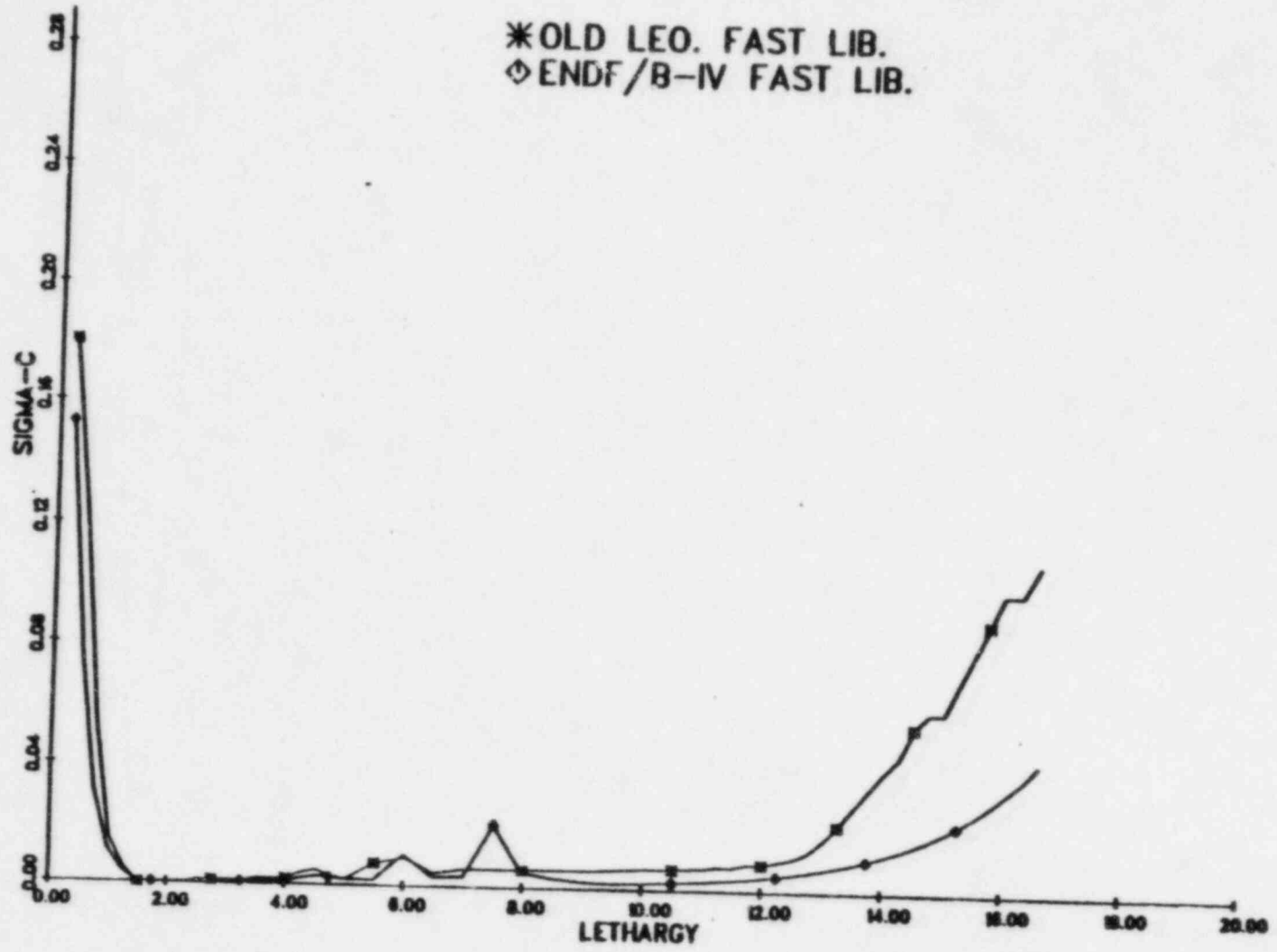

Figure 3. LEOPARD Library Comparison: ^{27}Al Capture Cross-Section vs. Lethargy

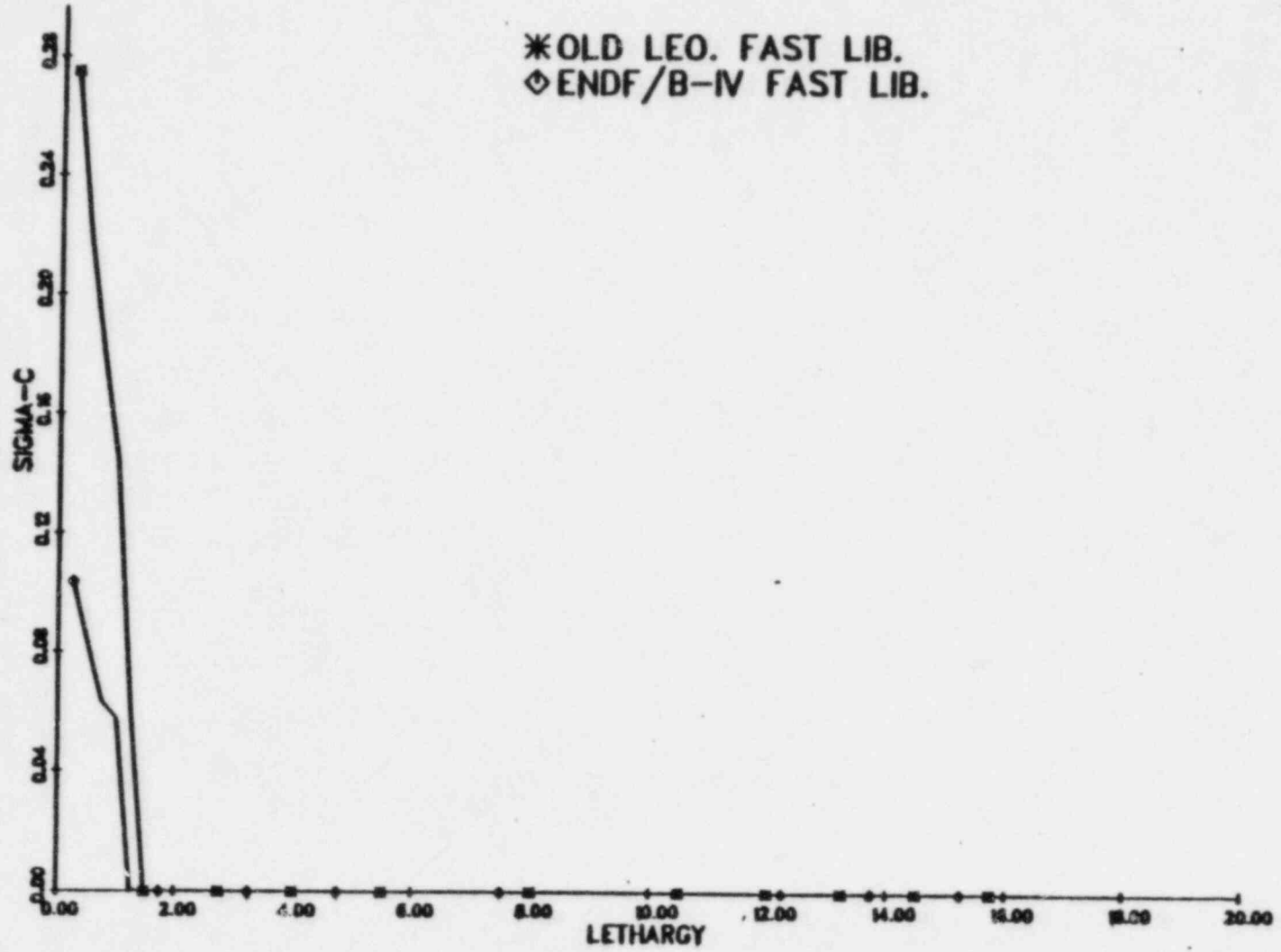

Figure 4. LEOPARD Library Comparison, ^{16}O Capture Cross Section vs. Lethargy

generated using the new library generally agree more closely with those of the benchmark codes than do those generated using the old library. In the thermal energy range, however, the microscopic cross sections of the old library compare more favorably with the benchmark cross-sections.

Before any conclusions can be made, however, the importance of the various cross-sections must be evaluated. To do this, a code incorporating a sensitivity technique was used to determine the contributions of differences in cross-section of the two LEOPARD libraries to the infinite multiplication factor. The contribution of a particular difference was calculated by multiplying the difference in the macroscopic cross-section by the importance of that cross-section to k_{inf} . Values of the most important cross-sections in the new library are generally in better agreement with the corresponding values generated by the benchmark codes than are those of the old library as seen in Table 1. for the HEU case.

The materials for which the differences between cross-sections of the two libraries have the largest influence on k_{inf} are ^{16}O, ^{27}Al, and ^{235}U. The differences between the values of these cross-sections of the two libraries can be seen in Figures 1-4. Although individually the contributions may be as much as 0.6% $\Delta k/k$, they tend to cancel one another resulting in a much smaller net difference. The net difference calculated directly by LEOPARD was 0.12% $\Delta k/k$. The sensitivity method code calculated a slightly different value, 0.14%, as a consequence of the approximate nature of the technique; however, this difference is acceptable and verifies the basic approach of the method.

In an effort to determine how well the new library simulates experimental data, the TRX rodded UO_2 lattice[17] with water/metal ratio of 2.35 was analyzed using both the old and new cross-section data sets. Both libraries predict the experimental results quite well, but in most cases the

Table 1. HEU Microscopic Cross-Sections
Important to the Infinite Multiplication Factor

Nuclide	Cross-Section	Contribution to k (%Δk/k) [a]	Value				
			Old LEOPARD	New LEOPARD	HAMMER	VIM [b]	E-Cell [b]
^{235}U	σ_{a3}	-0.602	37.5	40.2	39.7	40.2	39.9
^{1}D	σ_{s1}	+0.552	3.70-2 [c]	1.13-2	1.16-2	1.11-2	9.10-3
^{235}U	$\nu\sigma_{f3}$	+0.541	59.9	64.3	63.9	64.4	64.0
^{238}U	σ_{a4}	-0.523	442.	445.	424.	417.	421.
^{27}Al	σ_{a3}	+0.396	2.91-2	1.03-2	1.08-2	1.07-2	1.03-2
^{235}U	$\nu\sigma_{f4}$	-0.228	921.	918.	873.	859.	869.
^{27}Al	σ_{a1}	+0.073	9.60-3	6.27-3	6.80-3	6.43-3	6.15-3
^{235}U	$\nu\sigma_{f1}$	+0.038	3.11	3.69	3. .3	3.50	3.40
^{27}Al	σ_{a4}	-0.027	0.163	0.164	0.152	0.151	0.151
^{235}U	σ_{a1}	-0.013	1.25	1.30	1.30	1.34	1.31
^{27}Al	σ_{a2}	+0.011	3.50-3	3.02-3	3.06-3	2.87-3	2.71-3
^{1}H	σ_{a4}	+0.009	0.24367	0.24383	0.233	0.230	0.232
	Remaining Cross-Sections	-0.020	.....	.....	.....	.....	.....
	All Cross-Sections	+0.146	.....	.....	.....	.....	.....

[a] Contribution to k = $\frac{\Delta\Sigma}{k_\infty}\frac{\partial k_\infty}{\partial\Sigma}$, Σ = macroscopic cross-section

[b] ref. 14

[c] 3.70-2 represents 3.70×10^{-2}

old library provides slightly better accuracy (see Table 2). It is difficult to draw a conclusion from this result because one cannot be sure if the errors are introduced by the calculational scheme or by the cross-section data base. In addition, the error in the experimental data which may be as much as 2% must be considered.

Two group macroscopic constants for the 93% enriched FNR fuel generated by the LEOPARD and HAMMER codes are compared in Table 3. In most cases the parameters calculated incorporating the new library agree more closely with the HAMMER parameters. The thermal diffusion coefficient and thermal absorption cross-section calculated using the old library are exceptions because, as indicated earlier, microscopic thermal constants in the old library are generally in better agreement with those of the HAMMER code.

Complete burnup cross-section table sets of both the HEU and LEU FNR fuel have been produced by the LEOPARD code using the new library for comparison with the sets previously generated using the old library. By using each set, batch core depletion studies have been made with the 2DBUM code. In addition, a HEU critical experiment of the FNR core was simulated by the 2DBUM code using the old and new cross-section data sets.

The infinite multiplication factor of the fresh fuel calculated by the LEOPARD code incorporating the new library is higher than that obtained with the old library; as much as 0.26% for the HEU case and 0.22% for the LEU fuel. As the fuel is depleted the two values are closer to one another (see Table 4). This is a consequence of the higher absorption cross-section of ^{235}U in the new library resulting in an increased burnup rate for that nuclide. The value of the effective multiplication factor which was calculated using a constant buckling of 0.00914 cm^{-2}, shows a larger difference. The discrepancy in k_{eff} can be

Table 2. TRX Rodded UO_2 Critical Lattice Results (w/F = 2.35)

Parameter (a)	Experiment (b)	Old LEOPARD		New LEOPARD	
		Value	% diff.	Value	% diff.
δ^{28}	1.311	1.2698	-3.1	1.2843	-2.0
δ^{25}	0.0981	0.0984	+1.3	0.1061	+8.2
ρ^{28}	0.0914	0.0890	-2.6	0.0887	-3.0
CR*	0.792	0.7668	-3.2	0.7607	-4.0
B^2	0.0057	0.00564	-1.1	0.00562	-1.4
$k^{(c)}$	1.0	0.9984	-0.16	0.9977	-0.23

Notes: (a) $\delta^{28} = \frac{\text{U-238 epithermal capture}}{\text{U-238 thermal capture}}$

$\delta^{25} = \frac{\text{U-235 epithermal fission}}{\text{U-235 thermal fission}}$

$\rho^{28} = \frac{\text{U-238 fissions}}{\text{U-235 fissions}}$

$CR^* = \frac{\text{U-238 captures}}{\text{U-235 fissions}}$

B^2 = critical buckling

(b) WAPD-TM-931 (1970)

(c) Measured value assumed to be 1.0; calculated value is based on a LEOPARD run with measured critical buckling input

Table 3. Two-Group Constants of 93% Enriched FNR Fuel

Parameter	HAMMER Value	Old LEOPARD		New LEOPARD	
		Value	% diff.	Value	% diff.
k_∞	1.5556	1.5415	-0.91	1.5455	-0.65
ϕ_1/ϕ_2	2.460	2.439	-0.84	2.457	-0.13
Age	50.79	52.01	+2.40	51.26	+0.99
D_1	1.3956	1.4455	+3.58	1.4126	-1.22
Σ_{a1}	1.8578-3	2.0697-3	+11.41	1.8359-3	-1.18
Σ_{r1}	2.5621-2	2.5722-2	+0.39	2.5719-2	+0.38
$\nu\Sigma_{f1}$	2.2663-3	2.0874-3	-7.39	2.2241-3	-1.86
D_2	2.7607-1	2.8677-1	+3.88	2.8960-1	+4.90
Σ_{a2}	5.9558-2	6.0115-2	+3.01	6.0469-2	+3.62
$\nu\Sigma_{f2}$	9.3737-2	9.5112-2	+1.47	9.4850-2	+1.19

attributed to the large difference in the fast non-leakage probability, P_{NLF}. At the beginning of life the difference in k_{eff} is 0.89% decreasing to 0.75% for the HEU case after 500 days of depletion. For the LEU case, the difference is initially 0.82% and decreases to 0.59% after 700 days. The new library yields higher values of k_{eff} and k_{inf} throughout the depletion steps.

To further assess the impact of the new LEOPARD library on fuel depletion calculations, the HEU and LEU batch core configurations were analyzed for the FNR core. In the 2DBUM depletion calculations covering the fuel depletion from beginning of life through 200 days of full power operation, differences in k_{eff} for the HEU and LEU cores obtained with the two LEOPARD cross-section libraries stay nearly constant with depletion. Again, the new library predicted the higher value (see Fig. 5). For the fresh HEU core, the difference is 0.83%. After about fifteen days of fuel burnup, it peaks to about 0.90%. With time the difference gradually decreases to 0.80% at 200 days (see Fig. 6). The LEU core behaves in a similar manner. Initially the difference in eigenvalue is 0.74%. After a peak difference of 0.80% at about 20 days, the difference slowly decreases to 0.69% at 200 days. The decrease, as before, can be attributed to the faster depletion of ^{235}U with the new library.

The eigenvalues calculated in the 2DBUM simulation of the HEU critical experiment performed on June 13, 1971 during FNR cycle 147B are 1.0024 and 1.0102 for the old and new libraries, respectively. The difference of 0.78% is consistent with that found in the cases mentioned above. This case is not a completely independent evaluation of the differences between the two libraries because the data input to establish the middle-of-life core (i.e., fuel burn-up distribution) were calculated for both cases using the old LEOPARD library.

In summary, the new ENDF/B-IV library shows better

Table 4. HEU FNR Burnup Effect on LEOPARD Results

Time	Burnup	^{235}U % Burnup		k_{∞}			k_{eff}*			P_{FNL}*		
days	MWD/T	Old LEOPARD	New LEOPARD	Old LEOPARD	New LEOPARD	%diff	Old LEOPARD	New LEOPARD	%diff	Old LEOPARD	New LEOPARD	%diff
0	0	0	0	1.5417	1.5447	+0.26	1.0011	1.0100	+0.89	0.6785	0.6809	+0.35
30	10814	1.49	1.49	1.4886	1.4934	+0.32	0.9680	0.9771	+0.94	0.6789	0.6821	+0.47
100	36046	4.93	4.95	1.4674	1.4712	+0.26	0.9534	0.9619	+0.89	0.6793	0.6826	+0.49
200	72092	9.84	9.86	1.4388	1.4421	+0.23	0.9338	0.9417	+0.85	0.6799	0.6833	+0.50
300	108137	14.73	14.76	1.4089	1.4118	+0.21	0.9132	0.9207	+0.82	0.6806	0.6841	+0.51
400	144182	19.61	19.66	1.3777	1.3802	+0.18	0.8917	0.8987	+0.79	0.6812	0.6848	+0.53
500	180229	24.22	24.54	1.3447	1.3466	+0.14	0.8691	0.8756	+0.75	0.6819	0.6856	+0.54

* calculated with $B^2 = 0.00814\ cm^{-2}$

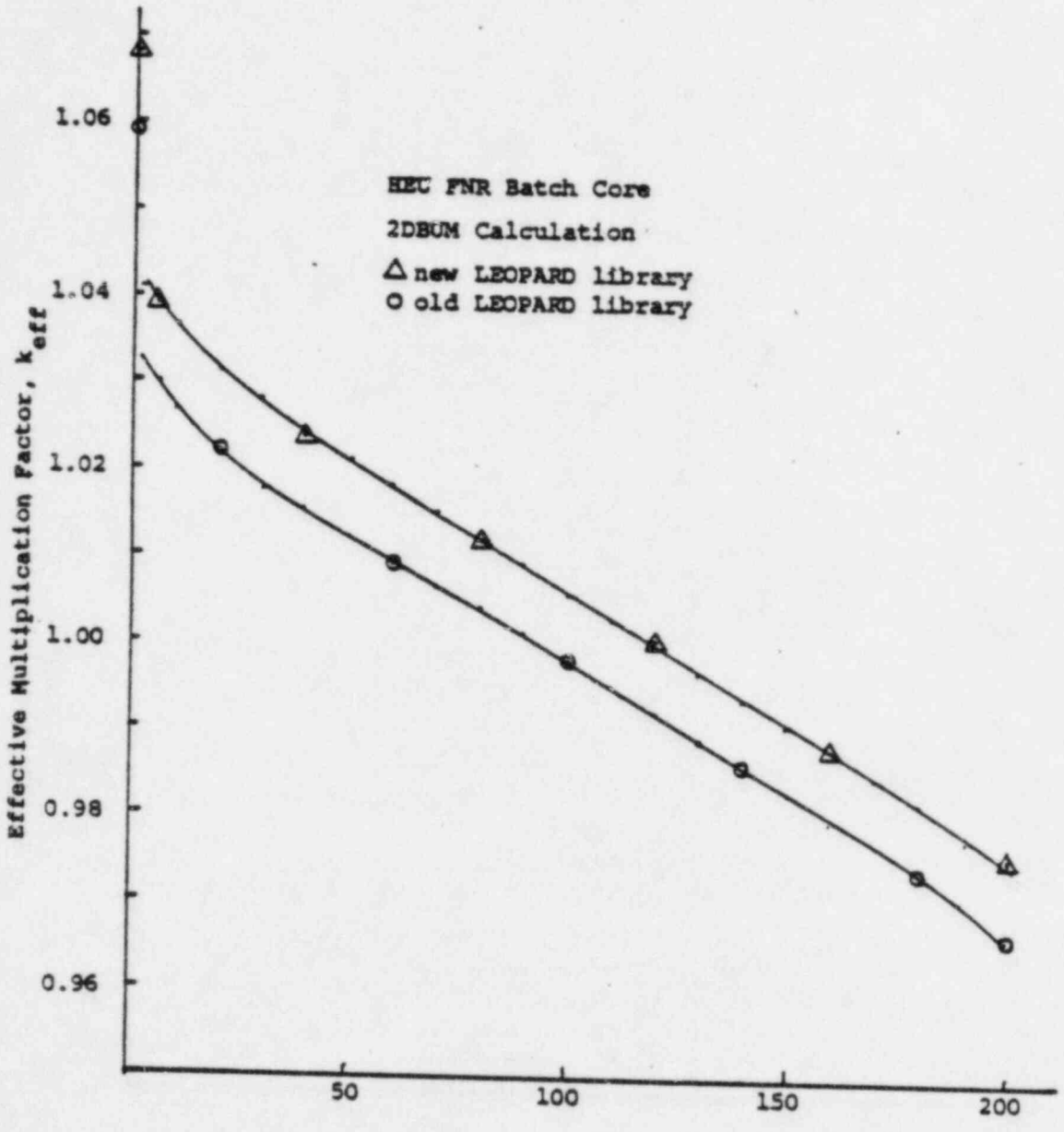

Figure 5. Effective Multiplication Factor vs. Fuel Depletion

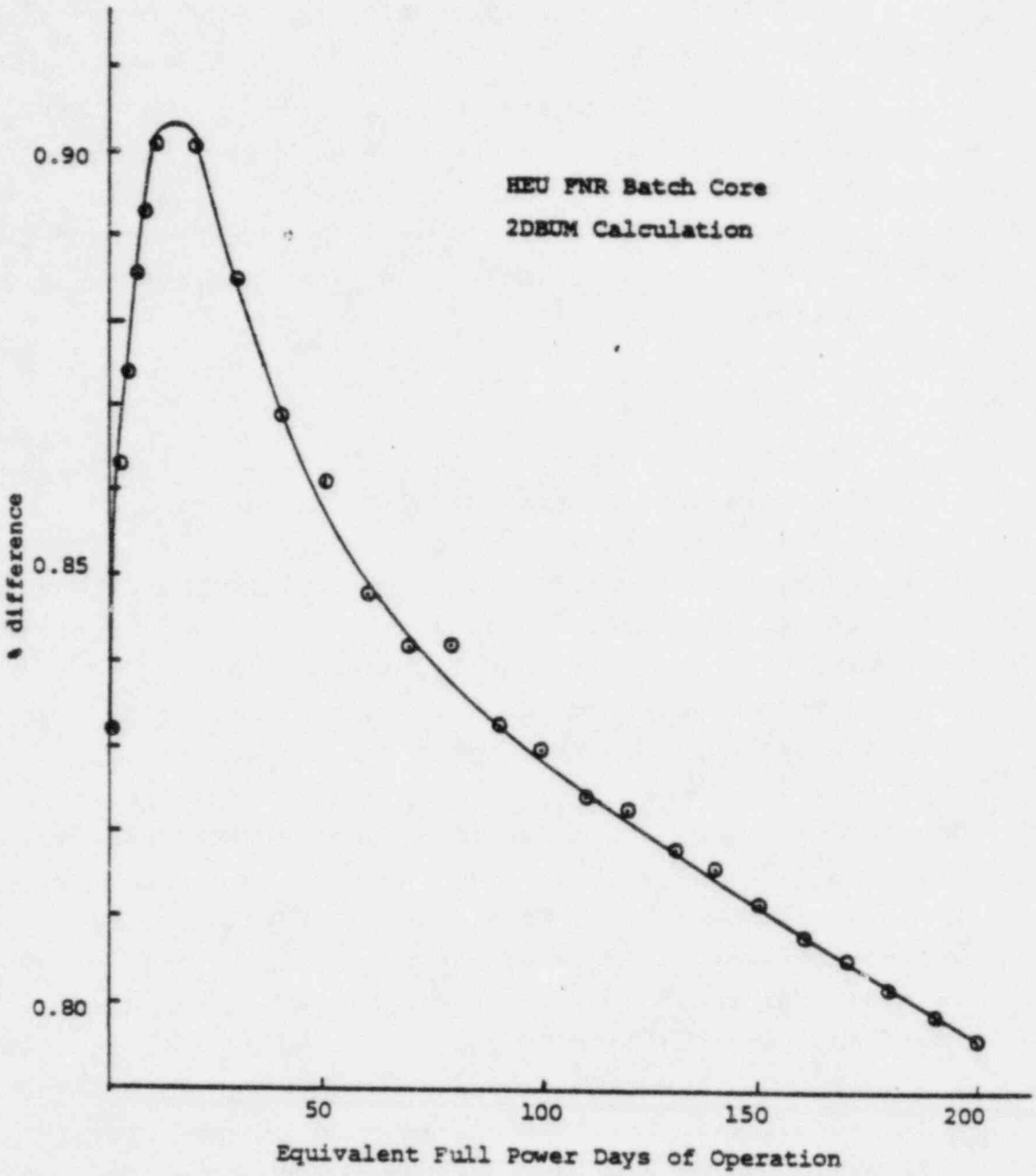

Figure 6. Difference in the Effective Multiplication Factor Dve to Different Libraries vs. Fuel Depletion

agreement with the results of more sophisticated codes on both the macro- and microscopic levels. Cores analyzed with the new library are predicted to deplete slightly faster but with a higher initial multiplication factor than are cores studied using the old library.

Currently, efforts are underway to update a number of physical constants used in the LEOPARD code. These include fission yields, decay constants, elemental densities, and atomic masses. Efforts will be made also to further explain the differences in k_{inf} and k_{eff} between the new and old LEOPARD libraries.

3. The ROD Code

The computational scheme for FNR control rod worth analysis presented in Reference 1 requires the use of the HAMMER code to generate special assembly cross-sections both with and without a control rod. To include the effects of fuel depletion on control rod worth, HAMMER calculations must be done for several special assembly burnups. Two schemes were considered for accomplishing this: The first, adding a depletion capability to HAMMER, was clearly unacceptable due to the extremely high computer costs, long development time, and major rewrite of HAMMER that would be required. The second, linking the LEOPARD and HAMMER codes to allow HAMMER calculations at any LEOPARD burnup step, was implemented via the development of the ROD code. This code is a sophisticated supervisor program which dynamically loads and runs the LEOPARD code for a special or regular assembly depletion run, saves the resulting isotopic number densities at each burnup step, sets up HAMMER input for user-specified burnup steps, dynamically loads and runs the HAMMER code, and then reformats the HAMMER generated cross-sections into a burnup library suitable for the 2DBUM code. Since the HAMMER code performs the spectrum calculation only for a specified input buckling (passed from the LEOPARD code

by the ROD code) and does not iterate to criticality, the ROD code checks the HAMMER eigenvalue. If the HAMMER eigenvalue is not sufficiently close to 1.0, the ROD code interactively asks the user for a new buckling and then reruns the HAMMER code. This interactive iteration approach was chosen to avoid the high cost of modifying HAMMER to perform criticality searches. For the case of a special assembly with control rod inserted, the ROD code makes a normal LEOPARD depletion run (i.e., no rod), estimates the critical buckling of a rodded special assembly using an empirical correlation, and then runs the HAMMER code for a rodded special assembly.

The entire calculational sequence of the ROD code is moderately expensive (about an order of magnitude greater than a standard LEOPARD depletion run) but has been used to generate cross-section burnup libraries for use in both HEU and LEU control rod worth analysis. Comparisons of predicted and measured rod worths are presented in Section III.B of Appendix B, and a comparison of HEU and LEU rod worths in Section III.F of Appendix B.

The ROD code performs many system-dependent functions related to disk file manipulation, dynamic program loading and linking, and interaction with the user via terminal input/output. As such, the code is <u>not</u> exportable to other computer systems not having both IBM Fortran and the Michigan Terminal System (MTS) operating system. Additionally, certain features of the FNR fuel assembly geometry are hardwired into the code, precluding its general use.

4. The EPRI-CINDER Code

The EPRI-CINDER code calculates fission product concentrations, effective cross sections, and other quantities based on fuel composition, fluxes and power level based on a point isotopic depletion model. The user chooses between two options, an 84-chain fission product library and

a 12-chain fission product library, which accounts for the eleven most predominant chains and creates a twelfth "effective" fission product chain to account for the remaining chains. The 12-chain library is intended for use in spatial depletion calculations. In general, the 12-chain library gives results almost identical to the 84-chain library, except for calculated effective resonance integrals.

The code has been modified to run on the Amdahl 470V/8 computer at the University of Michigan. Originally written for a CDC 6600 machine, the code is designed for greater exponent capacity than the Amdahl permits. The algorithm used to calculate nuclide concentrations includes intermediate products which are accumulated over several nuclides. These products become so small as to be outside the limits of the machine. Since the algorithm is complicated by extensive roundoff controls, the simplest solution was to multiply the time step length, power and decay constants by a constant factor at the time they are read as input. Thus, the intermediate quantities become manageable while the calculated number density remains unchanged.

To determine the accuracy of this 'fix' sample cases will be run, using the unaltered code, on the CDC 6600 machine at Michigan State University, through the MERIT Computer Network. The results of these cases will be compared with the results of identical cases run with the modified code. In addition, comparisons between the altered code and the summary tables printed in the EPRI-CINDER code manual have been made. Small differences occurred in several quantities, none greater than 0.2% in magnitude, while other results were unchanged. However, we consider the final verification must await the CDC-6600 results.

With the magnitude of any errors introduced by the code modifications thus determined, the next step will be to

compare results calculated by the EPRI-CINDER code with available experimental data sets to determine how well the code performs. The current effort is focused on identifying applicable experimental data on fission products for both LWR and MTR fuel elements. Upon verification of the sample lumped fission product correlation for LWR fuel currently used in the LEOPARD code, the EPRI-CINDER code will be utilized to generate an equivalent fission product correlation for the HEU and LEU fuel designs.

B. Global Diffusion Theory Calculations

1. 2DBUM Code Modifications

The 2DB code has continued to be our principal code for multidimensional diffusion theory analysis of the FNR. As noted previously[1], many local modifications were made to improve the usability of the code (link to LEOPARD, additional options, etc.) and to allow detailed FNR analysis (macroscopic cross-section interpolation on burnup, space dependent xenon, etc.). Early in 1980 it became apparent that an overall updating of the 2DB code was necessary in order to consolidate and clarify both the original coding and the diverse modifications made by various project members. Additionally, an overall updating would facilitate many major modifications to improve the code. Consequently, the code was largely rewritten and improved, with very large gains in computational speed and user convenience. The new version is denoted 2DBUM, and some of the major changes are discussed below.

- The names of all variables in the code were changed to mnemonics which resemble their purpose. For example, the old "K7" fission spectrum array is now denoted "CHI". This has greatly simplified checking and modifying the code.

- The FIDC free-format input processor (used by ANISN, DOT, MORSE, etc.) was incorporated to simplify input setup

and reduce input errors.

• Memory storage space was reduced by a factor of about two for many problems through rearrangement and consolidation of many large arrays. All array storage is now in one large container array which is created dynamically by 2DBUM during execution. (2START, a previously used separate code to acquire storage dynamically, is now obsolete.)

• The inner iteration coding was rewritten to follow the procedure outlined for the DIF3D code[18]. Also, cross-section subscripts were interchanged to avoid the need to copy cross-sections to a temporary array for the inner iterations. These changes resulted in decreases in total CPU time by factors of 2-4 for typical problems. As yet, improvements in the outer iteration acceleration scheme have not been made.

• The edit capabilities of the previously used 2DBED code were generalized and included in 2DBUM as a standard edit module. With only minimal additional input, a user can obtain detailed absolute and relative reaction rate edits for one or more combinations of code zones. This allows both global and local detailed results to be obtained easily from only one computer run.

• The format of the 2DBUM binary cross-section burnup library created by the LEOPARD/LINX package was modified to increase its generality and reduce the 2DBUM user input. All information pertinent to the burnup library (such as number of burnup steps, group structure, etc.) is now included in the library and need not be entered in the 2DBUM input. This reformatting facilitated such improvements as allowing different numbers of burnup steps for different materials, allowing direct access reading rather than sequential, the inclusion of both two and four group cross-sections in the same library, and reducing the core storage requirements for the 2DBUM code.

Verification of correct code operation following all of the above changes was accomplished by detailed comparisons of output from both the new and old versions of the code for many standard FNR problems.

A preliminary version of an input and reference manual for 2DBUM was written. Currently, this manual describes all necessary and optional input to the 2DBUM code, without detailing the theory or computational methods.

2. Three-dimensional Capability

The 3DB[19] code is operational on MTS and is being compared with 2DBUM results for various FNR configurations. Since the 3DB code does not include the various capabilities that have been incorporated into the 2DBUM code during the course of this project, it has been decided that future effort will be to incorporate three-dimensional capability into the 2DBUM code rather than attempting to implement the various 2DBUM options into the 3DB code. This effort, however, has not been initiated.

3. Albedo Boundary Conditions

An experimental version of the 2DBUM code has been modified to accept position-dependent two-group albedo boundary conditions as an option along with the usual boundary conditions. The input albedo is actually a matrix $\underline{\underline{\alpha}}$, relating the incoming (reflected) partial current $\underline{J}^-$ to the outgoing partial current $\underline{J}^+$,

$$\underline{J}^- = \underline{\underline{\alpha}}\,\underline{J}^+$$

where

$$\underline{\underline{\alpha}} = \begin{Bmatrix} \alpha_{11} & \alpha_{12} \\ \alpha_{21} & \alpha_{22} \end{Bmatrix}$$

and

$$\underline{J}^{\pm} = \begin{Bmatrix} J_1^{\pm} \\ J_2^{\pm} \end{Bmatrix}$$

It has been assumed that upscatter in the reflector is negligible, hence $\alpha_{21}=0$.

The advantage with using an albedo boundary condition is that the reflector nodes, which account for 60% of the mesh, can be eliminated. This will then allow the efficient use of the 2DBUM code for fuel cycle calculations which involve a large number of time steps and many iterations in order to arrive at an optimum scheme. The albedo option has been coded into the 2DBUM code and has been thoroughly checked. The results indicate a savings in CPU time by a factor of 2.5, which is less than expected on the basis of mesh number reduction but understandable when one takes into account the 2DBUM "overhead". The only aspect of this effort that remains in question is the calculation of the albedos. If pointwise albedos from full-core 2DB calculations are utilized, the relative power errors (albedo option vs. full-core option) are quite high, especially for the fuel elements adjacent to the D2O tank, where discrepancies in excess of 5% were observed. In addition the α_{12} albedo term varied significantly along the D2O tank. To remedy this a constant α_{12} for the D2O tank was determined on the basis of minimizing the RMS power error in the adjacent fuel elements. With this albedo, the full-core and albedo 2DBUM calculations agreed very well, within .02% for k_{eff} and within 1% for the maximum power error. In addition, a 38-step 2DBUM depletion calculation, with alternating time steps and fuel shuffling steps, was performed with the above albedos (assumed constant over the depletion) and compared with a corresponding full-core 2DBUM depletion run. The maximum eigenvalue difference for the entire cycle was less than .03%. Thus the albedos appear to be insensitive to core average depletion as well as spatial variations in the loading pattern. Effort is still being expended to examine the optimum procedure for computing the

albedos and to automate the procedure in order to eliminate the considerable amount of hand manipulations and calculations to arrive at an optimum albedo set.

4. Power Defect

The 2DBUM code can be used to analyze the effect of non-uniform temperature effects, such as for calculation of the power defect, by utilizing "derivative" cross-sections taken from a particular combination of base and restart LEOPARD runs. No changes were made to the 2DBUM code because existing "mixing" routines in 2DB were utilized. See Section II.E of Appendix B for further explanation.

5. Transverse Buckling

Calculations to determine appropriate bucklings for X-Y geometry FNR calculations have yielded a set of zone and group dependent bucklings that give good agreement between two- and three-dimensional calculations. These bucklings, shown in Figure 7, were edited from three-dimensional VENTURE[20] flux profiles calculated for the FNR Cycle 175D core. The VENTURE axial geometry geometry had 28 planes with 14 planes in the core region. The bucklings were edited by an integration over the central 6 core planes as illustrated in Figure 8. Integration over this particular volume gave slightly better agreement between two- and three-dimensional flux profiles at the core midplane and calculated core eigenvalues. The results of the two- and three-dimensional flux and eigenvalue calculations are compared in Table 5.

C. Specialized Methods and Applications

1. Monte Carlo Code Development

Extensive research effort has been directed toward the development of a very fast and inexpensive Monte Carlo code.

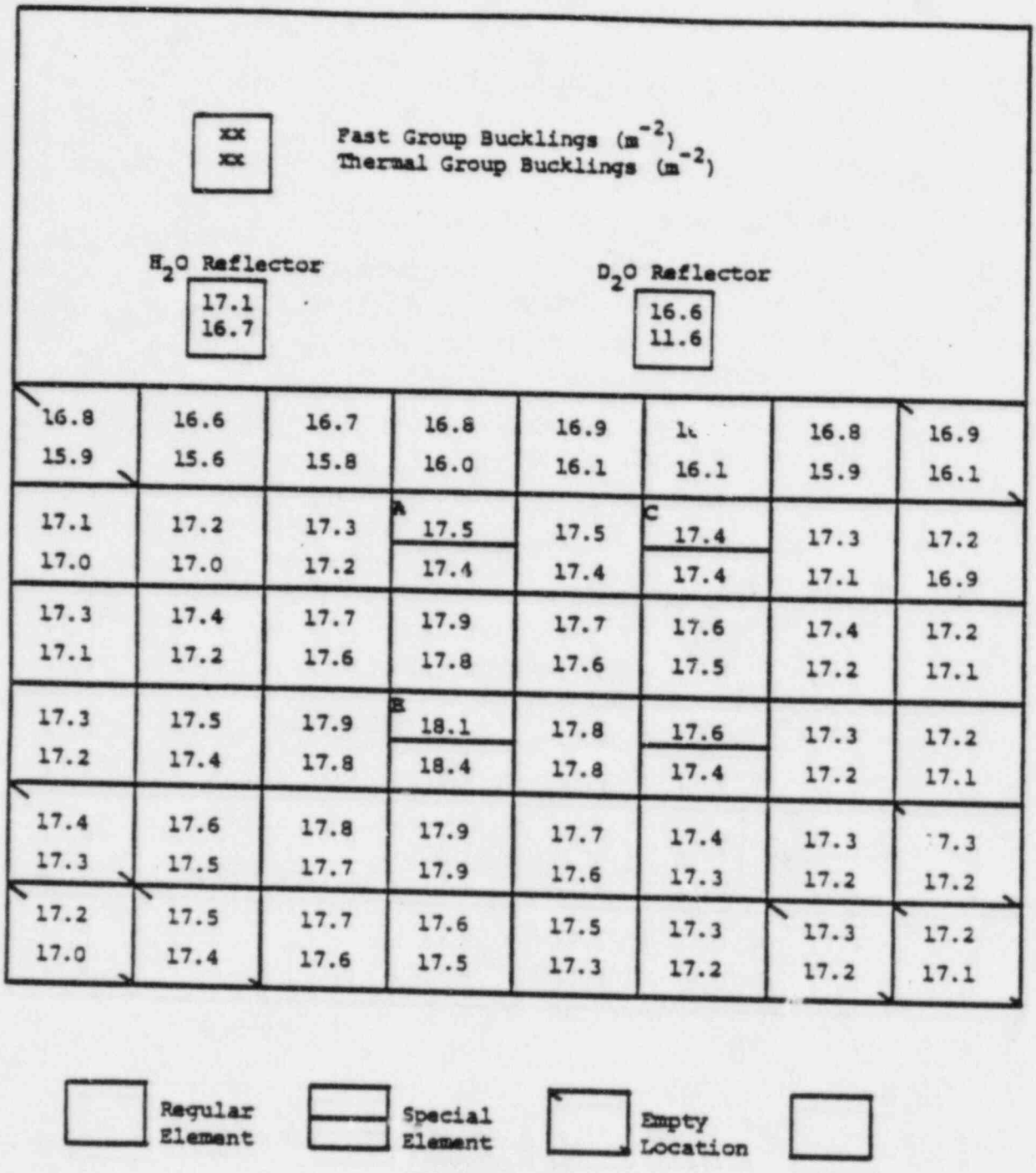

FNR Cycle 175D
VENTURE Calculation

Figure 7. Calculated Transverse Bucklings

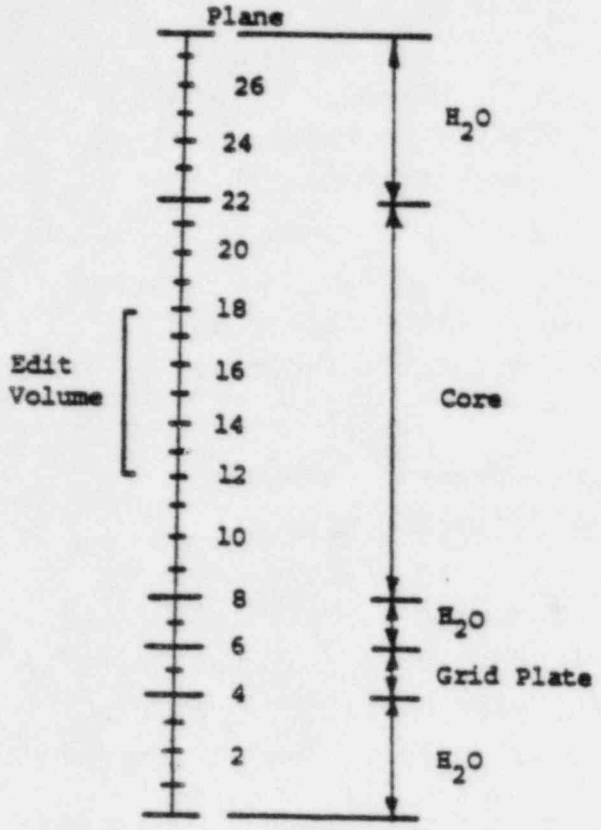

Buckling Edit

$$B_z^2 = \frac{\int_{vol} \frac{\partial^2 \phi}{\partial z^2} \, dV}{\int_{vol} \phi \, dV}$$

$$= \frac{\int_{sur} \frac{\partial \phi}{\partial z} \, dA}{\int_{vol} \phi \, dV}$$

Figure 8. Axial Geometry for 3-Dimensional VENTURE Calculation

Table 5.

Flux and Eigenvalue Comparisons for 2- and 3-Dimensional Geometry

Code	Geometry	RMS Deviation in Midplane Thermal Flux	Core Eigenvalue
VENTURE	X-Y-Z	Reference	1.0258
2DBUM	X-Y	.10%	1.0256

It is anticipated that such a code, running 1-2 orders of magnitude faster than standard production codes, will be useful for many specialized problems including the determination of errors introduced by cell homogenization, estimation of the effects of performing unit cell spectrum calculations for flat rather than curved plates, and analysis of leakage flux for the difficult D_2O tank geometry.

Work is near completion on a general geometry, multigroup Monte Carlo code incorporating many novel features to enhance computational speed and accuracy. Foremost among these are a new discrete conditional sampling method which eliminates the need for table searches when analyzing collisions[21], a moment-preserving equiprobable step function treatment of exit directions from collisions (which avoids both table searches and negative weights)[22], and the generalized surface segment geometry treatment of the ANDY code[23].

2. Reactor Kinetics Parameters

The utilization of the point kinetics equation for reactivity measurements requires accurate values of the kinetics parameters, e.g., the effective delayed neutron fraction β_{eff} and the neutron generation time ℓ. In order to assess the accuracy of the β_{eff} value currently in use for the FNR core and as a first step in evaluating the changes in the kinetics parameters due to the use of the proposed LEU fuel, calculation of β_{eff} for the present FNR configurations has been performed. The calculation to date has been based on the definition[24] of β_{eff} in the form:

$$\beta_{eff} = \frac{\langle \phi^*, \beta \chi_d P \phi \rangle}{\langle \phi^*, \chi P \phi \rangle} \qquad (1)$$

where ϕ is the neutron flux, ϕ^* is the adjoint neutron flux, and P is the production operator. The fission

neutron spectrum $\chi(E)$ may be written in terms of the prompt spectrum $\chi_p(E)$ and the delayed spectrum $\chi_d(E)$ as:

$$\chi(E) = (1-\beta)\chi_p(E) + \beta\chi_d(E) \qquad (2)$$

where β is the physical delayed neutron fraction. We have tried to evaluate β_{eff} based on Equation (1) through (a) a first order perturbation analysis and (b) explicit eigenvalue calculations. In the first approach, standard first-order perturbation theory calculations were performed with the forward and adjoint neutron fluxes calculated for the normal fission spectrum $\chi(E)$. In the second approach, following Kaplan and Henry[25], we assume that the effect of the delayed neutrons is confined to the production operator term and write the reactivity perturbation ρ due to delayed neutrons as:

$$\rho = \frac{\langle \phi^*, \delta(\chi P)\phi \rangle}{\langle \phi^*, \chi P \phi \rangle} \qquad (3)$$

where $\delta(\chi P) = \beta\chi_d P$. With the perturbed production operator $(\chi P)'$ as:

$$(\chi P)' = \chi P + \beta\chi_d P$$

one calculates the eigenvalue k' for the perturbed system. Together with the unperturbed eigenvalue k for the normal spectrum $\chi(E)$, one obtains:

$$\rho = \frac{k'-k}{k'k} \qquad (4)$$

Our calculation of the effective delayed neutron fraction β_{eff} has so far been based on the four-group structure of the LEOPARD code, and six delayed neutron groups. We have used the fractional yields of delayed neutrons in each of the six delayed groups and the total

yield recommended by R. J. Tuttle[26], while the delayed neutron spectrum for ^{235}U is taken from Saphier et al.[27] Spatial calculations were performed with the 2DBUM code in X-Y geometry with a (6x6) mesh for each fuel element. The first order perturbation calculations of β_{eff} were performed with the PERTV[28] code based on the four-group fluxes produced by the 2DBUM code.

3. Ex-Core Neutron Flux Analysis

For calculating the neutron flux in the core reflectors and the neutron beam tubes a number of code packages have been adapted to the MTS computing system and tested in preliminary calculations. The SCALE-0 code package[29] is being used to generate few-group cross sections for the excore calculations. Initial SCALE-0 calculations to collapse a 27 group (14 fast / 13 thermal group) master library used the NITAWL code with the Nordheim resonance treatment for the resonance self-shielding calculations. The spectral-spatial effects were modeled in a one-dimensional full-core transport calculation using either the XSDRN or ANISN codes.

Collapsed cross sections from the SCALE-0 system may be used in both full-core transport and diffusion theory calculations. A number of schemes are being investigated for calculating local flux profiles in regions such as the heavy water tank or neutron beams tubes. First and last flight transport codes have been used in preliminary tests to calculate the neutron streaming through the beam tubes.

D. Data Bank

A collection of standard code input and documentation has been assembled in computer files to form a data bank for our LEOPARD-LINX-2DBUM code system. The purpose of the data bank is to allow standardization in testing and verifying our codes, as well as standardization of input for our

routine FNR calculations. When codes are modified the test files are used to verify the accuracy of the calculation. For routine FNR calculations the data bank files make it convenient for someone unfamiliar with our calculations to set up a particular case. Standardized input to the cross section codes is especially valuable for comparison of subsequent core calculations. A limited selection of the standardized LEOPARD input and output is presented in Appendix C.

Documentation for our LEOPARD-LINX-2DBUM code system is also being developed. The documentation includes complete input instructions and sample problems that are stored in computer files for convenience in modifying the data and in transmitting the codes and code manuals to other facilities.

IV. ANALYSIS OF CURRENT FNR CORE AND COMPARISON WITH EXPERIMENT

To test and verify the accuracy of our analytic methods used for predicting the neutronic characteristics of the FNR many calculations have been made and compared with experimental data. These calculations include core criticality, flux and power distributions, control rod worth, power defect, void coefficient of reactivity, fuel burnup, and reactor kinetics parameters. The results of many of these calculations have been summarized in Part III of Appendix B. In this section we describe those additional calculations not included in the appendix.

A. Power Defect

Using the methods described in Section II.E of Appendix B, a preliminary calculation of the FNR power defect yielded -.16% Δk/k, which may be compared with the experimental value of -.21% Δk/k. We are currently attempting to improve our model. See Section III.B of Appendix B for further discussion.

B. Void Coefficient of Reactivity

To predict the impact of LEU fuel on the void coefficient of reactivity a calculational method has been developed and compared with void coefficient measurements for the FNR. In the void coefficient experiments performed as part of the Nuclear Engineering Department reactor laboratory course the void is simulated by inserting an aluminum blade into the core. Because the cross sections for aluminum are finite the experiment does not truly measure the void coefficient of reactivity, but for our purposes the experiment and calculation can provide a valid basis for comparing the HEU and LEU fuels.

In the experiment an aluminum blade measuring .040" x 2.25" x 24.0" is inserted vertically into the central water

channel of the fuel elements. Once the blade is inserted and reactor power stabilized at the initial level the core reactivity change is calculated from the change in regulating rod position.

To calculate the FNR void coefficient of reactivity a two-group diffusion and perturbation theory analysis was used. In this analysis the forward and adjoint flux distributions were calculated with the 2DBUM code using a 10 x 10 or 12 x 12 mesh/element. The two-group cross sections for the flux calculations were from our standard burnup dependent LEOPARD cross section libraries. In the perturbation theory analysis the insertion of the aluminum blade is represented by a change from water to aluminum cross sections. These cross sections, compared in Table 6, were generated with the HAMMER code, rather than through the less accurate LEOPARD code, because the results of the perturbation analysis depend heavily on the accuracy of these cross sections.

Table 6. Cross Sections for the Void Coefficient Calculation

Cross Section		Water	Aluminum	Change
$\Sigma_{a,1}$	(cm^{-1})	.00043	.00039	-.00004
$\Sigma_{s,1-2}$	(cm^{-1})	.0462	.0002	-.0460
$\Sigma_{a,2}$	(cm^{-1})	.0166	.0102	-.0063
D_1	(cm)	.907	2.35	1.44
D_2	(cm)	.173	4.33	4.16

The first order perturbation theory analysis performed with the PERTV code calculates the void reactivity change as:

$$-\Delta k/k = \iint \{(\bar{\nabla}\phi_1 \cdot \bar{\nabla}\phi_1^*)\Delta D_1 + (\bar{\nabla}\phi_2 \cdot \bar{\nabla}\phi_2^*)\Delta D_2 + \phi_1\phi_1^*\Delta\Sigma_{a1} + \phi_2\phi_2^*\Delta\Sigma_{a2} + \phi_1\phi_1^*\Delta D_1 B_z^2 + \phi_2\phi_2^*\Delta D_2 B_z^2 + \phi_1(\phi_1^* - \phi_2^*)\Delta\Sigma_{s1\to 2} - \frac{1}{k}\phi_1^*(\phi_1\Delta\nu\Sigma_{f1} + \phi_2\Delta\nu\Sigma_{f2})\} \, dxdy$$

$$1/k \iint \phi_1^*(\phi_1\nu\Sigma_{f1} + \phi_2\nu\Sigma_{f2}) \, dxdy$$

The first order approximation is appropriate for this calculation because the aluminum blade is only .040" thick compared to the thermal diffusion lengths which are typically 3-5 cm. Therefore, the blade cannot significantly perturb the flux distributions.

To verify our methodology for predicting the void coefficient of reactivity the experiment performed during FNR Cycle 169B was simulated. The core configuration and blade positions during the experiment are shown in Figure 9. The comparisions of calculated and measured void coefficient of reactivity in Figure 10 indicate reasonable agreement when uncertainties in measurements are considered. The uncertainties in the measured void coefficients of reactivity in Figure 10 represent the variation in the measurements taken by three students during this reactor laboratory experiment.

2/12/79

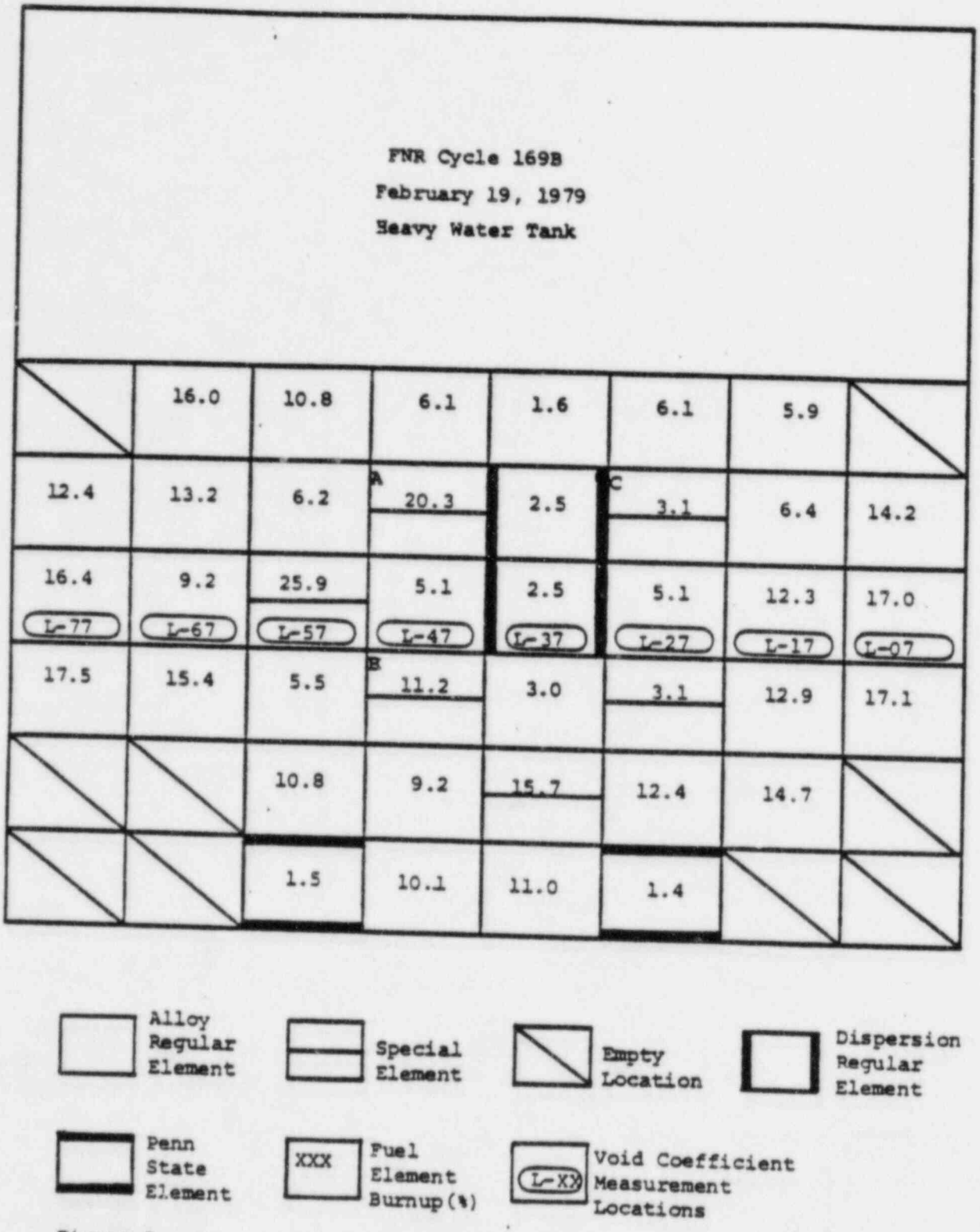

Figure 9. Core Configuration for Void Coefficient of Reactivity Experiment

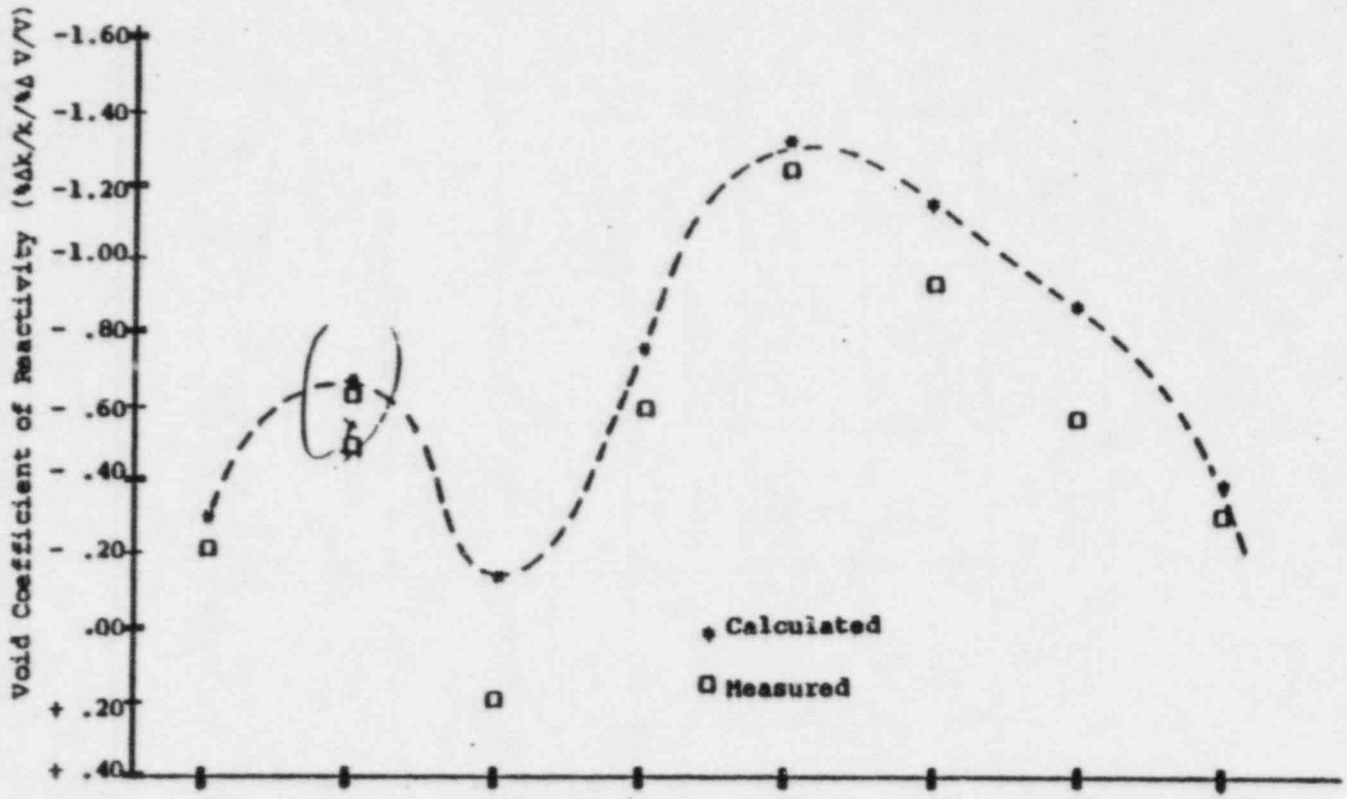

Core Position	L-77	L-67	L-57	L-47	L-37	L-27	L-17	L-07
Element Type	Alloy	Alloy	Special	Alloy	Dispersion	Alloy	Alloy	Alloy
Void Coefficient (%Δk/k/%ΔV/V)								
Calculated	-.28	-.48	-.12	-.75	-1.30	-1.13	-.86	-.37
Measured	-.21	-.46	+.20	-.58	-1.23	- .88	-.55	-.28
Measurement Uncertainty	±.07	±.13	±.23	±.32	±.02	± .01	±.04	±.01

Figure 10. Void Coefficient of Reactivity for FNR Cycle 169B Core

C. FNR Fuel Burnup Calculations

Several fuel burnup calculations have been performed for the FNR core to determine accurate fuel burnup distributions for other calculations and to assess the accuracy of different calculational schemes. These calculations and the results are briefly described in this section.

To provide burnup distribution data for the more recent FNR cores a 2DBUM burnup calculation has been performed to simulate FNR operation from October 10, 1978 to May 1, 1980. This calculation used a 2x2 mesh/element and 105 time steps to simulate 330 full power days of operation. The calculated fuel element burnups have been used in other more detailed calculations, such as control rod worth calculations for the FNR core.

Fuel burnup calculations using a 2x2 homogenous mesh structure have been compared with a 6x6 heterogenous mesh for the HEU equilibrium core. The purpose of these calculations was to determine the adequacy of the 2x2 mesh structure which we have relied upon for nearly all fuel burnup calculations. The conclusion of the study was that the 2x2 mesh calculation overpredicts the special element fuel burnup by about 7 to 8% as compared with the 6x6 mesh calculation. A likely reason for the difference is that in the 6x6 calculation the flux will peak in the waterhole region of the special element and not so much in the special element fuel region. In the 2x2 homogenous calculation, however, the flux will be enhanced throughout the smeared fuel element. For regular fuel elements there were negligible differences between 2x2 and 6x6 calculations.

Equilibrium core fuel-burnup calculations, in which the xenon build-up is explicitly modeled in 2DBUM, have been compared with our more standard calculations without xenon build-up. The conclusion of this study was that the calculated fuel burnup distribution is not significantly

different although the computing costs of modeling the xenon build-up are significantly higher because of the large flux perturbations from time step to time step.

D. Control Rod Worth

The development of the ROD code, described in Section III.A.3, has provided the capability to include special assembly fuel depletion effects on control rod worth. Comparison of measured and calculated control rod worth for six different FNR configurations are presented in Section III.B of Appendix B. The results verify the validity of our calculational model for control rod effects, and also seem to indicate that depletion of the boron in the rods causes a small but noticeable decrease in rod worth over a period of several years.

In addition to our standard control rod worth analysis using a 6x6 mesh/element in full core calculations, we have also investigated the use of rod worth calculations with only a 2x2 mesh/element. The purpose of this investigation was to find an inexpensive, although not necessarily highly accurate, scheme for calculating rod worth. The scheme would be necessary for realistic survey type calculations to determine optimal fuel loading strategies for the FNR. The quantitative results of this investigation are summarized in Table 7. The table shows that 2x2 mesh/element calculations may be used to predict control rod worth with a slight loss in accuracy, but a considerable savings in computing cost. In general 2x2 mesh/element calculations may be used for survey calculations and verified with 6x6 mesh/element calculations when necessary.

Table 7. Comparison of 2x2 and 6x6 Mesh/Element for Control Rod Worth Calculations in FNR Equilibrium Core Model

Rod Worth (%Δk/k)	6x6 Mesh	2x2 Mesh	% Error
Rod A	-2.14	-2.27	5.9 %
Rod B	-2.15	-2.21	2.6 %
Rod C	-1.96	-1.89	-3.8 %

E. Reactor Kinetics Parameters

Using the methods presented in Section III.G.2, two different FNR configurations were analyzed to date in our β_{eff} calculations: a full-core model simulating an actual FNR configuration and a half-core model representing a batch beginning-of-life configuration. The perturbation theory calculation for the full-core FNR configuration yielded β_{eff} = 0.77% with β_{eff}/β = 1.11. Values of 1.13 for β_{eff}/β and β_{eff}=.785% were obtained in a similar calculation for a batch half-core configuration. In contrast, the eigenvalue method applied to the batch half-core configuration yielded β_{eff}/β = 1.08, or β_{eff} = 0.751%. The physical fraction β was taken to be 0.6955% as recommended by Tuttle[26]. All of these estimates for β_{eff} are in reasonable agreement with a value of 0.755% for β_{eff} currently in use for the FNR core.

Parametric calculations have also been performed with the 2DBUM code in cylindrical geometry to assess the adequacy of our X-Y geometry model in representing neutron leakage in the axial direction through a transverse buckling term. These parametric calculations suggest that our X-Y

simulations are acceptable for the purpose of β_{eff} calculations. Further work is underway to resolve the differences in the values of β_{eff}/β, 1.13 versus 1.08, for the batch core calculated with the two different calculational schemes. In addition, alternative methods of calculating β_{eff} will be studied in an effort to reconcile larger values of the ratio β_{eff}/β reported earlier[30]. Future efforts under consideration also include experimental determination of the ratio β_{eff}/β in the current FNR configurations. Comparison between the calculated β_{eff} values for the HEU and LEU configurations will also be made.

V. ANALYSIS AND OPTIMIZATION OF LEU FUEL

Extensive analyses have been performed comparing the current HEU and proposed LEU fuels. The analyses were performed in both batch and equilibrium core configurations and are summarized in Section VI of Appendix B. In this section we present additional comparisons between the HEU and LEU fuels in regard to the void coefficient of reactivity and control rod worth. We also present the important results from analyses that have been performed to determine optimized core configurations and to study alternative fuel designs. The main purpose of these analyses was to find effective means of increasing the discharge fuel burnup for the FNR core. Presently fuel is discharged at approximately 17% fissile depletion which is relatively low in comparison with that achieved at other research reactors. The most important conclusion of our analysis has been that small increases in core reactivity can result in large increases in fuel burnup. These effects are explained more fully in Appendix B.

A. Equilibrium Core Void Coefficient of Reactivity

The void coefficient of reactivity was calculated for the HEU and LEU equilibrium cores using the methods described in Section IV.B. In these calculations the void is simulated by aluminum and therefore is not a truly voided region. The calculated void coefficients for the two cores are compared in Figure 11 and the individual components corresponding to the terms of the first order perturbation theory expression for the reactivity change are compared in Table 8. These reactivity components may be interpreted as representing the cause of the reactivity change in our two-group diffusion theory analysis. The diffusion theory analysis should not be expected to predict accurately the reactivity effects caused by a change in neutron leakage, but the effects of the change in absorption and slowing down

should be more accurately predicted. These calculations show practically no differences in the void coefficient of reactivity between the HEU and LEU cores, although for the LEU core the void coefficient is slightly more peaked in the center of the core.

B. Control Rod Effects

In an effort to identify significant differences between control rod effects on HEU and LEU fueled cores, detailed studies have been made of the neutronic effects caused by rod insertion. Using the methods described in Reference 1, the batch fresh test cores of Reference 1 were analyzed with and without control rods for both HEU and LEU fuels. Since a half-core symmetric model was used, results must be interpreted in terms of two inserted rods in the scuth half of the cores. Neutron balance tables obtained from 2DBUM are presented in Tables 9 and 10. Study of these and other similar results has led to several qualitative conclusions outlined below.

The FNR control rods are black to thermal neutrons and grey to fast neutrons. There is extreme flux depression near the rods for the thermal group and little flux depression for the fast group, resulting in a significant change in the whole-core fast/thermal flux ratio. These spectral effects (caused by absorption) are a major contributor to the overall control rod worth. As can be seen from the neutron balance tables, the dominant effects (in order) are: increased fast neutron leakage from the core, increased fast absorption, and increased thermal absorption.

A detailed comparison of the HEU and LEU core neutron balance shows that although there are different amounts of fast absorption and leakage induced by rod insertion, the changes in fast absorption and leakage due to rod insertion are nearly identical for both cores. This is reasonable,

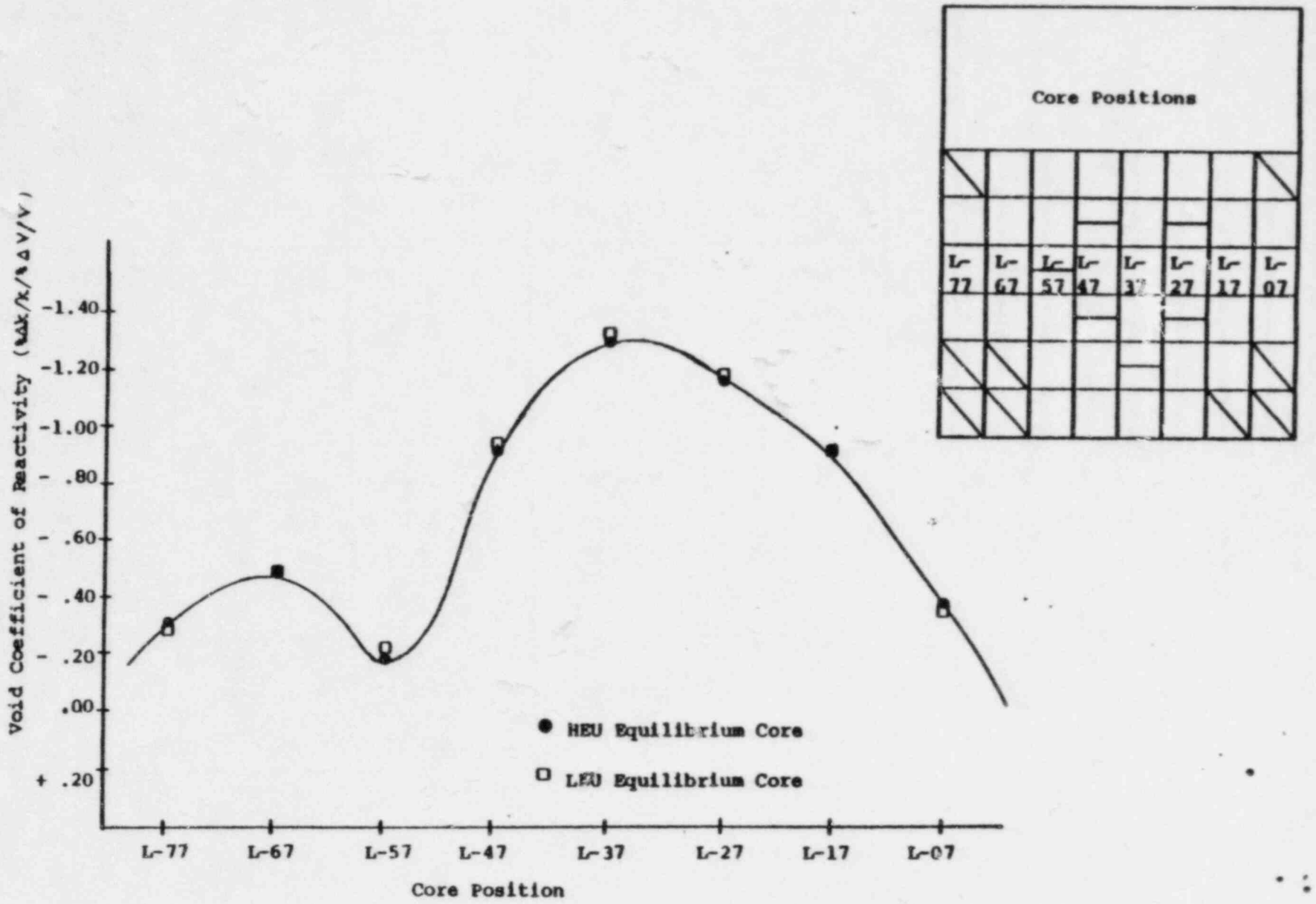

Figure 11. Void Coefficient of Reactivity Calculated for the Equilibrium Cores

Table 8.

Void Reactivity Components for Equilibrium Cores (%Δk/k/%Δ V/V)

Core Position	L-77		L-57		L-37		L-17		Reactivity Components with Source Normalization
Element Type	Regular		Special		Regular		Regular		
Fuel	HEU	LEU	HEU	LEU	HEU	LEU	HEU	LEU	$\phi_1^*(\phi_1 \nu\Sigma_{f1} + \phi_2 \nu\Sigma_{f2}) = 1$
Fast Group									
Absorption	.00	.00	.00	.00	.00	.00	.00	.00	$\phi_1 \phi_1^* \Delta \Sigma_{a_1}$
Z Leakage	-.03	-.03	-.10	-.10	-.18	-.18	-.09	-.09	$\phi_1 \phi_1^* \Delta D_1 B_z^2$
X-Y Leakage	-.12	-.11	-.04	-.04	-.02	-.01	-.10	-.10	$(\nabla\phi_1 \cdot \nabla\phi_1^*) \Delta D_1$
Downscatter	-.15	-.16	-.10	-.16	-1.24	-1.29	-.60	-.63	$\phi_1 (\phi_1^* - \phi_2^*) \Sigma_{s,1\to2}$
Thermal Group									
Absorption	.04	.04	.23	.22	.24	.21	.13	.11	$\phi_2 \phi_2^* \Delta \Sigma_{a2}$
Z Leakage	-.05	-.04	-.23	-.22	-.28	-.24	-.15	-.13	$\phi_2 \phi_2^* \Delta D_2 B_z^2$
X-Y Leakage	.00	.04	.08	.09	.18	.19	-.10	-.07	$(\nabla\phi_2 \cdot \nabla\phi_2^*) \Delta D_2$
Total	-.30	-.27	-.16	-.21	-1.30	-1.33	-.91	-.91	Δk/k

Table 9.

Neutron Balance for Control Rod Effects in HEU Batch Test Core

	Neutron Balance for Core Region (% of total fission source)		
	Rod Out	Rod In	(In-Out)
Fast Group			
absorption	4.1	5.5*	1.4
leakage**	30.3	32.3	2.0
Thermal Group			
absorption	64.4	65.7*	1.3
leakage**	-2.3	-2.5	-.2
Total Losses	96.5	101.0	4.5

	Rod Out	Rod In
Core-averaged (ϕ_1/ϕ_2):	1.98	2.14
Core-average ϕ_1:	3.06×10^{13}	3.19×10^{13}
Core-averaged ϕ_2:	1.54×10^{13}	1.49×10^{13}

*Core/Rod Breakdown:
fast abs.(core)--4.3
fast abs.(rod) --1.2
therm. abs.(core)-63.4
therm. abs.(rod) - 2.3

**Leakage includes DB_z^2 losses

Table 10.

Neutron Balance for Control Rod Effects in LEU Batch Test Core

	Neutron Balance for Core Region (% of total fission source)		
	Rod Out	Rod In	(In-Out)
Fast Group			
absorption	7.5	8.9*	1.4
leakage**	29.4	31.3	1.9
Thermal Group			
absorption	62.2	63.3*	1.1
leakage**	-2.7	-2.9	-.2
Total Losses	96.4	100.6	4.2

	Rod Out	Rod In
Core-averaged (ϕ_1/ϕ_2):	2.23	2.42
Core-averaged ϕ_1:	3.00×10^{13}	3.12×10^{13}
Core-averaged ϕ_2:	1.35×10^{13}	1.29×10^{13}

*Core/Rod Breakdown:
fast abs.(core)-- 7.7
fast abs. (rod)-- 1.2
therm. abs.(core)-61.2
therm. abs.(rod) - 2.1

**Leakage include DB_z^2 losses

since the fast flux distribution is sensitive mainly to gross changes in the fission source distribution or core geometry.

A similar comparison of changes in thermal neutron losses due to rod insertion shows that the extra change in thermal absorption is responsible for the decreased rod worth in the LEU core. Examination of thermal absorption in both cores (see the table and footnotes) shows that thermal absorption in the non-rod portion of the core decreases for both HEU and LEU when the rod is inserted. This decrease is the same for both cores, about 1% of the total source, indicating that global effects on the thermal flux are quite similar; i.e., changes in global thermal flux are determined primarily by core geometry for black rods. The major difference in control rod effects between the two cores is the increased thermal absorption in the rod itself-- 2.3% of the total source for the HEU core versus 2.1% for the LEU core. This effect seems to be due to the lower thermal flux in the LEU core, offset somewhat by the smaller diffusion length in material surrounding the rod.

C. Alternative Fuel Designs

The core physics analysis presented in Appendix B compares HEU and LEU fuels, in both batch and equilibrium core configurations. In addition, the final section of the appendix compares LEU fuel with an alternative design of higher fissile loading. In this section we describe additional equilibrium core studies for the HEU dispersion fuel and a LEU oxide fuel. The results of these studies are summarized in Table 11. The data for the HEU, LEU, and 175 gram LEU fuels have also been included in the table for ease of comparison. In all of our equilibrium core studies comparing different fuel types, the primary constraints have been to preserve the end of cycle reactivity and core size. These constraints along with our equilibrium core model are

described in detail in Appendix B.

The HEU dispersion fuel has been analyzed because the fuel is currently being used in the FNR and thus, there is an opportunity to compare analytic predictions of discharge fuel burnup with actual core data. The conversion from HEU alloy to HEU dispersion regular fuel elements has taken place gradually starting in December 1978, with the last of the alloy fuel expected to be discharged from the core during the summer of 1981.

As shown in Table 11, our equilibrium core calculations are predicting a significant increase in fuel burnup with the conversion from alloy to dispersion fuel. The reason for this change is that with the thinner fuel clad and hence, the larger moderator fraction in the dispersion elements, the fuel is more reactive. Because of the higher reactivity, the dispersion fuel can be depleted longer in our equilibrium core model while maintaining end-of-cycle reactivity. The discharge fuel burnup is predicted to increase from 17% fissile depletion with the alloy fuel to nearly 22% with the dispersion fuel.

The predicted change in fuel burnup must be interpreted with considerable care, because discharge burnup is extremely sensitive to core criticality in our equilibrium model. A relatively small error in the calculated criticality for the two cores creates a significant error in the predicted discharge burnup. Our prediction of a significant increase in fuel burnup with the conversion to dispersion fuel has not yet been confirmed or disproven with data from the FNR. The actual fuel loading data indicates some change with dispersion fuel. On the average, core fissile loading seems to have decreased and the core average fuel element burnup has increased. But, at this time the discharge fuel burnup has increased from the 17% fissile depletion achieved with the alloy cores to only about 18% in the elements currently being discharge from the FNR.

Table 11.

Equilibrium Core Fuel Design Comparisons

	HEU		LEU		
	Nominal	UAl_x	Nominal	U_3O_8	175gm
Enrichment	93%	93%	19.5%	19.5%	19.5%
Regular element fissile loading (gm)	140.6	139.9	167.3	167.3	175.0
Uranium density in fuel meat	14.1%	14.1%	42.0%	42.0%	43.9%
Equilibrium cycle length (days)	11.0	14.85	16.5	17.75	20.8
Core fissile loading (gm)					
Beginning of cycle	4549	4351	6315	5262	5327
End of cycle	4522	4314	5274	5218	5277
Discharge burnup (MWD/element)					
Regular	19.2	26.0	28.7	30.7	36.4
Special	16.9	21.8	25.9	27.6	32.5
Burnup reactivity change rate(%Δk/k/day)					
A Rod	2.20		2.14		2.15
B Rod	2.21		2.15		2.14
C Rod	2.00		1.96		2.00
Total	6.41		6.25		6.29
Excess reactivity required (%Δk/k)					
Xenon poisoning	2.26		2.17		2.15
Burnup effect	.31		.37		.43
Power defect	.21		.24		.24
Total	2.78		2.78		2.82
Shutdown margin (%Δk/k)	3.63		3.47		3.47

The physical characteristics of the oxide fuel--including clad material, plate spacing, etc.-- are identical to the LEU fuel. The fuel meat consists of 42 w/o uranium, in the form of U_3O_8, and is clad with aluminum.

For the oxide fuel, changes in fluxes and power density are negligible except in the special elements where greater burnup occurs. The longer cycle length and corresponding increase in discharge burnup can be attributed to the presence of oxygen, which decreases the fraction of aluminum in the fuel and has a lower absorption cross section than aluminum.

An important conclusion of these studies is that, in each case, relatively small changes in fuel design caused significant gains in discharge burnup. Gains of this magnitude are possible only because of the low discharge burnup of the FNR core, which is a constraint imposed by FNR operating conditions as discussed further in Appendix B.

D. Optimized Core Loading Scheme

Improved core loading schemes have been investigated as a means of increasing core reactivity. The incentive for this preliminary analysis has been the realization that even slight increases in core reactivity may allow the fuel elements to be depleted to substantially higher burnups. In this study, as in our standard equilibrium core analysis, several important constraints have been imposed, including a constant end-of-cycle core reactivity and core size.

The basic idea behind our loading scheme was to load the least depleted fuel elements into the core locations having the highest neutron importance. In this way core reactivity can be maximized. Although these optimization techniques have been attempted and are believed to be a valid approach to the problem, no definite results are available at this time.

E. Temperature Coefficient of Reactivity and Power Defect

The HAMMER and 2DBUM codes were used to compute the isothermal temperature coefficient of reactivity for the batch fresh core model, yielding -8.4 pcm/°F for the HEU fuel and -12.6 pcm/°F for the LEU fuel. The dominant contributor in both cases is the effect of moderator density changes on leakage and moderation, with the difference due almost exclusively to Doppler effects in the LEU fuel.

As the calculational method for the power defect is still undergoing development, the difference in the isothermal temperature coefficients was used to estimate the difference in power defect between HEU and LEU fuels. As discussed further in Section VI.C of Appendix B, this results in a power defect estimate of .24% Δk/k for the LEU batch fresh test core vs. .21% Δk/k for the HEU.

VI. SAFETY ANALYSIS REPORT

The safety analysis, Utilization of LEU Fuel in the Ford Nuclear Reactor, and accompanying license amendment requesting authorization to use LEU fuel were submitted for NRC approval in October, 1979. In June, 1980 a second license amendment was submitted requesting an increase in the total number of kilograms of contained uranium on-site from 16.1 to 25. Both amendments were approved in February, 1981.

Authorized LEU fuel assemblies consist of plates containing uranium aluminide (UAl_x) in the following loadings:

Number of plates	Maximum Plate Loading (grams of ^{235}U)	Maximum Assembly Loading (grams of ^{235}U)
18	9.28 ± 2 %	167 ± 2 %
9	9.28 ± 2 %	84 ± 2 %

The increased on-site inventory will permit temporary storage during the testing of LEU elements. Along with approval of the license amendments came a requirement to submit a loss-of-coolant accident (LOCA) analysis by September, 1981. The LOCA model described in Section VIII will form a basis for the accident analysis submittal.

VII. THERMAL HYDRAULICS

Tests related to a loss of coolant accident calculation were undertaken at the FNR to determine the peak fuel temperature at the hottest spot in the reactor core following loss of coolant and to determine the maximum reactor power below which melting would not occur subsequent to loss of coolant. Previous test results from the Low Intensity Training Reactor (LITR) and the Oak Ridge Reactor (ORR) are not directly applicable to the Ford Nuclear Reactor because of differences in construction and heat transfer mechanisms between the facilities. Analytical calculations leave uncertainties as to their applicability because of significant uncertainties in heat transfer coefficients and characteristics in narrow channel flow situations similar to natural convection flow in FNR fuel elements.

The FNR plate model simulates two flow channels and three fuel plates in a fuel element. Electric heating elements provide the fission product decay heat input to each plate. The center heater simulates the plate of interest; the two outer plates act as guard heaters to minimize radial conductive and radiative heat losses.

Two distinct sets of test runs were conducted. One, with the fuel plates insulated from a base plate which simulates the core grid and heavy water tank heat sinks, permits heat dissipation by natural convection up the channels and radiation out the ends of the plates. The second in which the base plate insulator is removed includes heat dissipation by conduction to the base plate. Decay heat input values are based upon the ANS 5.1 fission product decay heat time profile. These values were increased by 20% because of uncertainties as to their accuracy.

Based on a series of eight test runs[31], the peak fuel temperature in the FNR core as the result of a loss of coolant accident following prolonged 2 MW operation is

calculated to be 800°F. Test results also indicate that the FNR could be operated continuously up to power levels of 4.0 MW without exceeding a peak fuel temperature of 1200°F, the melting point of aluminum, after suffering a loss of coolant accident. Without the core grid and heavy water tank heat sink, the values would be 965F for 2 MW operation and 3.17 MW without exceeding 1200°F.

VIII. SUMMARY AND CONCLUSIONS

In support of the whole-core demonstration of LEU fuel in the FNR core scheduled to begin in September, 1981, efforts continued during 1980 both in the experimental and analytic areas. A request for an amendment to the FNR license which would permit utilization of LEU fuel was submitted to the U. S. Nuclear Regulatory Commission, and a provisional approval has recently been granted. A series of thermal-hydraulic tests for MTR-type fuel elements was also conducted in 1980.

In the area of the demonstration experiment program, considerable progress was made during the past year in the rhodium flux mapping experiments, and the major problems in that area are nearing solution. While substantial progress was made in the areas of thermocouple power mapping, incore spectral unfolding, and excore spectral measurements, significant work still remains to complete these experiments. Further efforts will also be required in improving the accuracy in the measurements of control rod worths and other reactivity parameters.

Considerable progress was also made in the analytic areas including generic neutronic model development and neutronic analysis of LEU fuel designs. Major improvements were made in the multi-dimensional diffusion theory analysis involving the 2DBUM code, together with the implementation of the ENDF/B-IV cross section library in the LEOPARD code. Initial efforts were also made during 1980 for development of calculational models for reactivity coefficients, including power defect and void coefficient of reactivity. Similar efforts for calculation of reactor dynamics parameters were initiated with models for the effective delayed neutron fraction β_{eff}. Emphasis was also placed on providing efficient links among various computer codes, with special applications to control rod worth calculations. Further comparison between the calculated results and the

FNR data continued during 1980, including a simulation of 330 full power days of operation with the 2DBUM code.

In confirmation of fuel specifications for the LEU fuel selected for testing at the FNR, further comparisons between the LEU and HEU fuels were performed in 1980. This included comparison of the calculated void coefficients of reactivity and control rod worths. Equilibrium core analysis of alternative LEU fuel designs was also undertaken during the year.

Efforts are continuing for development of methods for accurately predicting ex-core neutron flux distribution in the FNR. Improvements will also be required in analytic, as well as experimental, determination of reactivity coefficients, control rod worth and reactor dynamics parameters for the FNR core. Future refinements in the computer code system will include development of a three-dimensional capability within the 2DBUM code, and consolidation of the ENDF/B-IV library, new fission product poisoning correlation and updated physical constants in the form of a new version of the LEOPARD code. In preparation for the LEU testing in September, 1981, actual detailed loading calculations and optimal equilibrium core calculations are expected to be initiated some time during this summer.

Thermal-hydraulic testing of simulated FNR fuel elements performed to date suggests that there would be an adequate margin for the FNR operation at 2 MWt, even in the case of a postulated loss-of-coolant accident. Some further analysis will be necessary in the near future to supply information to the U. S. Nuclear Regulatory Commission in connection with the design basis accident analysis required in our latest license amendment.

REFERENCES

1. Low Enrichment Fuel Evaluation and Analysis Program, Summary Report for the Period January, 1979 - December, 1979, Department of Nuclear Engineering and Michigan-Memorial Phoenix Project Report, University of Michigan (January,1980).

2. D. K. Wehe and J. S. King, Trans. Am. Nucl. Soc., 34, 746 (June 1980).

3. J. M. Carpenter, R. F. Fleming, and H. Bozorgmanesh, Trans. Am. Nucl. Soc., 22, 606 (November 1975).

4. D. K. Wehe and J. S. King, Trans. Am. Nucl. Soc., 35, 571 (November 1980).

5. J. E. Tucker, "Thermocouple Probe Report for the Low Enrichment Project," Department of Nuclear Engineering Internal Report, University of Michigan (January 31, 1981).

6. R. F. Barry, "LEOPARD- A Spectrum Dependent Non-Spatial Depletion Code", WCAP-3269-26, Westinghouse Electric Corporation (Sept. 1963).

7. J. Barhen, W. Rothenstein, E. Taviv, "The HAMMER Code System", NP-565, Electric Power Research Institute (October 1978).

8. T. R. England, W. B. Wilson, and M. G. Stamatelatos, "Fission Product Data for Thermal Reactors, Part 2- Users Manual for EPRI-CINDER Code and Data", EPRI-NP-356, Electric Power Research Institute (Dec. 1976).

9. W. W. Little, Jr. and R. W. Hardie, "2DB User's Manual-Revision I", BNWL-831 REV1, Battelle Pacific Northwest Laboratory (February 1969).

10. F. B. Brown, D. C. Losey, D. K. Wehe, J. C. Lee, and W. R. Martin, Trans. Am. Nucl. Soc., 33, 746 (1979).

11. Private Communication, W. D. Henderson, Westinghouse Electric Corporation, to J. C. Lee, University of Michigan (August 1, 1980).

12. C. L. Beard and R. S. Dannels, "ETOT- A FORTRAN IV Program to Process Data from the ENDF/B File to Thermal Library Format", WCAP-7363, ENDF-146,Westinghouse Electric Corporation (1971).

13. D. E. Kusner and R. S. Dannels, "ETOG-1, A FORTRAN IV Program to Process Data from the ENDF/B File to the MUFT, GAM, and ANISN Format", WCAP 3845-1, Westinghouse Electric Corporation (1969).

14. R. E. Prael and L. J. Milton, "A User's Manual for the Monte Carlo Code VIM", FRA-TM-84 (1976).

15. Advance Recycle Methodology Program System Documentation, EPRI-CELL Code Description , Part II, Chapter 5 by Electric Power Research Institute (1977).

16. W. L. Woodruff, "Comparison of EPRI-CELL and VIM (Monte Carlo) Generated Microscopic Cross-section Data for a Slab Cell Representative of MTR-type Research and Test Reactors Using Highly-enriched and Reduced-enrichment Uranium Fuels", Argonne National Laboratory Internal Memorandum (January 3, 1979).

17. J. Hardy, D. Klein, and J. J. Volpe, "A Study of Physics Parameters in Several Water-Moderated Lattices of Slightly Enriched and Natural Uranium", WAPD-TM-931, Westinghouse Electric Corporation (March, 1970).

18. D. R. Ferguson and K. L. Derstine, Nucl. Sci. Eng., 64, 593 (1977).

19. R. W. Hardie and W. W. Little, Jr., "3DB, A Three-Dimensional Diffusion Theory Burnup Code", BNWL-1264, Battelle Northwest Laboratory (1970).

20. D. R. Vondy, T. B. Fowler, and G. W. Cunningham, "VENTURE: A Code Block for Solving Multigroup Neutronics Problems Applying the Finite-Difference Diffusion Theory Approximation to Neutron Transport", ORNL-5062, Oak Ridge National Laboratory (1975).

21. F. B. Brown, W. R. Martin, D. A. Calahan, "A Discrete Sampling Method for Vectorized Monte Carlo Calculations", Trans. Am. Nucl. Soc. (To be published June, 1981).

22. L. L. Carter and C. A. Forest, Nucl. Sci. Eng., 59, 27 (1976).

23. D. R. Harris, "ANDYMG3, the Basic Program of a Series of Monte Carlo Programs for Time-Dependent Transport of Particles and Photons", LA-4539, Los Alamos Scientific Laboratory (1970).

24. A. F. Henry, "The Application of Reactor Kinetics to Analysis of Experiments", Nucl. Sci. Eng., 3, 52 (1958).

25. S. Kaplan and A. F.Henry, "An Experiment to Measure Effective Delayed Neutron Fraction", WAPD-TM-209, Westinghouse Electric Corporation (1960).

26. R. J. Tuttle, "Delayed Neutron Data for Reactor Analysis", Nucl. Sci. Eng., 56, 37 (1975).

27. D. Saphier, et al., "Evaluated Delayed Neutron Spectra and Their Importance in Reactor Calculations", Nucl. Sci. Eng., 62, 660 (1977).

28. R. W. Hardie and W. W. Little, Jr., "PERTV- A Two Dimensional Code for Fast Reactor Analysis," BNWL-1162, Battelle Pacific Northwest Laboratory (Sept. 1969).

29. R. M. Westfall et al., "SCALE: A Modular Code System for Performing Standardized Computer Analysis for Licensing Evaluation," NUREG CR-0200, Distributed by the Radiation Shielding Information Center, Oak Ridge National Laboratory (1980).

30. P. N. Cooper et al.,"Some Measurements of Reactivity in a Light-Water Moderated Highly Enriched Uranium Assembly", React. Sci. Tech., 16, 65 (1962).

31. "Ford Nuclear Reactor Loss of Coolant Accident Tests Utilizing an Electrically Heated Fuel Plate Model", The University of Michigan, Ann Arbor, Michigan (September, 1980).

APPENDIX A

The RERTR Demonstration Experiments Program at the Ford Nuclear Reactor

The RERTR Demonstration Experiments Program at the Ford Nuclear Reactor

by

D.K. Wehe and J.S. King
Department of Nuclear Engineering
University of Michigan
Ann Arbor, Mich. 48109

The purpose of this paper is to highlight a major part of the experimental work which is being carried out at the Ford Nuclear Reactor (FNR) in conjunction with the RERTR program. A demonstration experiments program has been developed to:

1) characterize the FNR in sufficient detail to discern and quantify neutronic differences between the high and low enriched cores.
2) provide the theoretical group with measurements to benchmark their calculations.

As with any experimental program associated with a reactor, stringent constraints limit the experiments which can be performed. Some experiments are performed routinely on the FNR (such as control rod calibrations), and much data is already available. Unfortunately, the accuracy we demand precludes using much of this earlier data. And in many cases, the requirement of precise (and copious) data has led to either developing new techniques (as in the case of rhodium mapping and neutron diffraction) or to further refinements on existing methods (as in the case of spectral unfolding). Nevertheless, we have tried to stay within the realm of recognized, well-established experimental methods in order to assuage any doubts about measured differences between HEU and LEU core parameters. With these caveats in mind, the experiments which have been chosen to accomplish these tasks are:

A. Wire activation measurements to provide absolute flux normalization (limited spectral and spatial information).
B. Rhodium detector flux maps to provide absolute thermal (in-core and ex-core) fluxes.
C. Thermocouple ΔT maps to provide absolute power distributions.

D. Unfolded foil activation measurements to determine the in-core flux spectrum.

E. Neutron diffraction measurements to determine the flux spectrum in the D_2O reflector.

F. Shim and control rod worth ($\%\Delta k/k$), void coefficient, power defect, xenon worth, and temperature coefficient measurements to determine reactivity parameters.

The following sections of this paper describe the principal results of the experiments performed so far. However, the reactivity measurements use such traditional techniques (such as the asymptotic period method[1], to measure the control rod worth) that they are not described here. The paper is written with the philosophy that the reader is familiar with standard techniques. It should be emphasized that the experimental program has not been finished. Additional refinement and repetition of the experiments (particularly C, D, and E above is continuing). Regarding the rhodium flux maps, application of the rhodium detector transfer function analysis (described later) makes full-core rhodium flux maps a much quicker process. Lastly, some of the actual experimental work associated with the spectral unfolding still remains to be completed. Nevertheless, the results detailed in this paper represent a major part of the experimental characterization of the highly enriched FNR core.

A. Wire Activations for Absolute Flux Normalization

1. Purpose

The purpose of this phase of the experimental program was two-fold:

(i) to provide measured values of the thermal flux in the core and D_2O tank for comparison with the results being generated by the 2DB code.

(ii) to provide a means of absolute determination of the sensitivity of the rhodium detector (to be discussed in the next section).

2. Axial Flux Determination

a) Thermal flux determination

In order to obtain a measured value of the thermal flux, bare and cadmium covered iron wires were irradiated. The iron reaction:

$$Fe^{58}(n,\gamma)\ Fe^{59}$$

was used since the cross section varies as 1/v below 0.1 keV. The analysis closely follows that of Beckurts and Wirtz[2].

The fact that the cross section varies as 1/v makes the evaluation of the thermal cutoff energy, the cadmium cutoff energy, and cadmium correction factor very straightforward, and yields

E_{Tc} = thermal cutoff energy = 0.089 eV

E_{cc} = cadmium cutoff energy = 0.55 eV

and F_{cD} = 2.5 = cadmium correction factor.

It should be mentioned that for all activations performed, we have neglected corrections for self shielding, flux depression, and scattering in the foils, assuming they are small. Ge-Li detectors, calibrated with an NBS standard, were used in the counting.

The thermal flux determined by wire activations done axially along the core center is shown in Figure 1. The data "points" are shown as bars since the 1" long wire segments actually integrate the flux over this distance. Note that the thermal flux reflector peaking is responsible for the increased values near the ends of the fuel plate. The fact that the flux peaks slightly below the core midplane is attributable to the location of the shim rod bank. The results have been compared to earlier measurements on the FNR, and were found to be in good agreement.

b) Intermediate "thermal" flux

The results generated by the computer codes, (such as LEOPARD and 2DB) will not agree with the results presented in Figure 1. The reason for this lies in their definition of the thermal flux. It is a common practice to define the thermal flux using the cadmium cutoff energy E_{cc} as the upper limit. For this reason, we define an "intermediate thermal flux", as:

$$\phi_{IT} = \int_{E_{tc}}^{Ecc} \phi(E)dE$$

In this energy region, the flux is assumed to behave as 1/E. Then the "intermediate thermal flux" may be evaluated as:

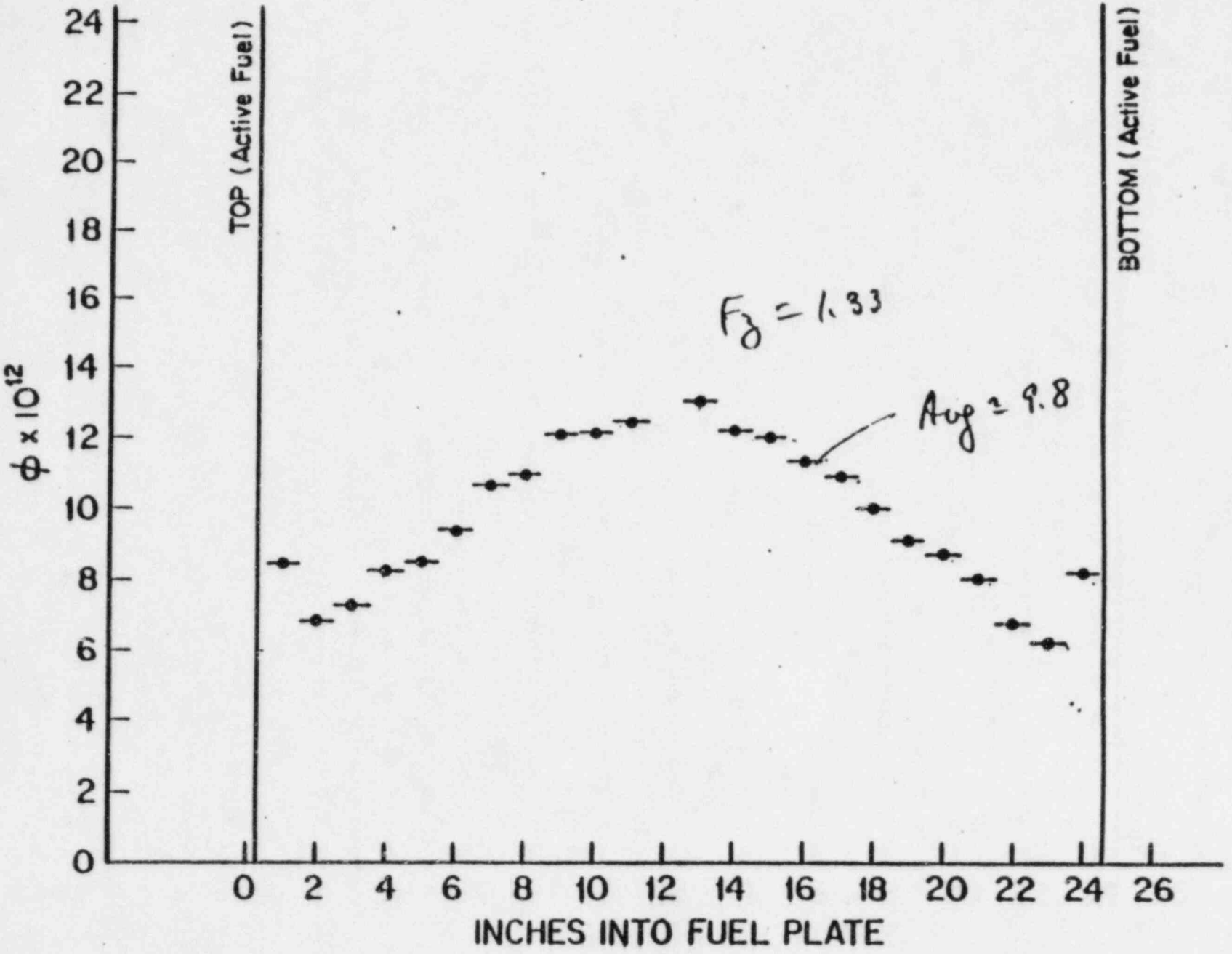

Figure 1. Wire Activation Results for ϕ_{th}
-Location L-37-

$$\bar{\Phi}_{1T} = \bar{\Phi}_0 \ln\left(\frac{E_{cd}}{E_c}\right)$$

The activity from the cadmium covered iron wire $Fe^{58}(n,\gamma)Fe^{59}$ reaction can be used to determine $\bar{\Phi}_0$, and hence $\bar{\Phi}_{1T}$ (or any integral flux in the 1/E range).

The correct flux from the iron wire results to compare with the computer generated "thermal flux" is thus

Figure 2 presents $\bar{\Phi}_{th} + \bar{\Phi}_{1T}$ for the axial center-of-core irradiations described above. The addition of $\bar{\Phi}_{1T}$ adds as much as 10%, at the core center, to the value of $\bar{\Phi}_{th}$, and brings computer calculated fluxes closer to the measured fluxes. Also presented on Figure 2 are the results of an axial rhodium detector flux map made on the same fuel element. The rhodium points are based on the manufacturer's detector sensitivity and are uncorrected for epithermal neutrons. The large disagreements in the values of the flux are attributable to these epithermal neutron contributions to the rhodium detector signal, and are discussed in detail in section B. There the measured values of $\bar{\Phi}_{th} + \bar{\Phi}_{1T}$ are used to calculate the sensitivity of the rhodium detector in the FNR.

c) Fast Flux

An additional benefit from activating iron is the threshold reaction:

$$Fe^{54}(n,p)\,Mn^{54}$$

which has a threshold at $\simeq 3.75$ MeV.

Defining a fast flux as:

$$\bar{\Phi}_F = \int_{4\,MeV}^{\infty} \Phi(E)\,dE$$

one can obtain

$$\bar{\Phi}_F = \frac{R}{N\sigma_{eff}}$$

where $\frac{R}{N}$ = saturated Mn^{54} activity per unit Fe^{54} nucleus.

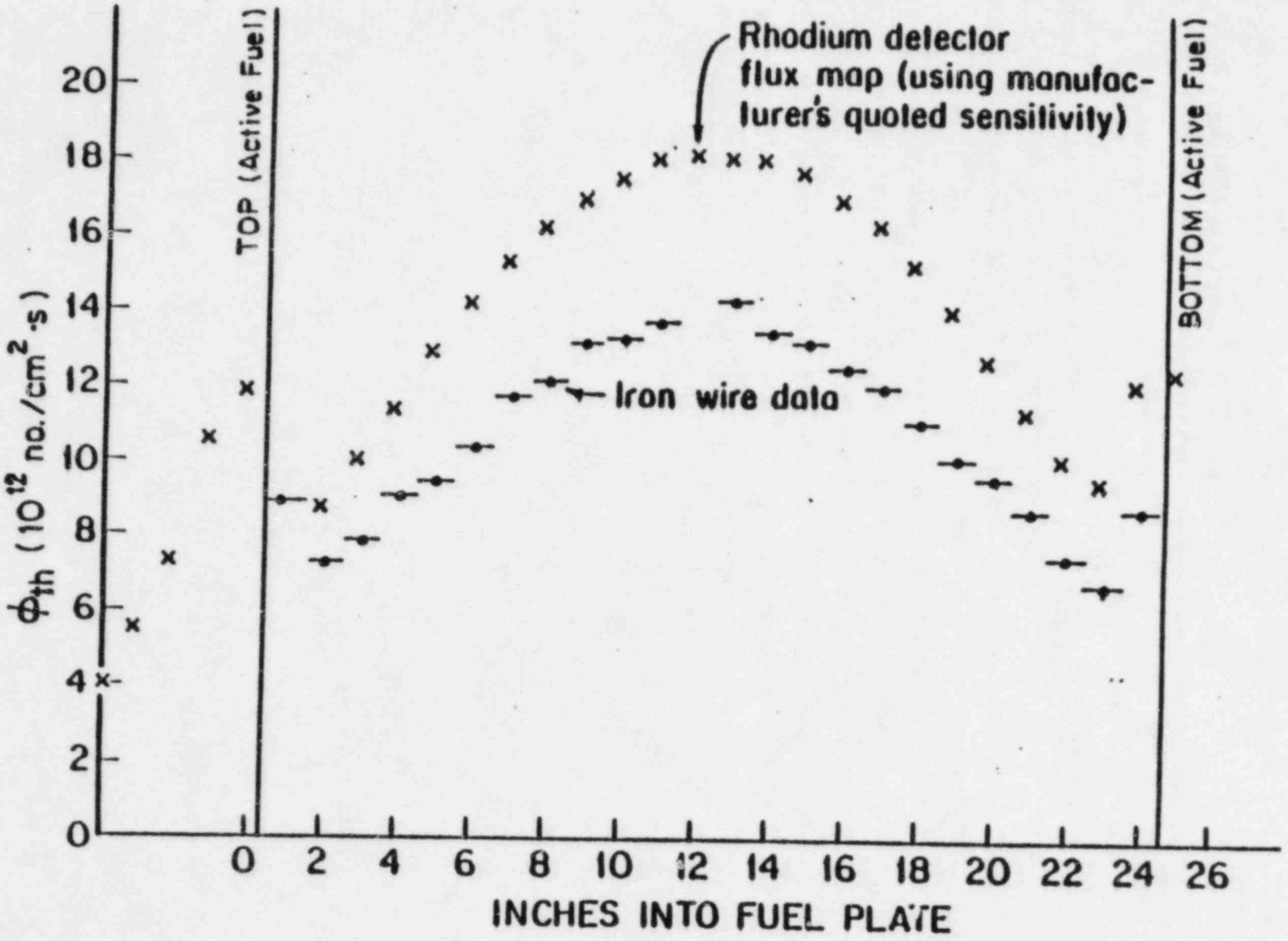

Figure 2. Wire Activation Results for $\phi_{th}+\phi_{IT}$

-Location L-37-

Thus, from the measurement of the Mn^{54} activity, one can obtain a measure of the fast flux, as defined above. Figure 3 shows the results of the measurement. Note that the flux scale is an order of magnitude smaller than for figures 1 and 2, indicating the smaller size of this fast flux. The noticeable shift of the flux towards the bottom of the core has been discussed earlier.

Additional measurements of the fast flux using the threshold reaction:

$$Al^{27}(n,\alpha)\ Na^{24}$$

with a threshold of ≈8.15 MeV were made. The analysis was performed as outlined above, and yielded the energy integrated flux above 8 MeV. As might be expected, the results look like Figure 3 on a smaller scale.

d) Ratio of fast to thermal flux

Lastly, it is expected that the ratio of fast to thermal flux will change with the introduction of low-enriched fuel. One measure of this, (besides taking ratios of Figures 1, 2, and 3) is the cadmium ratio. The iron cadmium ratio remained approximately constant in the core (except near the edges of the fuel) at about 9.7. The fact that the spectrum does not vary significantly throughout the normal fuel elements in the core greatly simplifies the measurements of the rhodium detector correction factors, as described in section B.

3. Radial Flux Determination

One of the difficulties encountered in attempting to compute the flux in the D_2O reflector is the complex structure inside the tank. In order to provide benchmark values of the flux, bare and cadmium covered iron wire irradiations were performed in the vertical penetrations of the D_2O tank.

A photograph of the D_2O tank is shown in Figure 4. The vertical penetrations into the D_2O tank are the 13 small, 1" inner diameter, pipes on the tank's top. These pipes extend down to within a few inches of the core midplane, and are filled with H_2O. Figure 5 shows the spacing between penetrations, and the names associated with them, (e.g., D_2O tank position S I. This nomenclature will be used throughout the rest of the paper for specifying locations in the D_2O tank.

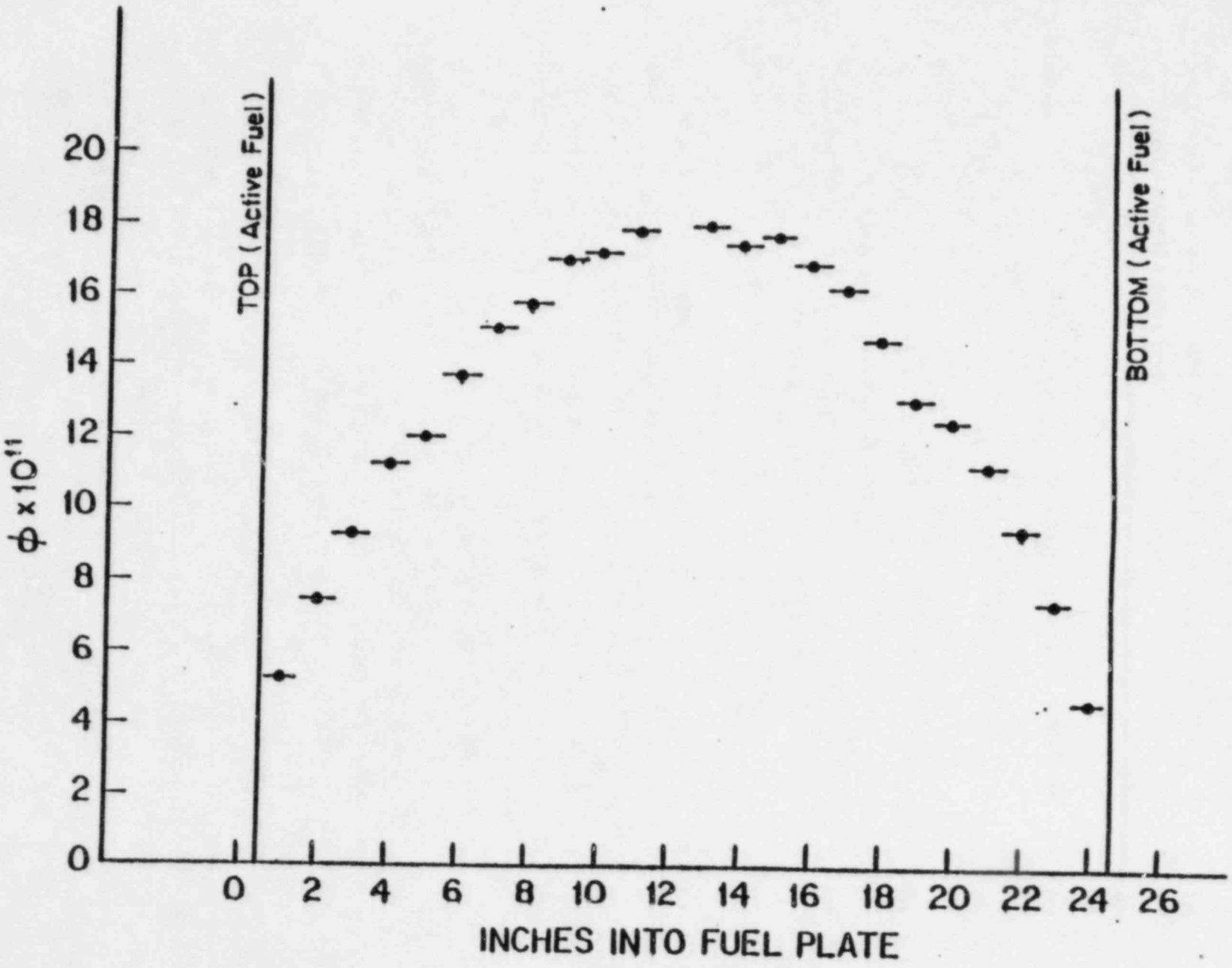

Figure 3. Wire Activation Results for ϕ_F
-Location L-37-

Core side

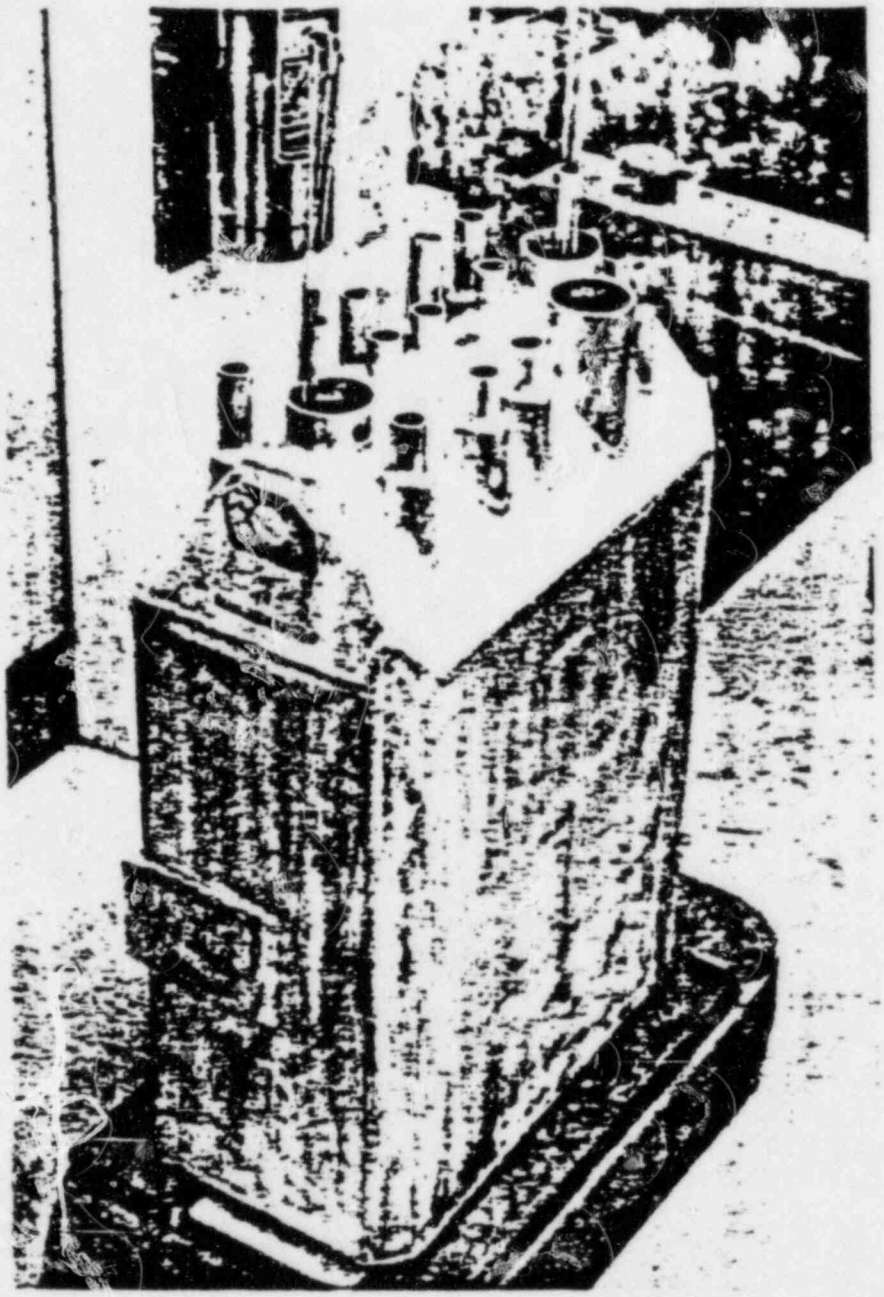

North side

Figure 4. D_2O Tank

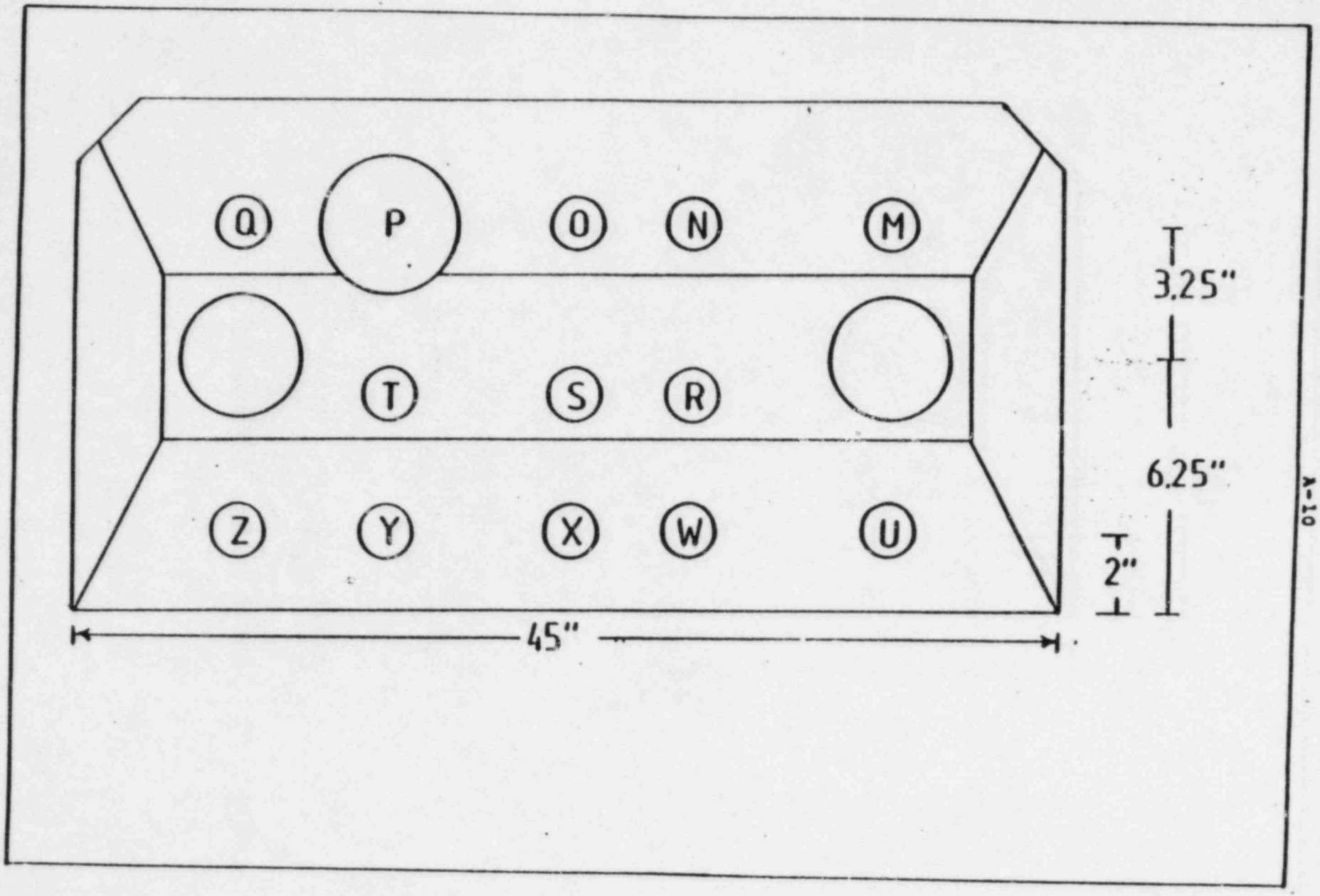

Figure 5. D_2O tank layout.

Bare and cadmium covered iron wires were irradiated in D_2O tank positions O and X. The results for the core center, and for D_2O tank positions O and X at an axial position 2" above the core midplane, are presented in Table 1. The thermal flux is seen to fall off much slower in the D_2O tank as compared to an H_2O reflector (see rhodium detector flux mapping data, section B). This is exactly what is expected. Further, the thermal flux quoted for D_2O tank position X is in good agreement with previously measured values. The values of $\Phi_{th} + \bar{\Phi}_{rr}$ are being used by the analytical group to fix the D_2O tank parameters for the computer calculations. The iron cadmium ratios are presented for future comparisons with low enriched fuel.

4. Conclusion

While the results presented in this section provide information on the fast and thermal fluxes for computer calculation comparisons and position dependent spectrum variations, they will also play an essential role in the calibration of the rhodium detector discussed in the next section.

B. Rhodium Detector Thermal Flux Mapping

1. Purpose and Introduction

The purpose of this phase of the experimental program was to measure the <u>thermal flux</u>* at many locations in the core and reflectors, in order to:

i) provide measured values to the analytic group performing the computer calculations. This ensures the codes are generating realistic results and provides additional confidence in their projections to low-enriched fuel.

ii) characterize the thermal flux profile associated with highly enriched fuel in order to quantitatively discern the changes associated with switching to low enriched fuel.

A rhodium self-powered neutron detector was chosen to accomplish the goals

---

*In contrast to Section A, the "thermal flux" in this section is defined as: $\Phi_{th} = \int_0^{E_{Cd}} \phi(E)dE$ where the value of the upper integrand has been changed to the cadmium cut-off energy.

Table 1. Comparison of Energy Integral Fluxes

	Core Center	D_2O Position X	D_2O Position O
Φ_{th}	1.21×10^{13}	$.913 \times 10^{13}$	$.287 \times 10^{13}$
Φ_{IT}	(0.117×10^{13})	$(.451 \times 10^{12})$	$(.169 \times 10^{11})$ $(\pm 13\%)$
Φ_{F}	0.172×10^{13}	0.139×10^{12}	negligible ($< 10^{9}$)
R_{Cd}(Fe)	9.72	16.67	128

because:

i) its size, mobility, and sensitivity are such that it can measure the thermal flux at any axial point in almost any core lattice position,

ii) the time required to obtain a measured flux, once the sensitivity is known, is much less than for a wire activation, and

iii) the uncertainty in the measured value is comparable to that obtained from wire activations.

This section briefly describes the physics associated with the rhodium self-powered neutron detector, the equipment used to perform the measurements, and the determination of the detector sensitivity. The results of axial and radial measurements are then presented. Finally, a technique being developed which may eliminate the most serious drawback in using the rhodium detector for full-core thermal flux maps is addressed.

2. Theoretical Description of Rhodium Detectors

The operation of a rhodium self-powered neutron detector is based on the rhodium nuclear reaction:

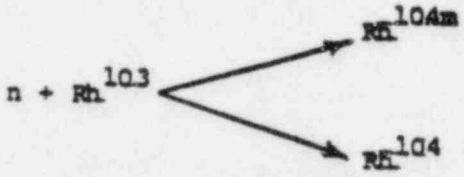

A closer examination of the rhodium decay scheme (Figure 6) brings to light two important factors of the rhodium detector. First, the relatively high rhodium absorption cross section implies a relatively high neutron sensitivity. Indeed, rhodium has the highest sensitivity of any type of self-powered neutron detector. For the FNR, it is the only commercially available material which will yield large enough signals to give precision data. In Figure 7, the energy dependence of the rhodium absorption cross section is shown. The large resonance at 1.25 eV implies that the detector is also measuring neutrons in the epithermal range. Since the thermal flux is required, epithermal corrections need to be applied to the detector current, and are described later. Secondly, the presence of the metastable state of Rh-104, with its 4.4 minute half life, implies that the current may take several minutes to reach its equilibrium value after a change in flux. This can be seen more precisely by writing the appropriate rate

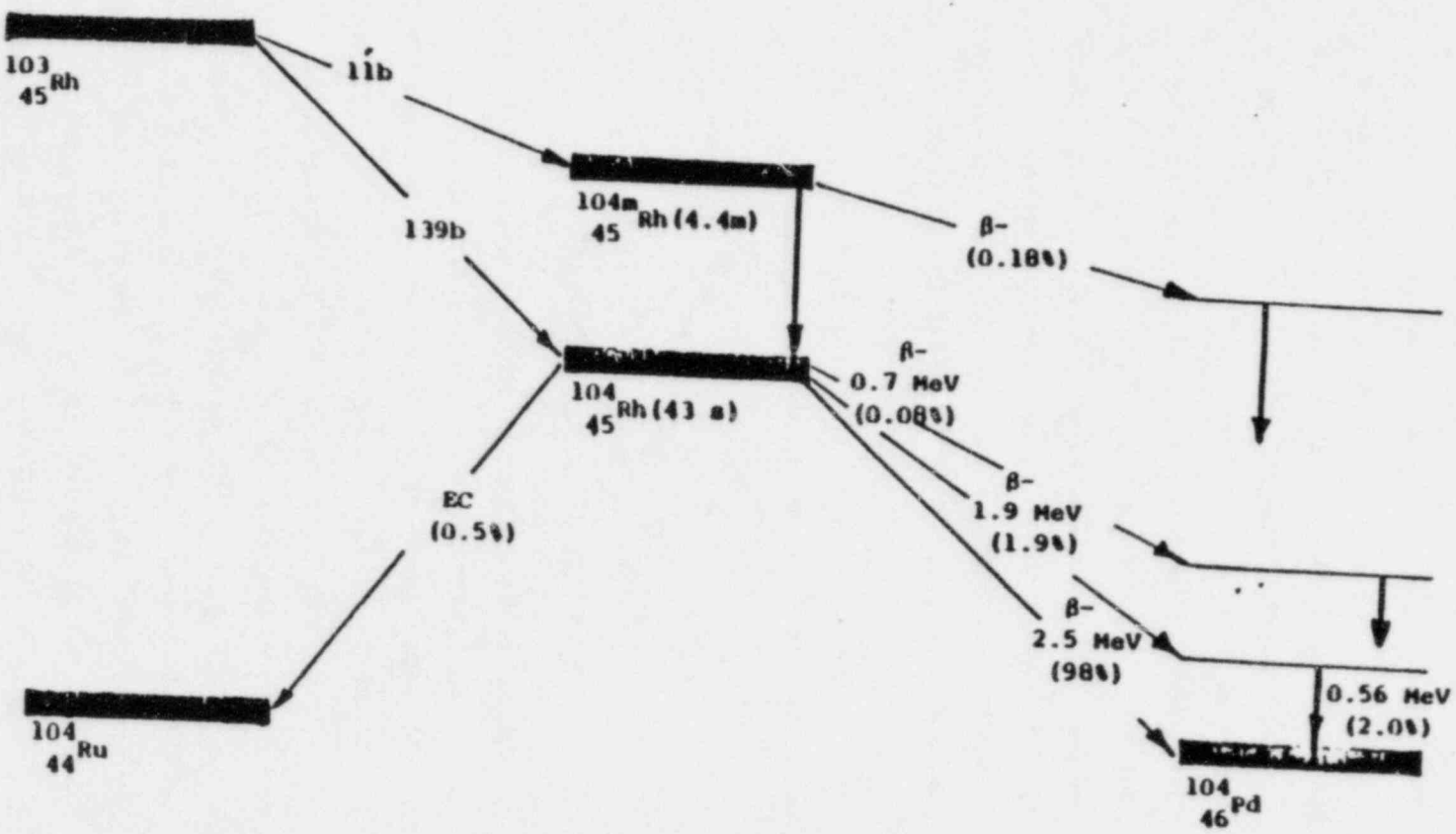

Figure 6. Rhodium Decay Scheme

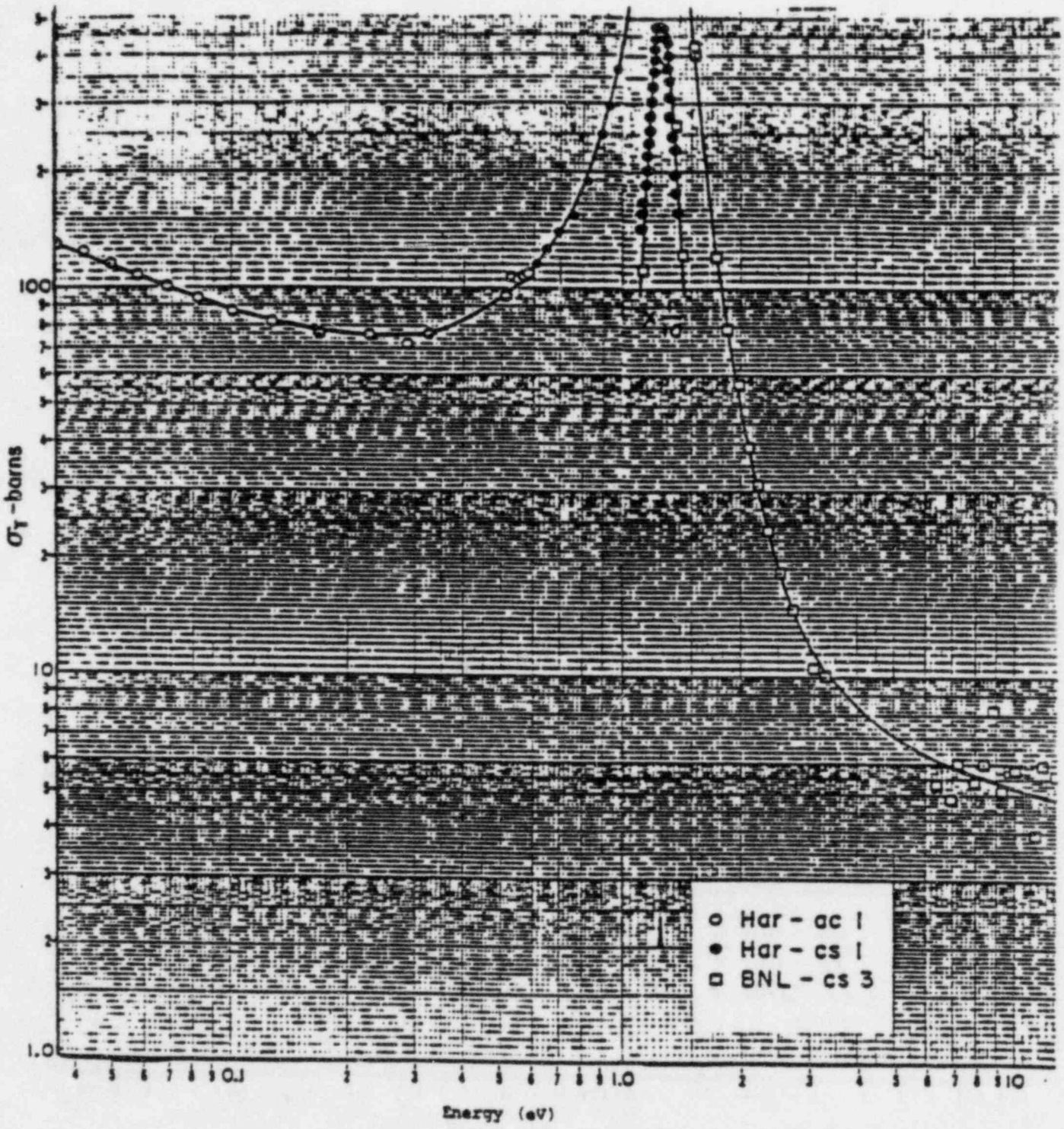

Figure 7. Rhodium Absorption Cross Section
(from BNL-325 - Second Edition)

equations and current equation for one energy group, and solving for the current. It can be shown that, following a step change in the flux at t=0, the time dependence of the current can be approximated by:

$$I(t) \approx I_o + \Delta I\left(1 - .088\, e^{-\lambda_m t} - .912\, e^{-\lambda_g t}\right) = I_o + \Delta I\, f(t),$$

where I_o = initial equilibrium value of current for $t \leq 0$.

ΔI = change in the equilibrium value of the current as the result of the step change in flux

λ_m, λ_g = decay constants for the Rh^{104} ground and metastable states.

$f(t)$ = the time dependent function contained in parenthesis.

Using the above relationship yields:

t(minutes)	$\frac{I(t)-I_o}{\Delta I}$
1	58%
2	81%
3	90%
5	95%
7	97%
9	98%
10	98%

In constructing this table, it is clear that the 4.4 minute half life of Rh^{104m} leads to the requirement of ~10 minute waittimes for ~98% of the current change to occur. However, the quantity of interest is usually the error in the measured current, which is defined as:

$$\epsilon(t) = \left|1 - \frac{I(t)}{I_f}\right|$$

where I_f is defined as the equilibrium value of the current after the flux change.

Using the above relations, algebra yields:

$$\epsilon(t) = (1-f(t))\left|1-\frac{I_o}{I_f}\right| = (1-f(t_i))\left|\frac{1}{1+\frac{f(t)}{\left(\frac{I(t)}{I_o}-1\right)}}\right| \qquad A-17$$

The second expression is useful for on-line estimates of the detector current error as a function of time. Using the first relationship for a fixed value of the wait time, one can tabulate $\epsilon(t)$. For a wait time of 3 minutes, for example, we obtain

$\frac{I_o}{I_f}$	$\epsilon(t)$
.38	1.7%
1.2	2 %
.5	5 %
2	10 %
.1	9 %
10	90 %

This shows that, for a given wait time, the detector should be moved into regions of increasing flux to minimize the error in the current. Or conversely, longer wait times are required for a given error in the current if the detector is moved in the direction of decreasing flux. Thus, while wait times on the order of several minutes are expected, the actual wait times required for a given error in the current cannot be predicted a priori*, but can be minimized through a judicial choice of detector measurement positions.

3. Equipment Description

In order to carry out this experimental program, several pieces of equipment were designed and fabricated. These are briefly discussed below.

The rhodium self-powered neutron detector (SPND) is shown in Figure 8. A bare lead, parallel to the emitter lead, is not shown on the figure, but was used to measure the current background. The detector was mounted on a

---

*The easily derivable expression: $I_f = I_o + (1/f(t))[I(t) - I_o]$ cannot be repeatedly used to shorten the wait time since I_o represents an equilibrium current prior to the step flux change. Techniques to eliminate the wait times are discussed later.

paddle designed to minimize flux perturbations, and can be accurately positioned at any axial location in a regular or special fuel element.

Special adapters were built to allow the SPND assembly to be used in the vertical penetrations into the D_2O tank (see Figure 4). These adapters sit on the vertical D_2O tank pipes, and provide a reference height and centering bar for the SPND assembly.

A special adapter was designed and built to measure the flux in the H_2O reflector south of the core. This adapter looks very similar to a regular fuel element, except that it has four vertical channels for the detector specifically located to bracket the anticipated narrow thermal flux peaking in the reflector. The adapter fits into an extension of the core grid plate, and rests snugly against a regular fuel element.

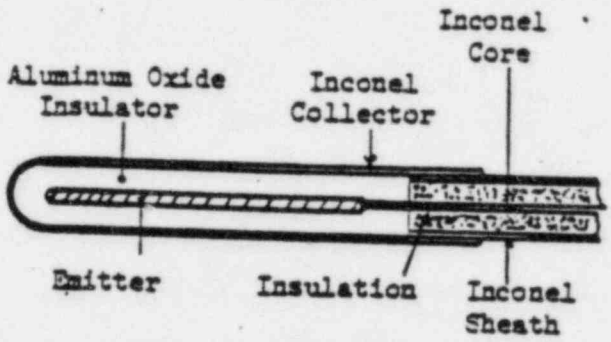

Figure 8. SPND Construction

4. Determination of Detector Sensitivity

In order to transform the measurements of current into flux values, the sensitivity of the detector, S, must be known, i.e.

$$S = \frac{I}{\Phi}$$

This parameter plays a crucial role in the data analysis, and its accurate determination is the subject of this section.

One technique to determine S is based on the theoretical calculations of Warren.[3] The model he proposes includes the effects of 2200 m/sec neutron self-shielding in the emitter wire, the energy loss of the electrons in traversing the insulator and emitter, and correction for space-charge buildup on the insultator. A prescription is presented for determining the sensitivity of various types of detectors with different insulators and geometries. In general, the model is said to give reasonable agreement

between measured and calculated sensitivities. When applied to our detector, Warren's model yields 2.97×10^{-21} amps/nv . The manufacturer's quoted sensitivity is 3×10^{-21} amps/nv , close to the calculated value.

In a more recent work, Laaksonen[4] points out that "several simplifying assumptions were made in (Warren's) model which, in the case of a rhodium SPND in a relatively hard spectrum might be too rough. For example, it was assumed that the electron source in the emitter wire is spatially flat, and only 2200 m/sec neutrons were considered." Laaksonen shows that the sensitivity can be strongly spectral dependent, and hence brings into question the validity of the sensitivity which is calculated above. Furthermore, he notes that the manufacturer's quoted sensitivities are usually given as electric current per unit 2200 m/sec flux. For reactors with a spectrum different than that used in the calibration of the sensitivity, the manufacturer's value may not be appropriate. Finally, when the manufacturer's sensitivity was applied to the FNR rhodium detector data, the fluxes did not agree with the iron wire data presented earlier.

As a result of these uncertainties, a program to determine the absolute sensitivity of the rhodium detector used in the FNR spectrum was developed. Define:

$\underline{x}$ = position vector

$f_{th}(\underline{x})$ = fraction of detector current which is attributable to neutrons with energy below the cadmium cutoff energy, (E_{cc}).
= "epithermal correction factor"

$I_{th}(\underline{x})$ = "thermal" detector current = detector current which is attributable to neutrons with energy below E_{cc}.

$I_{tot}(\underline{x})$ = total net detector current

$\bar{\Phi}_{th}(\underline{x})$ = thermal flux

Using these quantities, the sensitivity of the detector to thermal neutrons can be written as:

$$S_{th}(\underline{x}) = \frac{I_{tot}(\underline{x})}{\bar{\Phi}_{th}(\underline{x})} = \frac{I_{th}(\underline{x})}{f_{th}(\underline{x})\,\bar{\Phi}_{th}(\underline{x})}$$

If the thermal current per unit thermal flux is assumed position independent*, and defined as S_I, then

$$S_{th}(\underline{x}) = \frac{1}{f_{th}(\underline{x})} S_I$$

To determine S_I, where

$$S_I = \frac{I_{th}}{\Phi_{th}} = \frac{f_{th}(\underline{x})\, I_{TOT}(\underline{x})}{\Phi_{th}(\underline{x})}$$

measured values of $\Phi_{th}(\underline{x})$, $I_{TOT}(\underline{x})$, and $f_{th}(\underline{x})$ are needed. The iron wire data of Section A is used to provide $\Phi_{th}(\underline{x})$**, the measurement of $f_{th}(\underline{x})$ is disucssed below, and $I_{TOT}(\underline{x})$ comes from the rhodium detector. Using several axial positions at the core center, we find

$$S_I = 3.76 \times 10^{-21} \ \frac{\text{"thermal" amps}}{\text{thermal flux}}$$

which represents a 9% increase over the manufacturer's quoted sensitivity. The plots which follow use $S_I = 3 \times 10^{-21} \frac{\text{thermal amps}}{\text{thermal flux}}$ since this improved value was not available at the time the plots were drawn. Hence, all plot values should be corrected to account for this 9% difference.

Thus, to determine the thermal sensitivity of the detector requires an evaluation of $f_{th}(\underline{x})$, the fraction of detector current attributable to thermal neutron absorption in the rhodium emitter. This quantity was measured at various positions, in and around the core, by activation of bare and cadmium covered rhodium wires. From the count rates of wires irradiated at position $\underline{x}$, one can determine $f_{th}(\underline{x})$ as:

$$f_{th}(\underline{x}) = 1 - \frac{A_{cd}(\underline{x},t)}{A_b(\underline{x},t)}$$

where $A_{CD}(\underline{x},t)$ = specific activity at time t of the cadmium covered rhodium wire irradiated at position $\underline{x}$

and $A_b(\underline{x},t)$ = specific activity at time t of the bare rhodium wire irradiated at position $\underline{x}$.

---

*It has been shown that the thermal current per unit thermal flux is strongly dependant on the effective neutron tamperature due to the non-1/v behavior of rhodium in the thermal energy region. Thus, the assumption is that the effective neutron tamperature is position independant. The results obtained from spectral unfolding in the thermal region (described in Section D) will be used to check the validity of this approximation and make any needed corrections.

** It is implicitly assumed that the cadmium cutoff energy for iron is approximately equal to the cadmium cutoff energy for rhodium.

Because the rhodium wire activates so easily, has a short half-life, and long-lived impurities, the irradiations were performed at 100 kW to reduce their saturated activities.* Even so, the wires needed to be cut remotely (to 3/8") for unshielded counting and handling. The experimental group found that, with experience, the wires could be counted within ten minutes after the irradiation. A similar experimental technique has been used by Baldwin and Rogers[5] to study the effect of varying boron concentrations on the rhodium detector response. While they chose to count the emitted electrons with proportional counters, the present experiments used GeLi detectors to count the .555 MeV gamma rays (See Figure 6).

The experimental results for $f_{th}(\underline{x})$ are presented in Table 2. Radial locations are keyed to Figure 9. As can be seen from the data for L-37 (center of core), L-40 (core edge), and L-67 (regular fuel element next to a special fuel element), the value of $f_{th}(\underline{x})$ in the core does not vary greatly**(with the exception of special fuel elements). This is consistent with computer code predictions. As a result, a single value of $f_{th}(\underline{x}) \approx .8$ could have been applied to all <u>regular</u> fuel elements in the core without substantial error. Values for the epithermal correction factor are also presented for the H_2O reflector, special fuel element, and two D_2O tank locations. Values of $f_{th}(\underline{x})$ in locations which were not directly meausured were interpolated from these measured results. For the H_2O reflector, the value of $f_{th}(\underline{x})$ measured in the second channel (outward from the core) is assumed applicable for all four channels. This is probably an acceptable approximation since the measured value of $f_{th}(\underline{x}) = .93$ is already close to unity and should not vary by more than a few percent either way in the other channels.

Thus, with values of $f_{th}(\underline{x})$ defined for all points in the core, south H_2O reflector, and D_2O tank, the thermal sensitivity of the detector,

$$S_{th}(\underline{x}) = \frac{1}{f_{th}(\underline{x})} \cdot S_I$$

becomes a known function of position, and the thermal flux can be determined from rhodium detector net current readings as:

---

*Throughout this section, it is assumed that the spectrum does not change significantly as a function of FNR core loadings or power level. All measurements were made at or near 2 MW equilibrium xenon, however.

**The epithermal correction factor is also assumed constant axially. This will be true except within a couple of inches at the ends of the fuel plates, as was shown by iron wire cadmium ratio measurements (Section A).

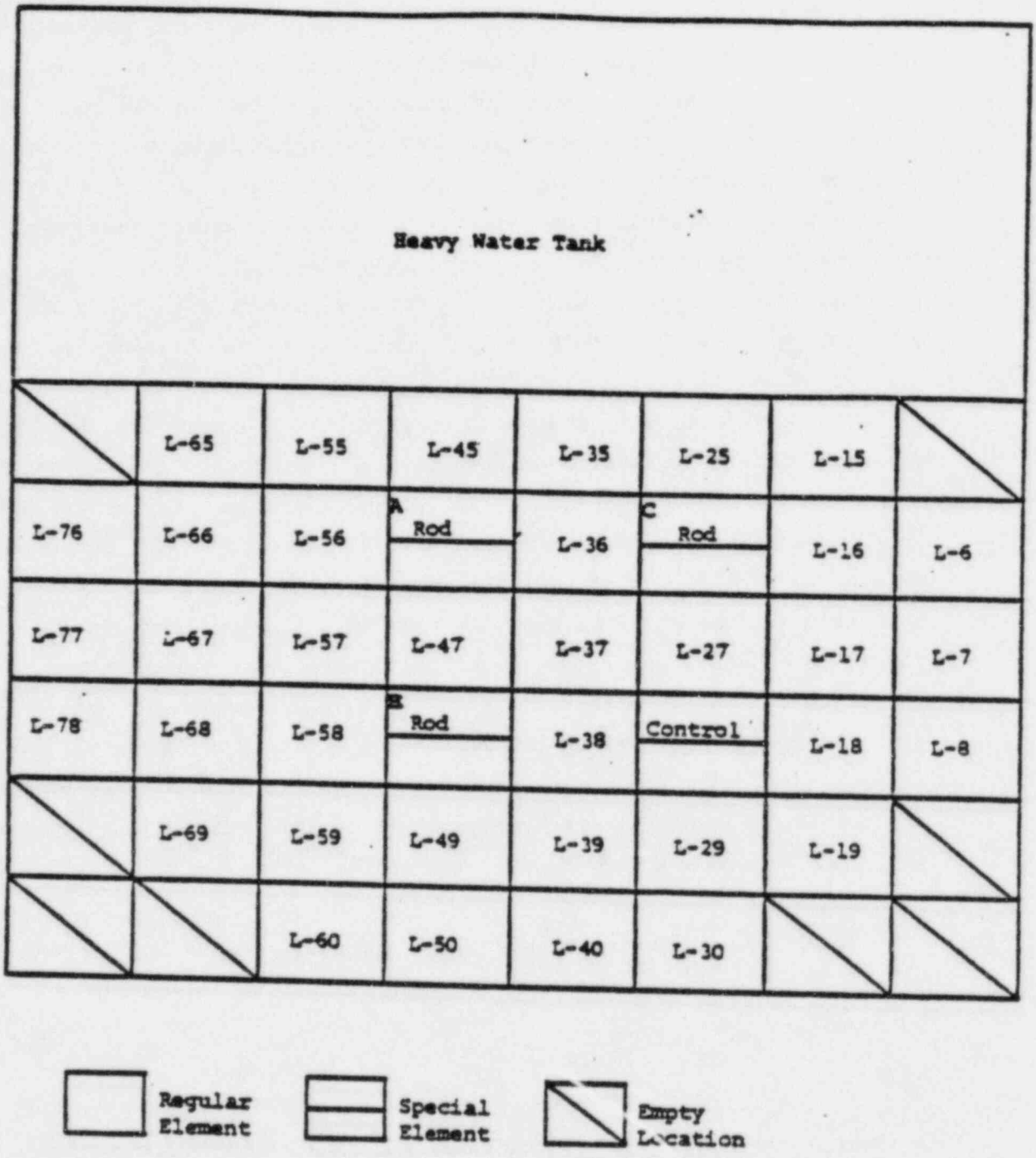

Figure 9. Key to Lattice Positions

Table 2. Epithermal Correction Factors

Lattice Location	Description	Correlation coefficients to straight line fits	$\frac{\text{Cadmium covered activity}}{\text{Bare activity}} = 1 - f_{th}$
D-O	D_2O tank penetration O	.9999, .9999	.0282
L-67	Regular fuel element	.9999, .9999	.1677
L-37	Regular fuel element	.9999, 1.0000	.2093
L-40	Regular fuel element adjacent to H_2O reflector	.9997, 1.0000	.1703
L-40-A	Channel 2 in H_2O reflector element	.9994, .9998	.0726
D-X	D_2O tank penetration X	.9998, 1.0000	.1052
L-39	Special fuel element (measured in waterhole)	.9999, .9999	.0874

$$\bar{\Phi}_{th}(\underline{x}) = \frac{I_{TOT}(\underline{x})}{S_{th}(\underline{x})}$$

The radial and axial measurements of $I_{TOT}(\underline{x})$ (and hence $\bar{\Phi}_{th}(\underline{x})$), are discussed next.

5. Rhodium Detector Flux Maps

a) Axial Profiles

Axial profiles have been measured in elements L-37, L-40, L-35, the H_2O reflector, and D_2O tank position S (See Figure 5). A typical axial rhodium detector flux map is shown in Figure 10 for L-37. The axial measurements have not yet been point-by-point corrected for variations in the detector's epithermal signal, which implies the thermal flux in the reflectors is too high by 10%. The values of $\bar{\Phi}_{th}$ in the active fuel region are approximately 8% higher than predicted by the iron wire data. This is directly attributable to the choice of sensitivity, as discussed previously.

A comparison of axial profiles in L-35, L-37, L-40 and channel 2 in the H_2O reflector is shown in Figure 11. The appropriate epithermal correction factor, $f_{th}(\underline{x})$, was applied to each element. By taking the ratios of measured points, it is seen that the axial profile remains constant for L-37 and L-40, but flattens close to the D_2O tank (L-35). Computer calculations also predict a constant axial profile throughout the core except near the D_2O tank. Channel #2 in the H_2O reflector shows a curvature comparable to that in L-35. These profiles provide valuable information on the axial buckling, as well as the axial correction factors needed later.

b) Radial Profiles

The rhodium detector was also used to provide radial flux profiles. Because of the long wait times associated with the use of the detector (discussed earlier), radial profiles were measured along only a few horizontal planes. In addition, reactor equipment (such as control rod drive motors, vertical beam tubes, etc) blocked the access to 14 of the fuel elements and several of the D_2O tank penetrations. Measurements in the H_2O reflector were made with the adapter always positioned south of L-40, so that a complete north-south traverse of the core could be plotted. Each of the two radial flux maps which were measured is discussed below.

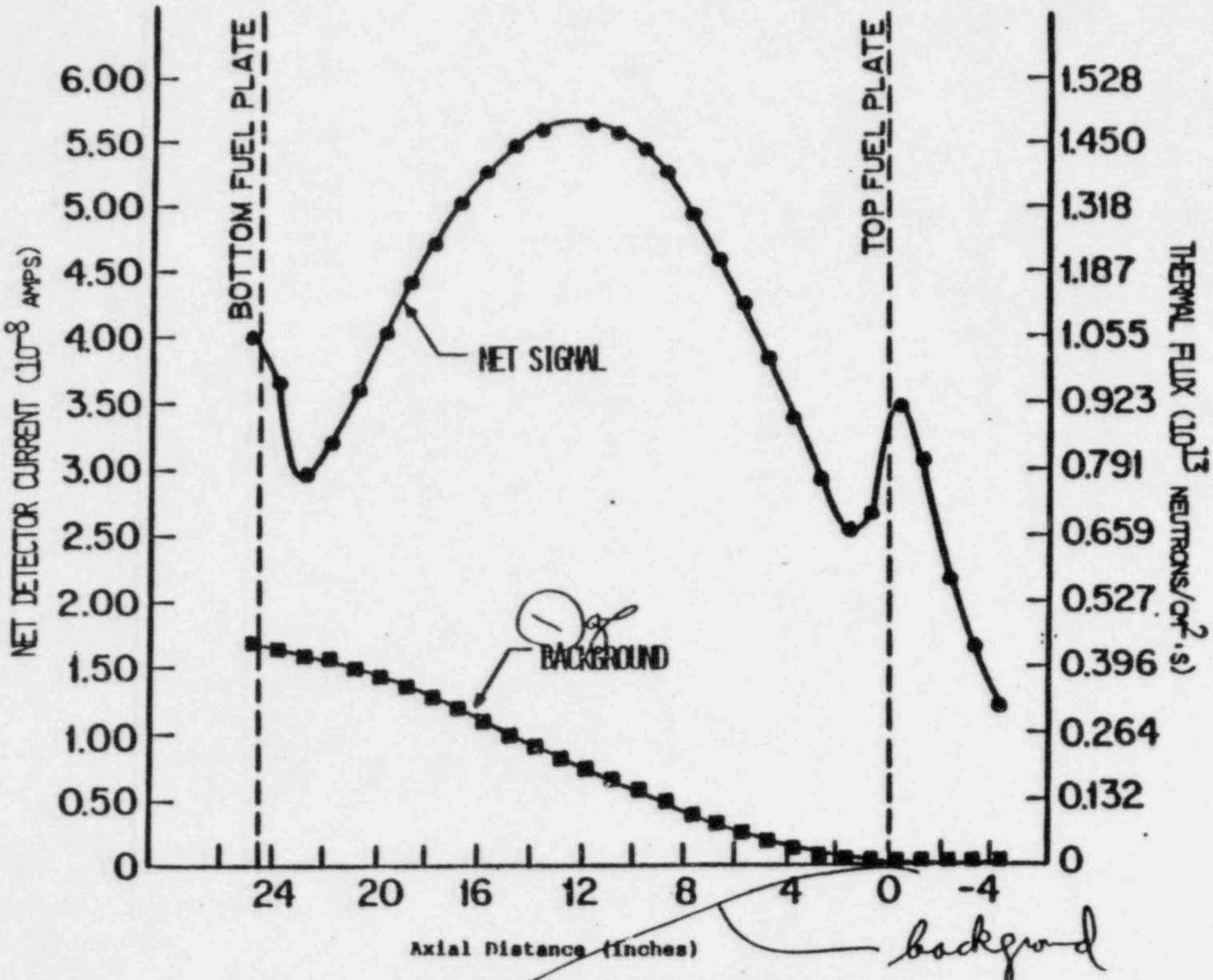

Figure 10. Axial Profile for Regular Fuel Element in Location L-37

background

D:O ⊕ bkd but small

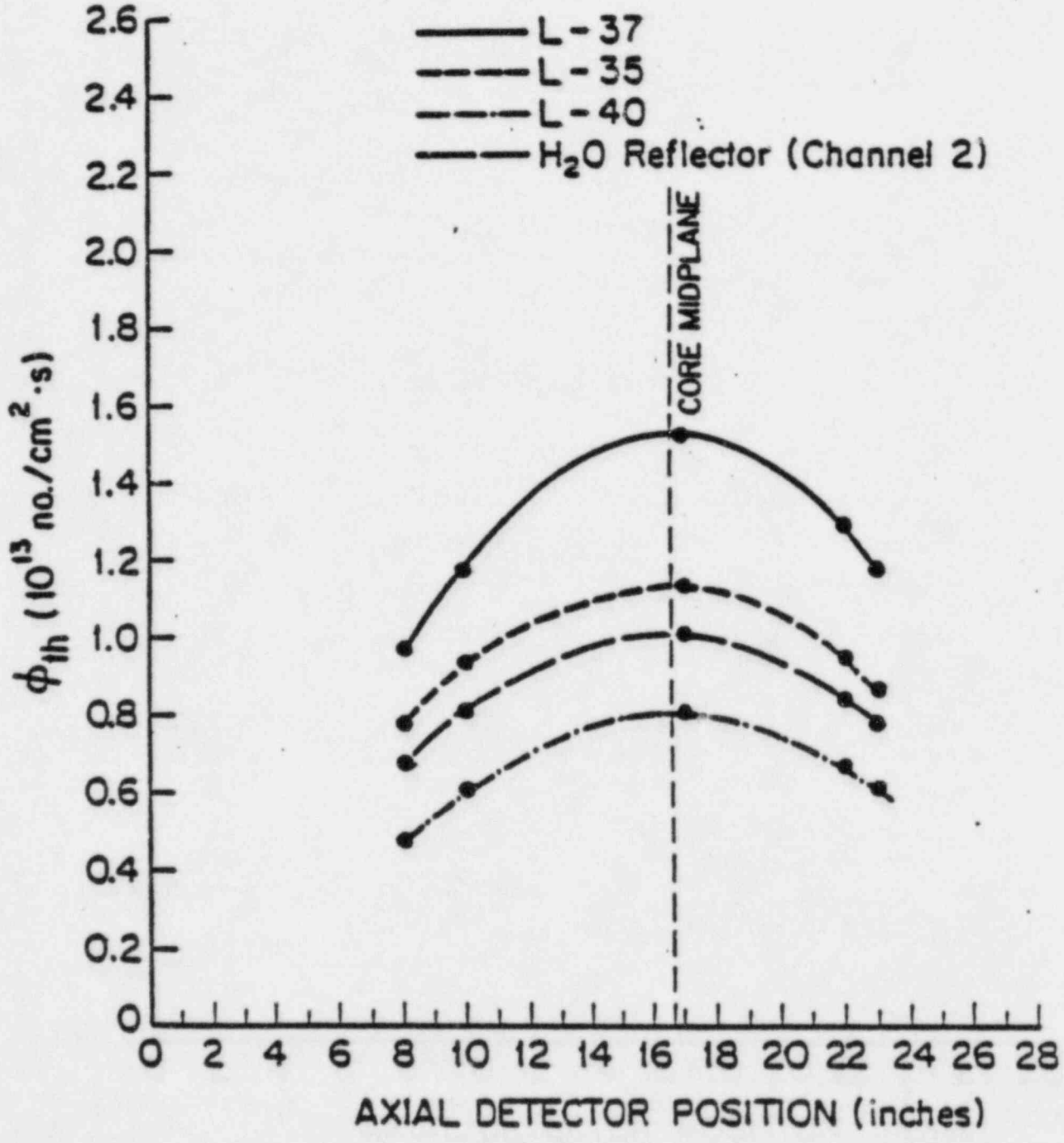

Figure 11. Axial profiles in H_2O, L-39, and L-40 Lattice Locations

The first radial flux map (denoted as map #1) measured the flux in all accessible fuel elements, the H_2O reflector, and two D_2O tank penetrations. The data was taken at three axial levels: 1/4 into the fuel, the core midplane, and 3/4 into the fuel element. North-south traverses through the core center (L-37) are plotted in Figure 12 for the 1/4, midplane, and 3/4 planes. The curves which are drawn between the data points are subject to interpretation, but are probably not far from the actual profile. Also shown on the plot is the core midplane data without the epithermal correction factor applied. Not only is the absolute value of the flux reduced by a sizeable amount, but the shape also changes due to the different values of $f_{th}(\underline{x})$.

For this map, core position L-39 contains a special fuel element*, which explains the large thermal peak measured in the waterhole. These measured values contain some additional uncertainty due to the inability to accurately position the detector radially. In the core, the 3/4-position fluxes remain higher than the 1/4-position fluxes. This is consistent with the iron wire data, and rhodium axial profiles discussed earlier. However, in the H_2O reflector, the opposite is true. This may be due to a large neutron absorber which was adjacent to the bottom of the H_2O adapter element. Regarding the points in the D_2O tank, it should be noted that neither position T nor position W is directly on a line containing the other elements for which the data is plotted. Position W is quite close to the line, but position T is about six inches west of the line. Hence the value for T is estimated (on the basis of the second radial map discussed later) to be about 9% low.

The second radial flux map, denoted as map #2, measured the flux in all accessible fuel elements, the H_2O reflector, and seven D_2O tank locations. The additional D_2O tank measurements (relative to the first map) were made possible by the removal of a vertical beam tube. The measurements were made at the core midplane, and at the 1/4- and 3/4-planes for a few selected elements along the north-south line through L-37. The D_2O tank measurements were made on the 1/4-plane, and extrapolated to the core midplane. For some of the regular fuel elements in the core, the detector would not fit in the channel normally used (just south of the fuel bail). Measurements were

*The special fuel element has several of the center fuel plates removed to allow room for shim or control rods. For this map, lattice positions L-39 and L-57 contain special fuel elements.

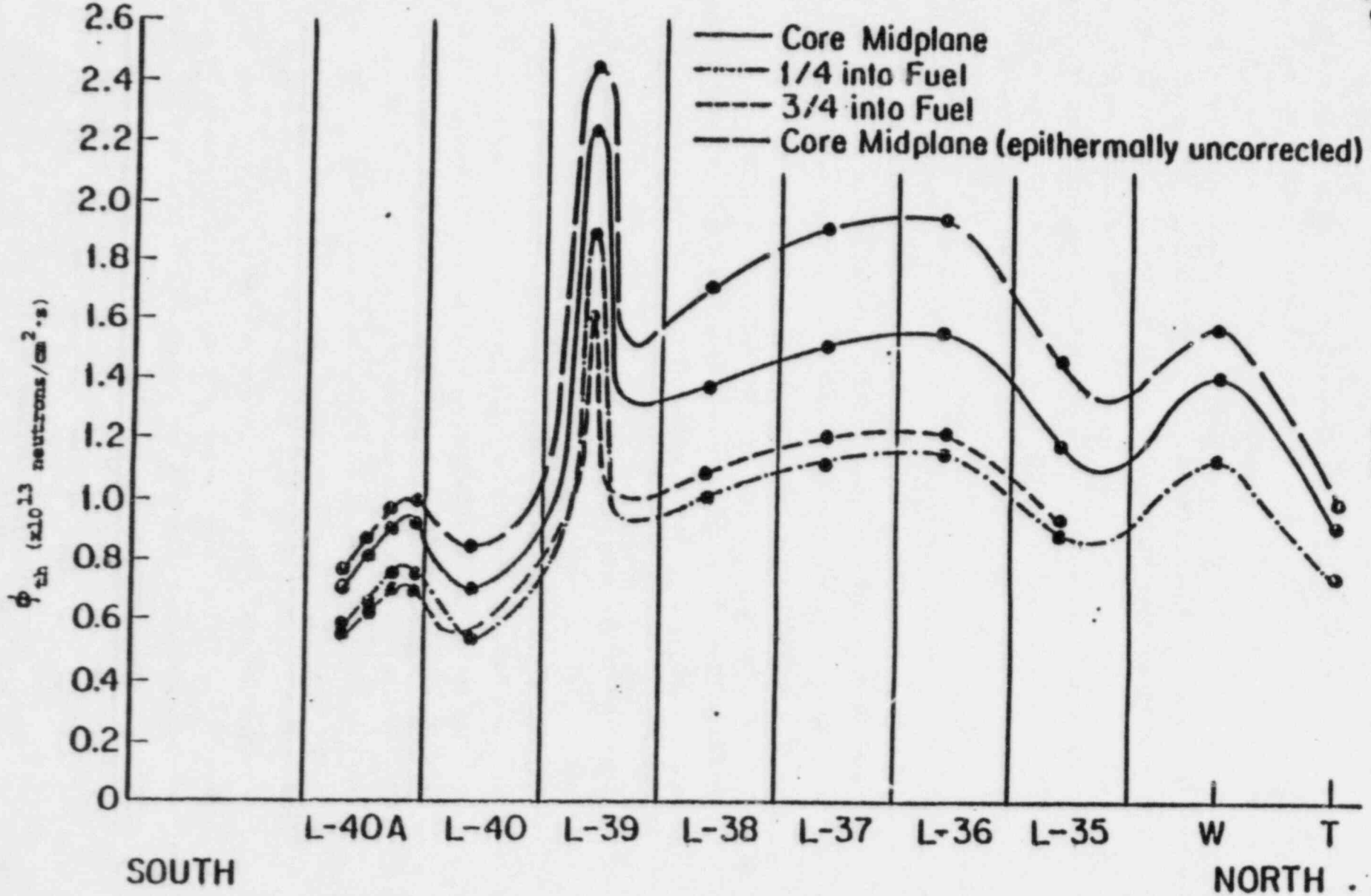

Figure 12. North-South Traverse Through L-37
Map #1

taken in a channel just north of the bail in these cases. The differences in the flux values between these two points is less than 2%, as shown by measurements taken on both sides of the bail in L-37. The core loading is slightly different than during the first map. A regular element replaced the special element that was in L-39, and the fuel element that was in L-50 was removed and not replaced. All other locations retained the same type of fuel element, although the individual fuel assemblies had been shuffled since the first map.

A north-south traverse through L-37 for the core midplane is shown in Figure 13. The thermal flux is seen to behave much more smoothly without the special element in L-39. The D_2O tank data is much more complete in this plot, and shows a flux peak which is comparable to that at the center of core.

The data which has been acquired provides valuable information on the thermal flux in the FNR core. The data is currently being used to benchmark the computer codes used by the analytical group to predict thermal fluxes. In addition, the data also provides information on the effects of the special fuel elements on the thermal flux distribution in the core and D_2O tank. It further suggests that the current shuffling pattern of regular fuel elements does not significantly alter the thermal flux shape. Lastly, the data will be used to determine the changes which are attributable to the introduction of low enriched fuel to the FNR.

6. Rhodium Detector Transfer Function Analysis

As described earlier, one of the major drawbacks associated with using a rhodium SPND is the several minute wait time required after a change in flux. This long wait time makes full-core flux maps impractical. Even the limited data presented in map #1 and map #2 involved substantial effort. An analytical technique which would eliminate the majority of the delay is being developed at The University of Michigan, and is briefly described in References 6 and 7. The analysis centers on developing the transfer function for the rhodium detector. If the transfer function is known, then the flux can be determined from the current without having to wait for the current to reach its equilibrium value. A full core flux map could be performed in a few hours, instead of a few days, should the technique prove sufficiently accurate.

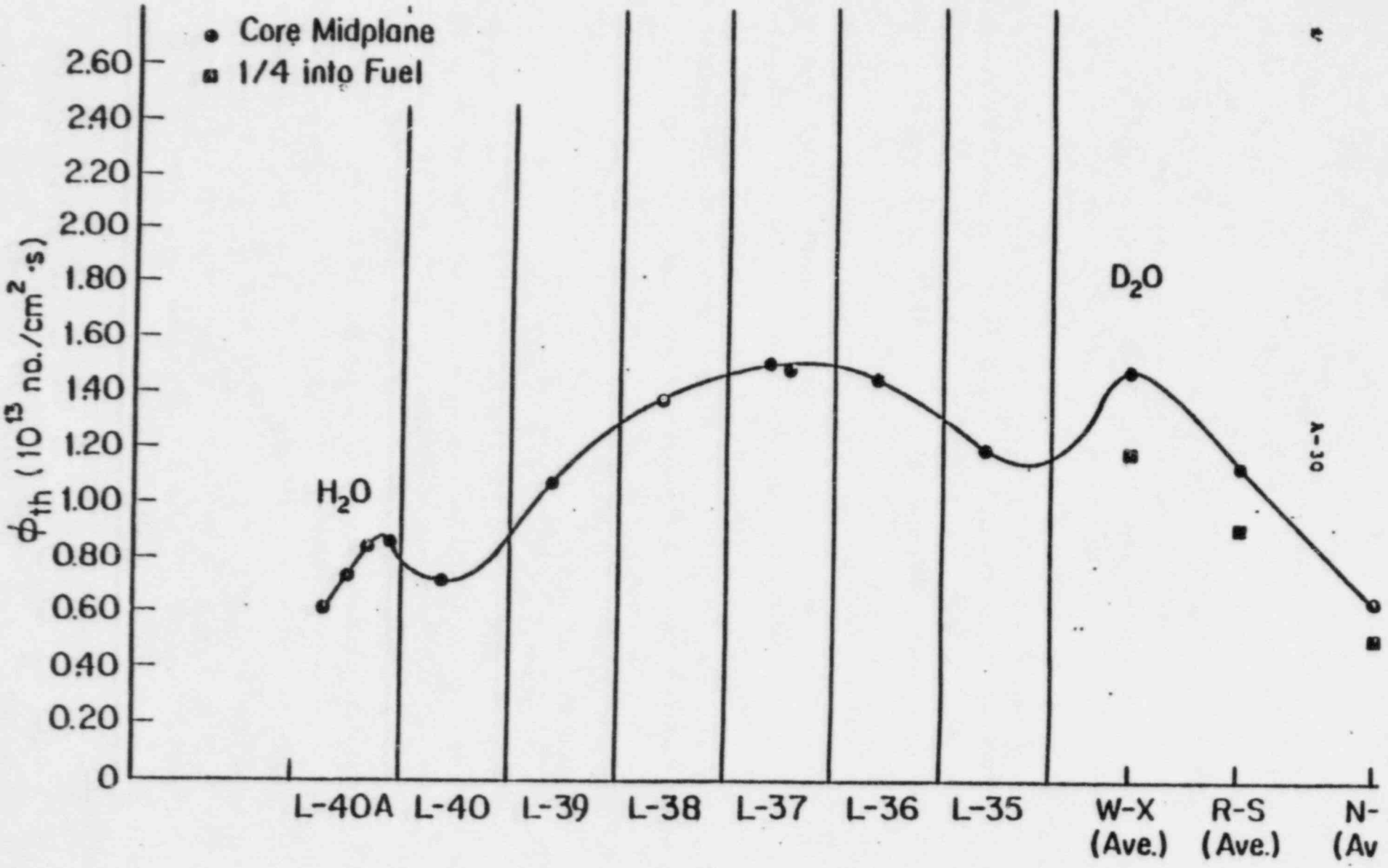

Figure 13. North-South Traverse Through L-37
Map #2

In order to develop the theory, first define (see Figure 6):

N_m = number density of Rh-104m states

N_g = number density of Rh-104 ground states

I = net detector current

σ_m, σ_g = cross sections for production of Rh-104m and Rh-104g states, respectively

N = number density of Rh-103

K_g, K_m = sensitivity of detector to ground and metastable decays

K_p = sensitivity of detector to conversion electrons from Rh-103*

γ = fraction of metastable decays going to ground

Then the kinetic equations can be written as:

$$\dot{N}_m = \sigma_m N \Phi - \lambda_m N_m \tag{1}$$

$$\dot{N}_g = \sigma_g N \Phi + \gamma \lambda_m N_m - \lambda_g N_g \tag{2}$$

$$I = K_m \lambda_m N_m + K_g \lambda_g N_g + K_p N (\sigma_g + \sigma_m) \Phi \tag{3}$$

Thus, given $N_m(0)$, $N_g(0)$, and $\Phi(t)$, one can calculate $I(t)$ from equations (1) - (3). Pictorially, the equations are in the form:

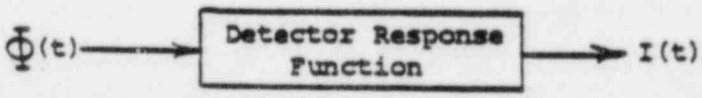

In practice, $I(t)$ is measured, and $\Phi(t)$ is the desired quantity. Thus, these equations are inverted by taking the Laplace transform, solving for $\tilde{\Phi}(s)$, and re-inverting to obtain $\Phi(t)$. The detailed and lengthy algebra is omitted, and the solution is presented below.

Define:

$$B \equiv (\lambda_g + \lambda_m) + \frac{\sigma_m K_m \lambda_m + \sigma_g K_g \lambda_g}{K_p (\sigma_m + \sigma_g)}$$

$$C \equiv \lambda_g \lambda_m \left[1 + \frac{(\sigma_g + \gamma \sigma_m) K_g + \sigma_m K_m}{K_p (\sigma_m + \sigma_g)} \right]$$

$$s_\pm \equiv \frac{-B \pm \sqrt{B^2 - 4C}}{2}$$

It can be shown that the inversion of equations (1)-(3) yields:

$$\Phi(t) = \frac{K_0}{2}\left\{ e^{\zeta_+ t} + e^{\zeta_- t} + \frac{e^{\zeta_+ t} - e^{\zeta_- t}}{\sqrt{1 - 4C/B^2}} \right\} +$$

$$+ \frac{1}{K_p(T_m + T_g)N(\zeta_+ - \zeta_-)} \int_0^t \left[e^{\zeta_+(t-u)} - e^{\zeta_-(t-u)} \right] \left[\dddot{I}(u) + \lambda_g \lambda_m \dot{I}(u) + \right. \quad (4)$$

$$\left. + \lambda_g \lambda_m I(u) \right] du$$

with $\Phi(0)$ determined by $I(0)$ from equations (1)-(3). Note that the integrals in (4):

$$\mathcal{I}^{\pm}(t) = \int_0^t e^{\zeta_\pm (t-u)} \left[\ddot{I}(u) + (\lambda_g + \lambda_m)\dot{I}(u) + \lambda_g \lambda_m I(u) \right] du \quad (5)$$

can be further reduced to:

$$\mathcal{I}^{\pm}(t) = \dot{I}(t) + C_1^{\pm}\left(I(t) - e^{\zeta_\pm t} I(0) \right) + C_2^{\pm} \int_0^t e^{\zeta_\pm (t-u)} I(u)\, du \quad (6)$$

with $$C_1^{\pm} = \zeta_\pm + \lambda_g + \lambda_m$$

and $$C_2^{\pm} = \zeta_\pm^2 + \zeta_\pm (\lambda_g + \lambda_m) + \lambda_g \lambda_m$$

Thus defining

$$F(t) = \frac{1}{2}\left\{ e^{\zeta_+ t} + e^{\zeta_- t} + \frac{e^{\zeta_+ t} - e^{\zeta_- t}}{\sqrt{1 - 4C/B^2}} \right\}$$

then equation (4) can be rewritten as

$$\bar{\Phi}(t) = \Phi(0) F(t) + c\left(\tfrac{1}{2}^{+}(t) - \tfrac{1}{2}^{-}(t)\right) \tag{7}$$

and the burden is apparently placed on evaluating the $\mathcal{I}^{\pm}$ terms. Either equation (5) or (6) can be used to determined $\mathcal{I}^{\pm}(t)$, and both approaches are equivalent.

In order to evalute $\mathcal{I}^{\pm}(t)$, we first consider the form of equation (5). We assume the data is taken at equal time intervals, that is:

$$t_i = (i-1)\,\Delta t$$

Further, we assume that the current I(t) can be approximated by a cubic polynominal during the time Δt between readings:

$$I(t) \approx Y(t) = \sum_{n=0}^{3} a_n(t_i)\,(u-t_i)^n$$

The $a_n(t_i)$ are determined by the cubic spline routine SMOOTH obtained from ANL. Then letting $x = u - t_i$, splitting the integral into a sum of integrals over time steps Δt, and after a little algebra yields:

$$\mathcal{I}^{\pm}(t) = e^{s_{\pm} t}\left(\sum_{i=1}^{+/\Delta t} e^{-s_{\pm} t_i} \left(\sum_{n=0}^{3} \alpha_n(t_i)\, J_n^{\pm} \right) \right) \tag{8}$$

where

$$J_n^{\pm} = \int_0^{\Delta t} e^{s_{\pm} x}\, x^n\, dx$$

and $\alpha_n(t_i)$ contains the $a_n(t_i)$ and constants from the derivatives.

Note that equation (8) is not a purely "on-line" scheme since it uses values of I(u) with $u > t$, to find $\bar{\Phi}(t)$. This turns out to be an advantage when only a limited amount of discrete data is available.

As mentioned above, equation (6) can also be used to evaluate $\mathcal{I}^{\pm}(t)$. In fact, note that when taking $\mathcal{I}^{+} - \mathcal{I}^{-}$ in equation (7) to find $\bar{\Phi}(t)$, the $\dot{I}(t)$ term drops out completely. Thus, one is only left with numerically evaluating:

$$\int_0^t e^{-S_2 u} I(u)\,du$$

Note that this scheme does have the promise of being "on-line" if one uses a numerical integration scheme such as the trapezoidal rule or Simpson's rule. We have found that the trapezoidal rule, Simpson's rule, and a smoothing scheme exactly analogous to that described above, give the same results for $\int_-^+(t)$.

Equation (8) is used for the evaluation of the $\int_-^+(t)$ integrals in the material which follows. The technique was first tested using a calculated current from equations (1)-(3), assuming a two-fold step change in the flux. The calculated current is shown in Figure 14, the response of the code to this input current is shown in figure 15. Both the remarkable ability (within 3 one-second time steps) to resolve the change, and the solution stability for long times are quite evident.

The code has also received extensive testing based on data taken on the FNR. The code response is compared to data which is taken using the conventional technique described in Section B.2. Figure 16 shows the results of a test where the detector is run smoothly through the center 21" of the core at a rate of 1"/minute. The vertical scale is exaggerated in order to show the characteristic lag of code response probably associated with values of $S_\pm$ slightly off. Nevertheless, calculations shows that the magnitude of the difference between equilibrium (solid line) and code response predictions (asterisks) averages only about 1%, within the experimental uncertainty of the data. A similar test using a 2"/minute motion through the core yielded differences which averaged only about 2%, and shows the characteristic lag to be slightly worse. Thus, using either 1"/min or 2"/min detector motions yields good agreement compared to the equilibrium data, with the possibility of superb agreement by slightly tuning S_+ and S_- to account for the uncertainty in K_p.

The response of the code was also tested in the reflector regions. The equilibrium data there is estimated to have an average uncertainty of 2% based upon its reproducibility. Figure 17 compares the code response to 1"/minute data taken every 30 seconds, to equilibrium data taken every inch. Similar results were obtained for the top reflector. Note that the largest difference occurred at the sharp reflector peak and was

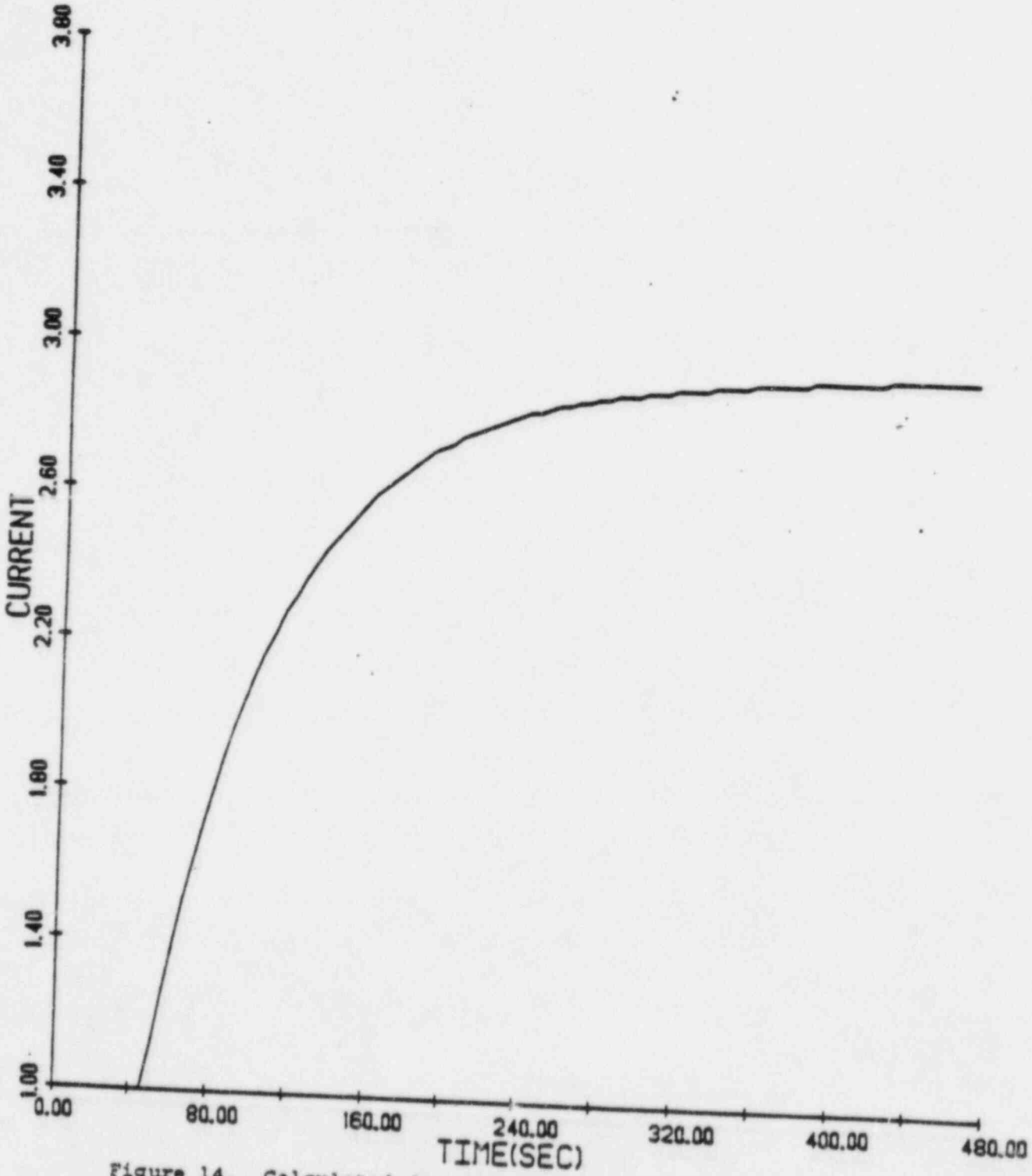

Figure 14. Calculated detector current following a three-fold step change in flux.

FLUX RESPONSE

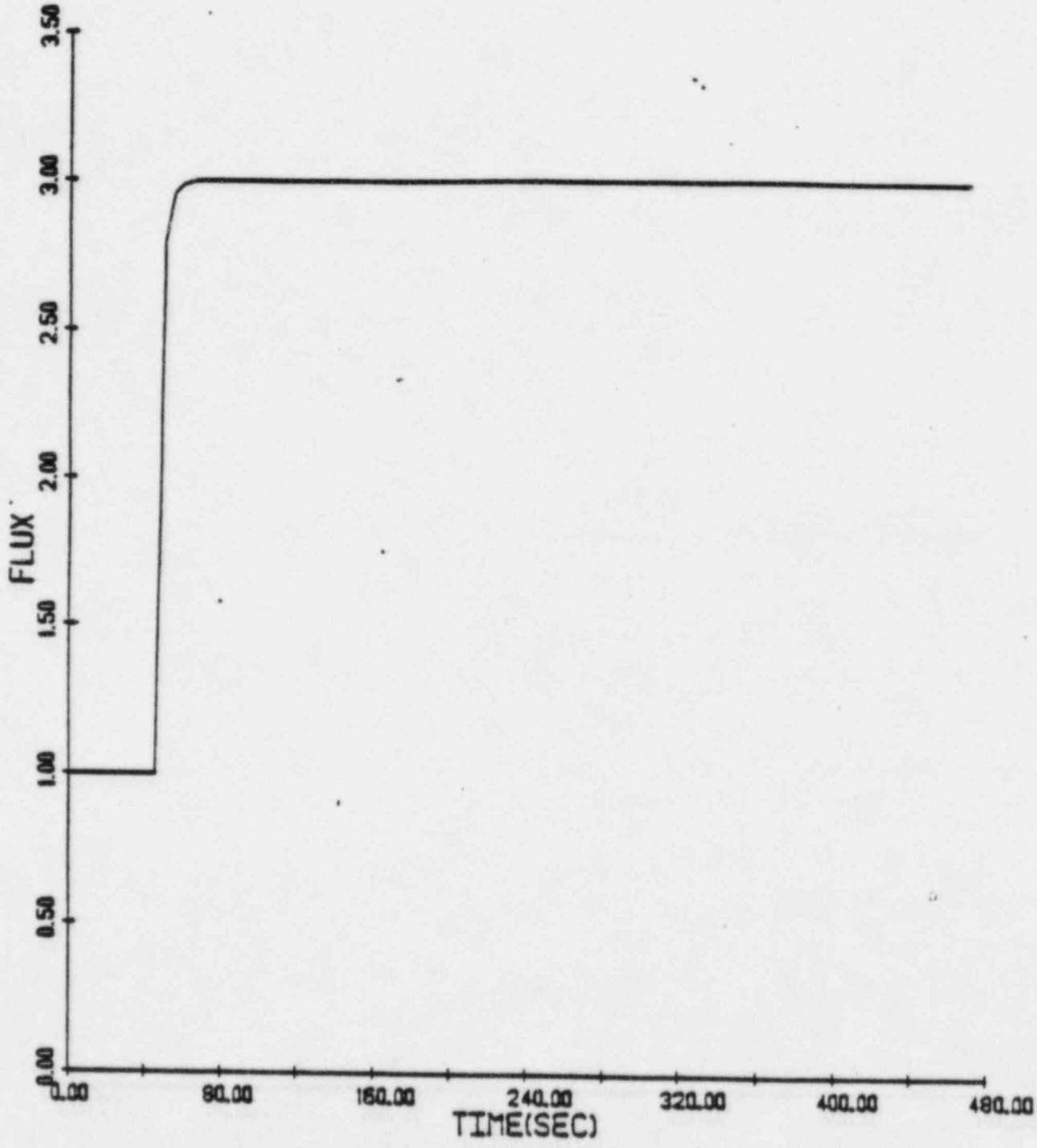

Figure 15. Code response to input data from Figure 14.

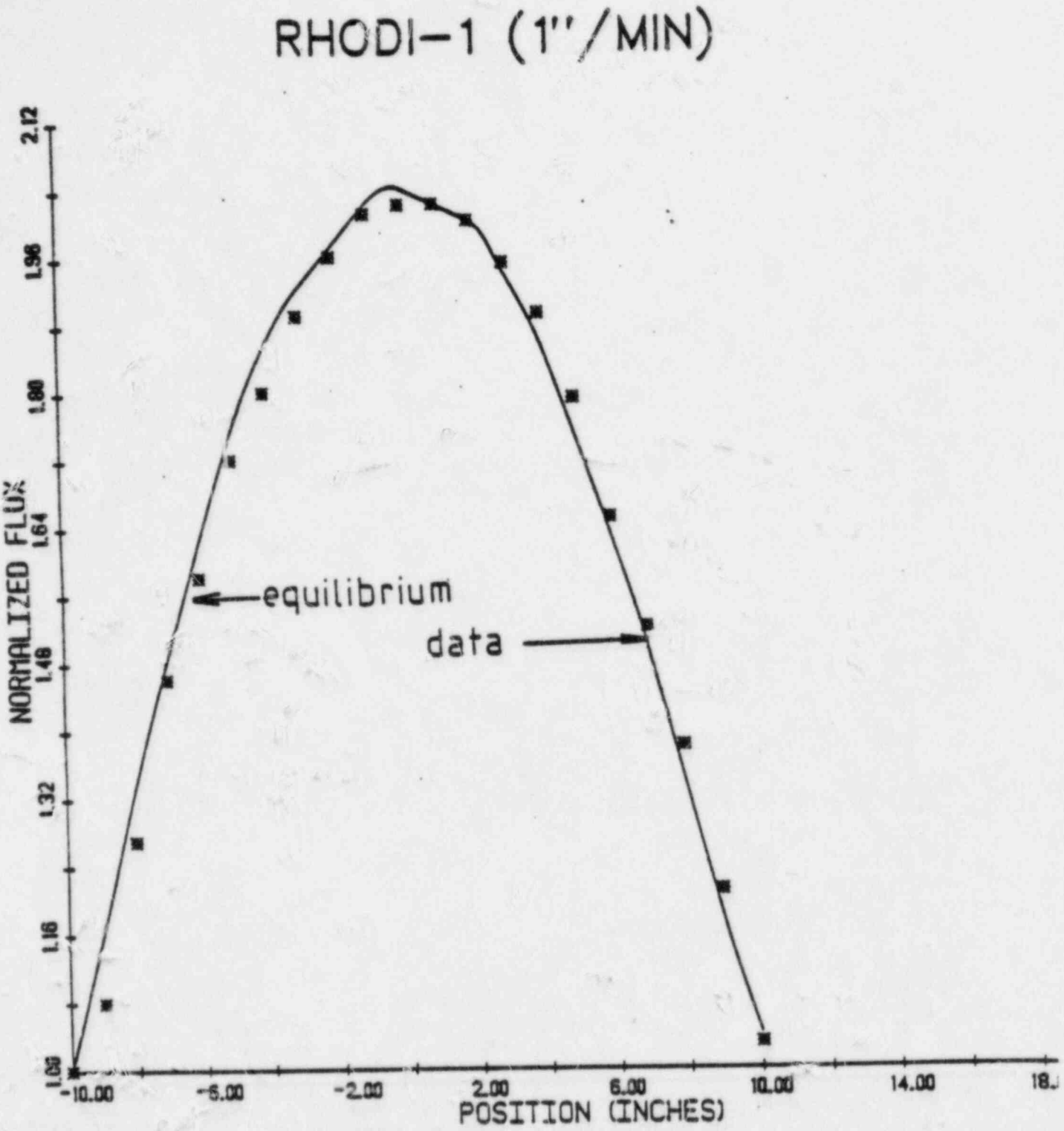

Figure 16. Equilibrium data compared to code response for data taken axially at 1"/minute through the center 21" of L-37.

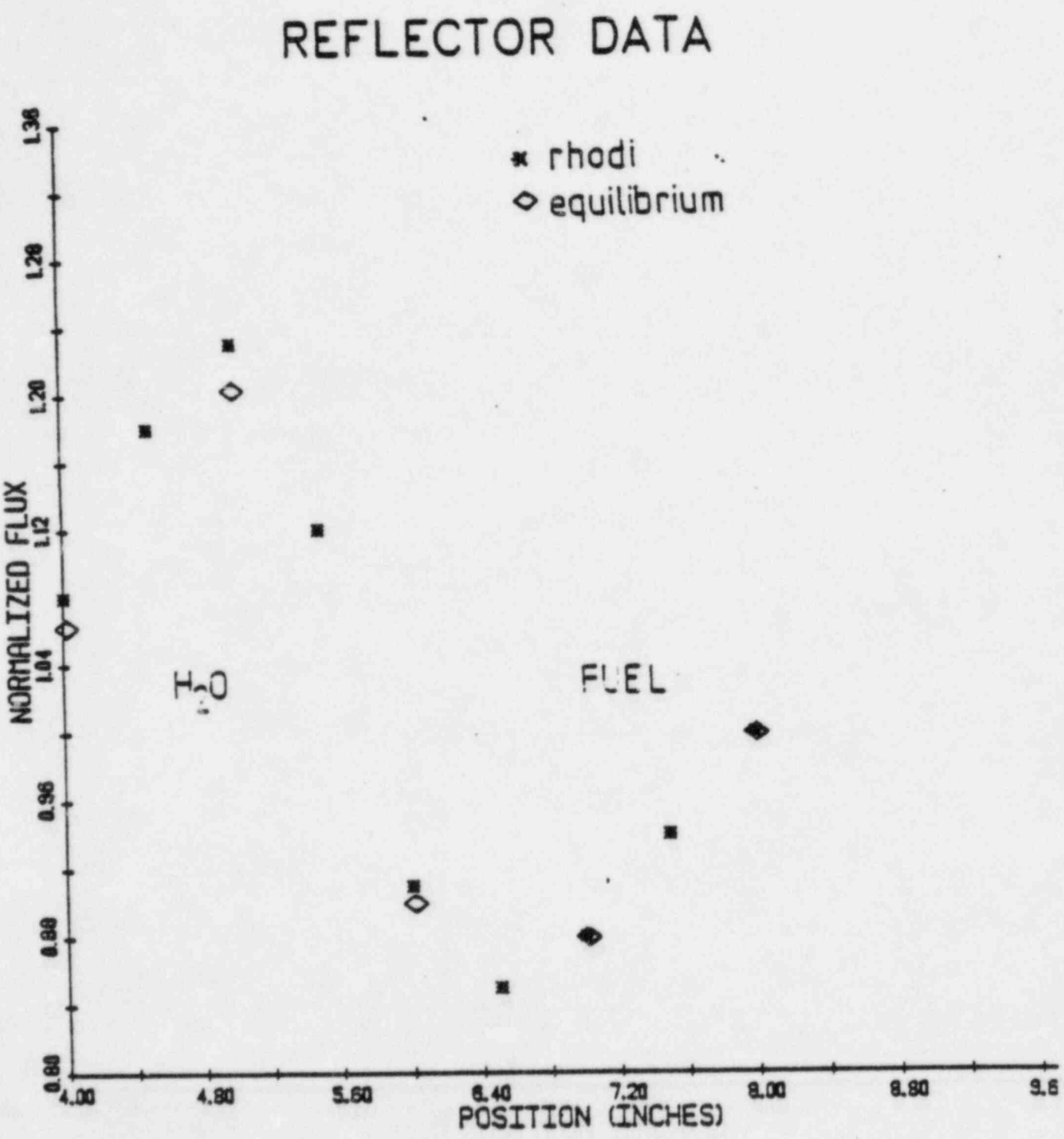

Figure 17. RHODI code response to data taken axially in H_2O reflector below L-37 is compared to equilibrium data.

6.7%, while the uncertainty of the equilibrium data there was 3%. When the experiment was repeated with a 1/2"/minute movement, the difference at the reflector peak was reduced to 2.5%.

Thus, the technique has been demonstrated to yield reasonable results with speeds of up to 2"/min through the core and 1"/min through the axial reflector regions. Even better agreement has recently been achieved by reducing K_p from 5% to 1%. In the core, the data which was low is increased by about 0.5%, and the data which was too high is decreased by a similar amount. In summary, as the code is "tuned" to the proper value of K_p, even greater speeds should be possible with negligible differences when compared to equilibrium data. This will allow full core maps to be made in a reasonable amount of time.

C. Thermocouple (ΔT) Measurements for Power Distributions

1. Purpose

The purpose of this phase of the experimental program is to provide a radial core map of the axially-integrated power distribution. This is used as a theoretical benchmark for the analytic group, as well as providing additional HEU-LEU comparisons. The data can also be used to obtain information about spectrally and spatially averaged fluxes, as well as being useful in the calculation of reactivity effects, such as power defects.

2. Equipment

A Cu-Constantan thermocouple is used for the ΔT measurments. The thermocouple sheath is enclosed in a stainless steel tube which can be extended into or retracted from the core by means of a plunger-type arrangement. The thermocouple leads are connected to a digital meter which reads temperature directly. Positive alignment is assured by a special mounting head which rests on the fuel bail.

3. Fuel Assembly Flow Rate Measurements

In order to convert ΔT measurements into power, the flow rates through each assembly must be known. Pressure drops across individual assemblies have been made and have shown:[8]

An FNR with 32 standard elements, 4 control elements with shim rods in place, and 2 open control elements (used as irradiation positions) has a measured core pressure drop of 2.1$\pm$.2 inches of water. This variation was observed by

making measurements in different core locations. The measurements in each element shows a fluctuation of not more than ±1/16 inch.

The tests performed on the fuel elements show that the pressure drop across the element varies as the square of the flow rate through the element. This is confirmed by similar flow tests performed on an element similar to the FNR standard element by AMF Atomics in 1959.[9] Further measurements made in a plexiglass test tank yielded fuel assembly flow rates as a function of pressure drop for unrodded special, rodded special, and regular fuel elements. These are summarized below for a 2.1" core pressure drop.

Element Type	Flow rates (gpm)
Rodded special element	18.0
Unrodded special element	29.0
Regular fuel element	20.5

Table 3. Measured flow rates

It should be noted that it is also possible to calculate the flow rates and core pressure drop if the total core flow rate is known. In practice, total core flow rate is continually monitored, and is known to a precision of about 1-2%. We have not yet had the opportunity to make these comparisons, however.

4. Thermocouple Maps

The results from one partial thermocouple map are shown in Table 4. The values which are presented are the ΔT in °F and the normalized assembly powers. Normalized core midplane thermal flux obtained from a rhodium map is presented also. The relative uncertainty in the ΔT readings is calculated to be 3.5% on the basis of repeated measurements.

Table 4. Results of Partial Thermocouple Map

Element	ΔT	Normalized Power	Normalized Φ_{th}
L-40	19.5±.4	.51	.48
L-39	28.5±.5	.74	.71
L-38	34.0±.3	.89	.91
L-37	38.4±.3	1.0	1.0
L-36	35.2±.3	.92	.97
L-35	27.1±.4	.71	.80
L-7	20.3±.6	.53	.63
L-17	26.0±.3	.68	.86
L-27	36.9±.6	.96	.97
L-47	41.0±.7	1.07	.99
L-67	20.9±.4	.54	.63
L-77	17.3±.3	.45	.46

While the thermal flux is measured on a slightly different core, comparison of the flux and power does seem to indicate that the thermocouple measurements need to be repeated and a careful analysis made to determine the sources of the differences above.

D. Neutron Flux Spectra by Activation Analysis

1. Purpose

The purpose of this phase of the demonstration experiments is to define the in-core spectrum. The technique chosen is known as "Spectral Analysis by Neutron Detection" or "SAND" and involves the unfolding of the neutron spectrum from activation measurements of many foils.

2. Background

The concept of unfolding neutron spectra is based on the fact that at saturation, the activity can be assumed proportional to:

$$\int_0^\infty \sigma_i(E)\,\Phi(E)\,dE$$

where $\sigma_i(E)$ is the cross section for the reaction being studied. If one assumes the cross sections are well known, then with many different activa-

tions, it may be possible to determine $\vec{\Phi}(E)$. This process of finding $\vec{\Phi}(E)$ given the saturated activities of several different foils represents the "unfolding".

The unfolding of neutron spectra has been a problem of serious interest for more than a decade, and yet the frequency of articles in the current literature underscores the importance of the techniques. Oster[10] has catalogued the various generic approaches used in unfolding, and listed over 20 unfolding computer programs using these methods. Zipf[11] has compared three of the more standard computer codes, including CRYSTAL BALL and SAND-II. In the past, we have used the SAND-II code[12] and SANDANL codes as our unfolding "workhorse". In addition to the SAND-II and SANDANL codes, the WINDOWS[17], FERRET[18], and STAY'SL[19] unfolding codes have been acquired. These codes are newer and use techniques which are more mathematically rigorous, such as linear programming for optimal solutions. The STAY'SL code also has the capability of using the ENDF covariance files mentioned above to assess the significance of the known errors in the cross sections on the unfolded spectrum. ENDF-V cross sections, written in a SAND-II compatible format, are available from Brookhaven National Lab and have replaced the original cross sections in our packages.

The selection of a set of foils plays a critical role in the accuracy of the unfolding process. For the unfolding process, one desires as many reactions as possible, as much energy coverage as possible, and as much overlap in energy coverage as possible. In addition, the irradiation-handling and counting processes impose additional constraints. For example, the foils cannot be packaged together, as is normally done, and still fit in the $\approx$1/8" slot between fuel plates. And uncertainties in the irradiation time make irradiations less than 10 minutes inadvisable. These and other considerations make the foil set selection procedure a difficult one.

To aid in the selection, the PRED code was written to predict the combinations of irradiation and wait times required to achieve the optimal count rate (including the energy dependance of the detector efficiency) on the fixed geometry, GeLi detector to be used. Varying foil thickness and diameters were considered, as well as the branching ratios for the various gammas to be counted, and isotopic abundances. The results yielded a set of six foil materials covering 17 reactions, and are summarized in Table 5.

Table 5. Selected Trial Foils

Foil	Reactions	E Region	Irradiation Time	Foil #
A. Copper	$Cu^{63}(n,\gamma)Cu^{64}$	.0072eV → 7.6keV	1/2 hr	1
	$Cu^{63}(n,\alpha)Co^{60m}$	5.9 → 11 MeV	1/2 hr	1
	$Cu^{63}(n,2n)Cu^{62}$	11.9 → 16.3MeV	1/2 hr	1
	$Cu^{63}(n,\gamma)Cu^{64}$(Cd)	.5eV → 9.6keV	1 hr	2
B. Aluminum	$Al^{27}(n,p)Mn^{27}$(Cd)	3.4 → 9.2MeV	1/2 hr	3
	$Al^{27}(n,\alpha)Na^{24}$(Cd)	6.4 → 11.8MeV		3
C. Iron	$Fe^{58}(n,\gamma)Fe^{59}$	.0076eV → .36keV	45 minutes	4
	$Fe^{56}(n,p)Mn^{56}$	5.4 → 10.9MeV		4
	$Fe^{54}(n,p)Mn^{54}$	2.3 → 7.7MeV		4
	$Fe^{58}(n,\gamma)Fe^{59}$(Cd)	.525eV → 2.3keV		5
	$Fe^{59}(n,\alpha)Cr^{51}$	----		-
D. Titanium	$Ti^{46}(n,p)Sc^{46}$	3.4 → 9 MeV	1 hr	6
	$Ti^{47}(n,p)Sc^{47}$	2.1 → 6.9MeV		6
	$Ti^{48}(n,p)Sc^{48}$	6.6 → 12.7MeV		6
E. Zinc	$Zn^{64}(n,p)Cu^{64}$	2.3 → 7.7 MeV	1 hr	7
F. Indium	$In^{115}(n,n')In^{115m}$	1.2 → 5.8 MeV	1 hr	8
	$In^{115}(n,\gamma)In^{116m}$	.040eV → 1.8eV		8

The results of the unfolding of data taken in L-37 using this trial foil set and the SANDANL code are shown in Figure 18. The indium foil yielded data which was suspect and was not included in the unfolding. The zinc foil was not available at the time of the irradiation, and a nickel foil was substituted. The figure shows the unfolded flux bounded above and below by one standard deviation. The lack of foil sensitivity in the 10 keV to 2 MeV is apparent from the magnitude of the uncertainty in the unfolded flux in this region. While the thermal flux energy mesh appears crude, it should be noted that the integral thermal flux agrees well with results presented earlier. Two lessons which were learned from this unfolding were:

1) Five foil materials are insufficient to determine the spectrum accurately over eleven decades of energy, and
2) introduction of cadmium covers into a regular fuel channel produces substantial perturbations in the flux.

As a result, additional foils have been added to the in-core irradiation plans. Also, an aluminum sample holder which fills the special fuel element center hole has been designed and built for more convenient incore irradiations. The unfolding of the incore spectrum has been demonstrated to be a more difficult problem than originally envisioned, and will represent a significant part of our future efforts.

E. Measurement of the Thermal Neutron Spectrum at Beam Port Exits

The shape and temperature of the Maxwellian-like thermal neutron spectrum is an important characteristic of the reactor, both in core and at the beam port exits. To determine if significant changes will be introduced by the low enrichment design, the experimental program has included measurements of the beam port exit spectrum using a crystal diffractometer. The initial results obtained are described below. These measurements will be repeated to refine the technique, and this will be repeated before and after the new core is installed.

1. Crystal Diffractometer Method

Data have been obtained on the FNR crystal diffractometer located at the exit of beam port I. Figure 19 is a drawing of the spectrometer and beam port geometry. The effective source plane is near the center of the D_2O reflector. Counting data is normally obtained using only the

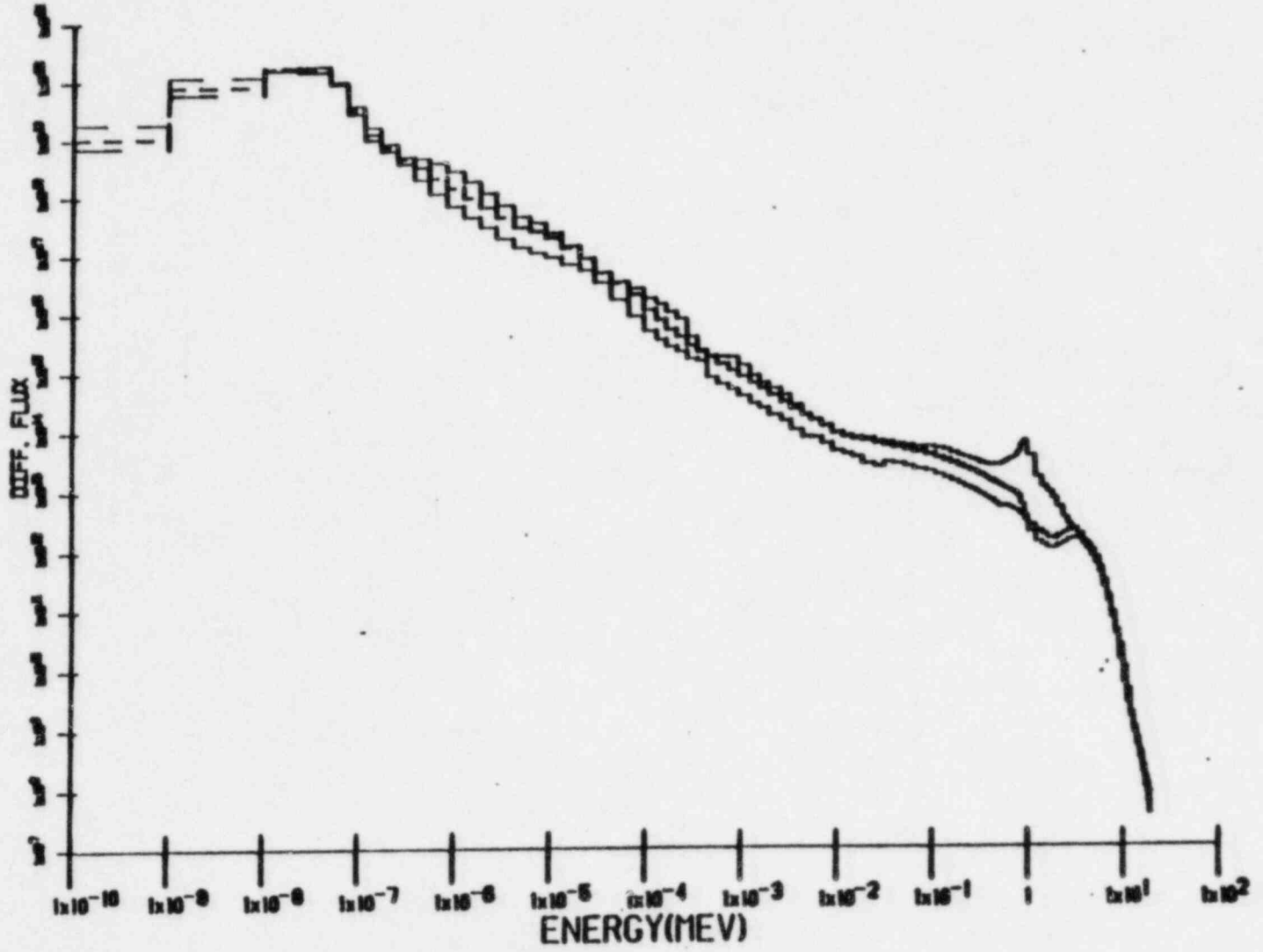

Figure 18. Unfolded in-core flux spectrum using five trial foils, along with upper and lower bounds on the solution.

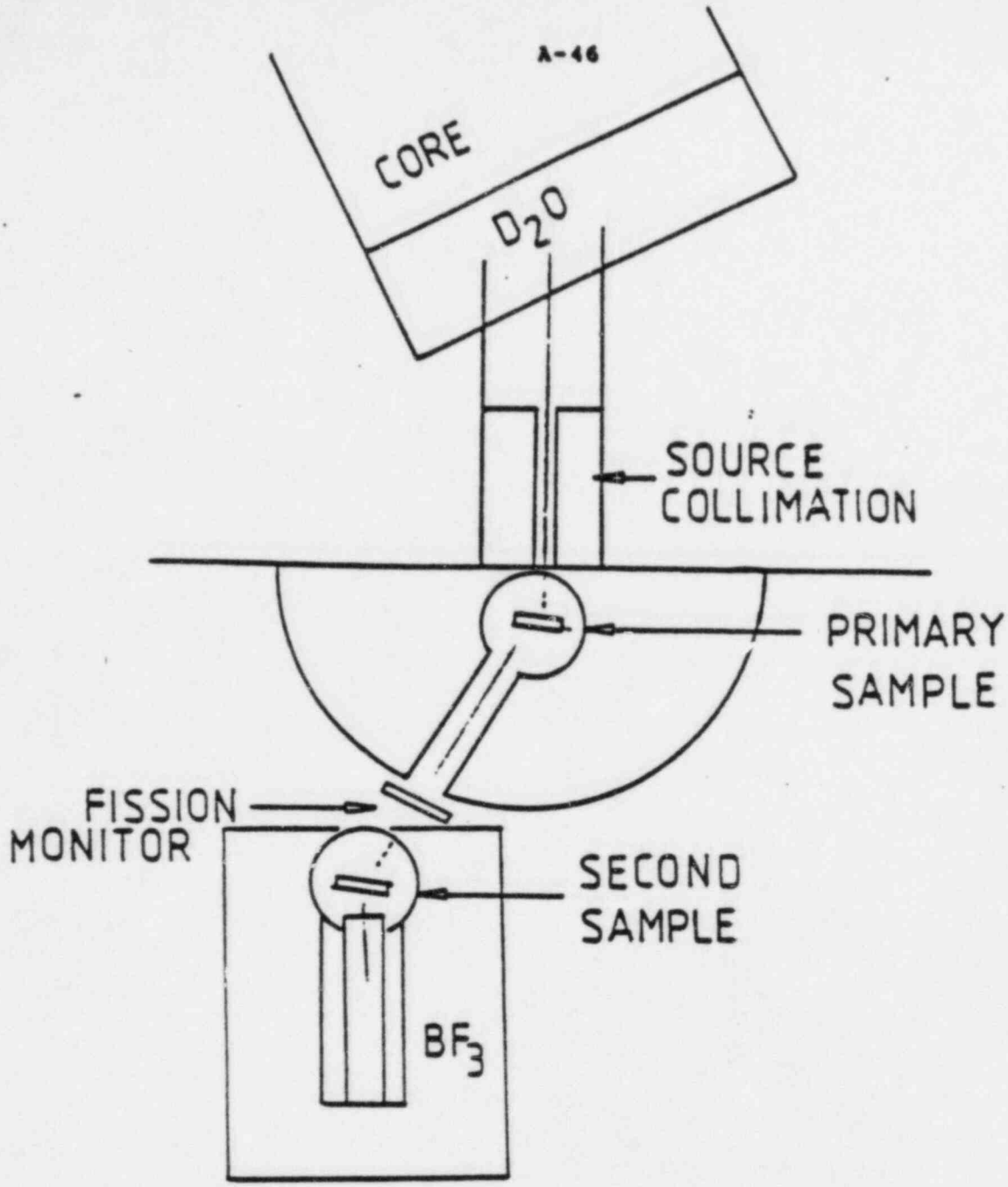

Figure 19. SPECTROMETERS

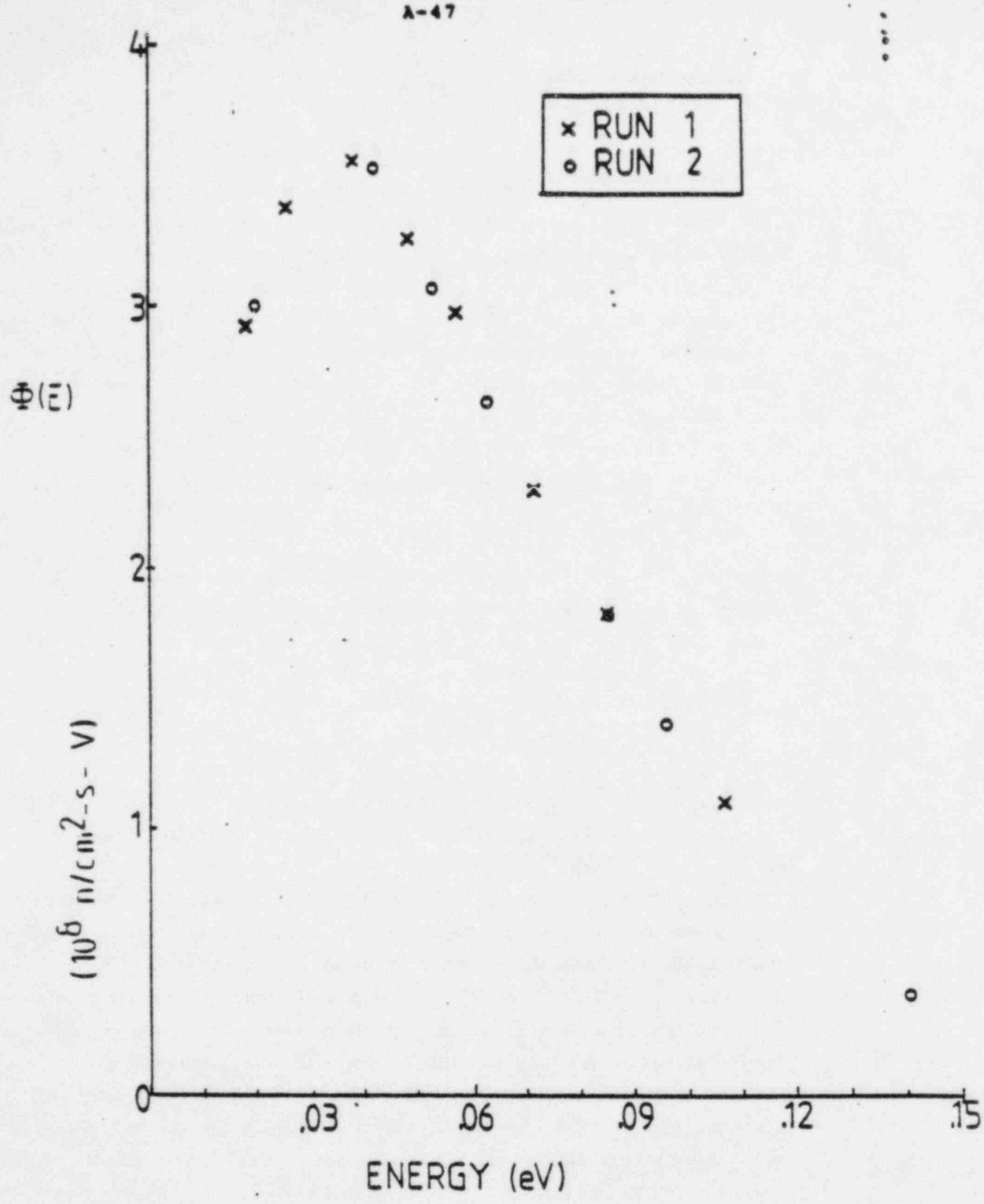

Figure 20. Thermal flux spectrum.

fission chamber monitor detector and a single crystal in the primary sample position, as shown in Figure 19. Counting rates are obtained as this monochromating crystal is rocked through Bragg angles about a given detector position $2\theta_o$, for a sequence of $2\theta_o$ positions. A silicon crystal of narrow mosaic, is used in (111) transmission reflection, which has the advantages of no second order reflective contamination, "constant" crystal geometric profile, and relatively reliable prediction of reflectivity versus θ_o. The count rate at each θ_o is, after background correction, given by

$$CR(\theta_o) = a \int_{-\infty}^{\infty} \epsilon(\theta)\, R(\theta-\theta_o)\, \bar{\Phi}(\theta)\, d\theta$$

where a is a constant geometry factor, $\epsilon(\theta)$ is the fission chamber efficiency versus θ (i.e., versus energy) and $R(\theta)$ is the crystal reflectivity. Because the latter term is sharply peaked in angle, the count rate is simply related to the flux by

$$CR(\theta_o) = a\,\epsilon(\theta_o)\,R(\theta_o)\,\bar{\Phi}(\theta_o)$$

The angular counting rate is converted to energy dependant flux $\bar{\Phi}(E)$ using the Bragg law. Figure 20 gives the results of points taken in two separate experiments.

It should be noted that the accuracy of the deduced $\bar{\Phi}(E)$ depends directly on the accuracy of the calculated reflectivity. We have followed the well-known kinematic diffraction theory for mosaic crystals in obtaining $R(\theta_o)$[13,14,15], but this requires a priori knowledge of the mosaic width of the crystal, η. While we have measured the mosaic width using a two-silicon crystal rocking experiment, the calculation of the reflectivity of a single perfect crystal is, in theory, much more straightforward. Thus, while it is only the shift in the neutron temperature that is required, it is our philosophy that if the data also produces an accurate absolute value of the neutron temperature, our confidence in the shift is reinforced. As such, we are in the process of repeating the measurements of the neutron temperature using a perfect silicon crystal.

Thus, in conclusion, the experimental program has progressed far in characterizing the HEU core. Additional measurements still need to be

made, particularly in the areas of in-core and excore spectra. But the program itself is sound and complete, and should quantify the significant differences which are associated with the enrichment change. These results should prove useful to other MTR reactors which are also considering upgrading their facility.

References

1. J. Duderstadt and L. Hamilton, Nuclear Reactor Analysis, John Wiley and Sons (1976).

2. K. H. Beckurts and K. Wirtz, Neutron Physics, Springer-Verlag (1964).

3. H. D. Warren, Nuc. Sci. Eng., 48, 331 (1972).

4. T. Laaksonen and J. Sasstamoinen, Proceedings of IAEA Specialists' Meeting on In-core Instrumentation and Failed Fuel Detection and Location, pp. 111-131, AECL-5124, Atomic Energy of Canada Limited (May 1974).

5. M. N. Baldwin and J. E. Rogers, Physics Verification Program, BAW-3647-23, Babcock and Wilcox Co. (December 1971).

6. J. M. Carpenter, R. F. Fleming, and H. Bozorgmanesh, Trans. Am. Nucl. Soc., 22, 606 (Nov. 1975).

7. D. K. Wehe and J. S. King, Trans. Am. Nucl. Soc., 35, 571, (Nov. 1980).

8. R. D. Martin, "A Low-Cost Shim-Safety Rod for Pool-Type Reactors", PML Internal report, (July 1967).

9. American Machine and Foundry Co., Engineering Report No. 7527, "Hydraulic Flow Test of an 18 Plate Dummy Fuel Element".

10. C. A. Oster, "Review of Unfolding Methods Used in the U.S. and Their Standardization for Dosimetry", BNWL-SA-6503, Battelle Pacific Northwest Laboratory (October 1977).

11. W. L. Zipj, Proceedings of the Second ASTM-EURATOM Symposium on Reactor Dosimetry, pp. 1333-1365, NUREG/CP-0004, National Technical Information Service (Oct. 1977).

12. W. N. McElroy, S. Berg, T. Crockett, and R. Hawkins, "A Computer-Automated Iterative Method for Neutron Flux Spectra Determination by Foil Activation", AFWL-TR-67-41, Atomics International (Sept. 1967).

13. W. H. Zachariasen, Theory of X-ray Diffraction in Crystals, Dover, N.Y. (1945

14. G. E. Bacon and R. D. Lowde, Acta. Crysta., 1, 303 (1948).

15. G. E. Bacon, Neutron Diffraction, Clarendon Press, London (1962).

APPENDIX B

Core Physics Analysis in Support of the FNR HEU-LEU Demonstration Experiment

Core Physics Analysis in Support of the FNR HEU-LEU Demonstration Experiment

by

David C. Losey, Forrest B. Brown, William R. Martin
and John C. Lee
Department of Nuclear Engineering
The University of Michigan
Ann Arbor, Michigan 48109

Abstract

A core neutronics analysis has been undertaken to assess the impact of low-enrichment fuel on the performance and utilization of the FNR. As part of this analytic effort a computer code system has been assembled which will be of general use in analyzing research reactors with MTR-type fuel. The code system has been extensively tested and verified in calculations for the present high enrichment core. The analysis presented here compares the high-and-low enrichment fuels in batch and equilibrium core configurations which model the actual FNR operating conditions. The two fuels are compared for cycle length, fuel burnup, and flux and power distributions, as well as for the reactivity effects which are important in assessing the impact of LEU fuel on reactor shutdown margin.

Presented at the International Meeting Meeting on Development, Fabrication and Application of Reduced-Enrichment Fuels for Research and Test Reactors, held on November 12-14, 1980 at Argonne National Laboratory.

1. INTRODUCTION

The University of Michigan Department of Nuclear Engineering and the Michigan-Memorial Phoenix Project are engaged in a cooperative effort with Argonne National Laboratory to test and analyze low enrichment fuel in the Ford Nuclear Reactor. The effort is one element of the Reduced Enrichment Research and Test Reactor (RERTR) Program, which is itself one facet of the overall U.S. policy seeking to minimize the risk of nuclear weapons proliferation. A near-term objective of the RERTR program is to demonstrate and implement enrichment reductions from 93% to less than 20% or, where that is impractical, to 45% within the next two years, based on currently qualified fuel fabrication technology. A part of the effort to meet this objective is a whole-core demonstration with reduced enrichment fuel, which will allow detailed testing and evaluation of the low enrichment fuel and an assessment of its impact on research and test reactor performance and utilization.

The Ford Nuclear Reactor (FNR) at The University of Michigan has been selected for the low-power whole-core demonstration. This demonstration project includes development of methods to analyze MTR-type fuel and core configurations, assisting in the design and analysis of the low enrichment uranium (LEU) fuel, preparation of fuel procurement specifications, preparing the requisite safety analysis report revision and license amendment application, procuring the operating license amendment, planning and conducting the experimental program, and analyzing the results of the experiments, including comparisons with analytical predictions.

The demonstration project at The University of Michigan has been divided into several phases. The initial phase, which is essentially complete, includes the work necessary to design and specify the fuel and obtain the necessary license amendments. The LEU fuel has been designed and is presently being frabricated by two European vendors, NUKEM and CERCA. The LEU fuel elements have a 167.3 gram fissile loading, which is 19.5% higher than the present high enrichment uranium (HEU) fuel. The initial phase of the demonstration project has also included an experimental program to characterize the current HEU core to provide a basis for comparison with the LEU core. In addition, experimental techniques and equipment are being tested and refined during this phase. A companion paper[1] presented at this conference provides further discussion of the experimental portions of this project. The major task of the project will be the actual whole-core testing of the LEU fuel along with the necessary measurements and analysis of experimental results and comparison with analytical predictions performed prior to core loading. The present project schedule calls for actual loading of LEU fuel elements in April, 1981. Further verification and improvement of our calculational methods will also be performed along with the whole-core testing program. Thus at the conclusion of the demonstration project, the impact of LEU fuel on the FNR performance and utilization will be assessed experimentally and compared with analytic predictions using methods developed and implemented during this investigation.

This paper presents a detailed review of the analytical effort performed at The University of Michigan as a part of the demonstration project. While many of our analytic results and methods have been summarized

in earlier conference and project reports[2-6], a detailed summary of the effort to date should be of use to the research reactor community. It is hoped that this review will provide guidance to others planning similar enrichment reductions and an appreciation of the practical considerations in performing detailed reactor analyses which cannot be addressed in generic studies. The following sections present a description of the calculational methods used in the physics analysis, and comparisons of the analysis and measurements used to validate the calculational model for the present high enrichment uranium fuel. We also present comparisons of the physics analyses for the HEU and LEU fuels, a summary of current efforts, and our conclusions to date.

The FNR currently uses highly enriched uranium MTR-type fuel. To provide the means for a valid prediction of the impact of LEU fuel on FNR operation, safety, and research usage, a generic neutronics model has been developed. This model is based on standard, well-verified production codes which are routinely used in reactor analyses. These codes have been modified only when necessary to accommodate the special characteristics of small low-power research reactors with plate-type fuel. As such, the methods of analysis should be applicable to a large number of research reactors and accessible to many computing installations. The following sections provide a brief description of the calculational model and its verification.

II. CALCULATIONAL METHODS

A. Computer Codes

All analyses were performed with the standard, well-verified production codes LEOPARD[7], EPRI-HAMMER[8], 2DB[9], ANISN[10], TWOTRAN[11], and VENTURE.[12]

Brief descriptions of code capabilities are:

1) LEOPARD - a zero-dimensional unit-cell code using the MUFT/SOFOCATE scheme (54 fast and 172 thermal groups); has depletion capability; cross-section library consists of an early industrial data set.

2) EPRI-HAMMER - a one-dimensional integral transport theory code using 54 fast and 30 thermal groups; cross-section library constructed from ENDF/B-IV data.

3) 2DB - a two-dimensional multi-group diffusion theory code with depletion capability.

4) ANISN - a one-dimensional discrete ordinates transport theory code.

5) TWOTRAN-II - a two-dimensional discrete ordinates transport theory code.

6) VENTURE - a three-dimensional multi-group diffusion theory code.

B. Code Modifications

The LEOPARD code originally performed a spectrum calculation for lattices consisting of cylindrical fuel rods. The code was modified to allow slab geometry and separate few-group edits for both lattice and non-lattice regions. The principal modification was in the calculation of thermal disadvantage factors by the ABH method for slab geometry.[13] A summary of these modifications is given in Table 1.

Table 1. Modifications to the LEOPARD Code

Modification	Purpose	Method
slab geometry option	analysis of plate-type fuel	- ABH method for thermal disadvantage factors for slabs - volume fractions, mean chord length, Dancoff factor redefined for slabs - minor input changes
lattice/non-lattice edits	allow separate few-group constants for lattice and inactive side plates	neutron conservation, with separate disadvantage factors for lattice region
xenon cross section edits	allows space-dependent xenon calculation in 2DB	transmit σ_a^{Xe} and Σ_a^{Xe} to 2DB
output few-group constant tablesets as functions of depletion	-automate data transfer to 2DB -allow interpolation in 2DB based on depletion	create output file compatible with modified 2DB
restart capability	allow parametric calculations at any depletion step	save all parameters needed to re-initialize code
added thermal expansion coefficient for Al	allow thermal expansion of meat and clad	minor addition to input routine
allow input multiplier for fission product buildup factor	burnup >> commercial reactor, correlation in code must be extended	minor input change
option for burnup dependent NLPF input	incorporate spectral effects of flux peaking variations due to burnup	minor input changes

The modified LEOPARD code compares satisfactorily with the EPRI-HAMMER code, an accurate, well-verified code used in the analysis of benchmark critical experiments. A typical comparison of k_∞ and two-group parameters in Table 2, shows that despite the many engineering approximations in the LEOPARD code, it compares quite well with the more accurate HAMMER code. Differences in few-group constants are due primarily to differences in the cross-section libraries - HAMMER uses ENDF/B-IV data while LEOPARD uses an early industrial data set.

The 2DB code has been modified to allow a macroscopic depletion capability via interpolation of macroscopic cross sections as a function of depletion. In addition, the isotopic balance equations for xenon and iodine have been included to allow the correct xenon levels within the core as a function of position and time (and macroscopic absorption cross sections are appropriately modified). Other modifications to 2DB have been aimed at automating data handling, improving fuel shuffling and edit capabilities, and greatly decreasing the computer run-time costs. These modifications are summarized in Table 3.

C. Basic Calculation Method

The LEOPARD and 2DB codes were used for routine calculations of core reactivity, depletion effects, and power and flux distributions. Special methods for control rods and core leakage flux are described in subsequent sections. For both HEU and the proposed LEU fuel, the following scheme was used:

Table 2. Comparison of LEOPARD and HAMMER Results for MTR-type Fuel

	93% Alloy		19.5% UAl_x	
	LEOPARD	HAMMER	LEOPARD	HAMMER
k_∞	1.5477	1.5500	1.5150	1.5116
ϕ_1/ϕ_2	2.41	2.40	2.76	2.75
Age	51.5	49.9	49.1	47.5
D_1	1.434	1.372	1.424	1.360
Σ_{a1}	0.00204	0.00182	0.00358	0.00344
Σ_{r1}	0.0258	0.0257	0.0254	0.0253
$\nu\Sigma_{f1}$	0.00206	0.00223	0.00256	0.00274
D_2	0.284	0.272	0.280	0.269
Σ_{a2}	0.0597	0.0594	0.0676	0.0668
$\nu\Sigma_{f2}$	0.0948	0.0935	0.110	0.108

Table 3. Modifications to 2DB

Modification	Purpose	Method
determine macroscopic cross-sections by interpolation based on local fuel burnup	model fuel number density changes and spectrum effects due to local fuel depletion	quadratic Lagrangian interpolation in cross-section tableset from LEOPARD at each depletion step major input options added, extra scratch file and memory
space-dependent xenon	xenon feedback	N^{Xe} determined from local power and flux levels σ_a^{Xe} interpolated as function of local fuel depletion Γ_a^{Xe} added to Xe-free Γ_a
dynamic memory allocation	reduced core storage requirements	system routines acquire only needed space
interface with LEOPARD	reduced input setup	A special preprocessor (LINX) converts LEOPARD cross section sets to the 2DB input format
FIDO input processor	free-format input with many options	total revision of input routines
recoding of inner iteration routines	reduce CPU time by factor of 4	use of precomputed constant arrays to eliminate redundant calculations
improved edits and output	detailed analysis of reaction rates, neutron balance	neutron conservation equations
complete recoding and updating of entire code	improve and clarify coding, reduced storage and CPU time, consolidate all changes	mnemonic variable names, structured programming, improved code logic.

11 The LEOPARD code was used to generate few-group cross sections. For most applications, two energy groups (fast and thermal) were used, although four energy groups were chosen for several detailed calculations.

The geometry chosen was a unit cell in slab geometry consisting of a lattice region and a non-lattice or extra region. The lattice region was composed of fuel meat, clad and water channel. For regular assemblies, the extra region consisted of the side plates, non-active portions of fuel plates, and inter-assembly water gaps, which are homogenized on a volume basis. For special fuel assemblies, the central water hole was also included in the extra region. Few-group macroscopic cross-section sets were generated as functions of depletion for the lattice and non-lattice regions and the total assembly.

For the water reflector and heavy water tank, the extra region was chosen as H_2O or D_2O with a .25% H_2O content and a volume fraction arbitrarily set equal to that of the lattice region. The extra region few-group cross sections obtained in this manner were used for the reflector and heavy water tank in the subsequent global calculation.

21 Global diffusion theory calculations were performed with the 2DB code. Three spatial mesh descriptions were used in x-y geometry. A homogeneous description, with a 2x2 mesh per assembly, was used for survey calculations, equilibrium core studies, and cycle length studies. A discrete representation, using a 6x6 mesh per

assembly with the lattice and non-lattice portions of an assembly explicitly represented, was used for detailed analysis of power and flux distributions, temperature coefficient, and control rod reactivity worth. A discrete representation with a 12x12 mesh per assembly was used for verifying the adequacy of the 2x2 and 6x6 representations, and for comparison with the measured flux distributions. The various mesh structures are presented in Figure 1.

Depletion was accounted for on the assembly level by interpolating macroscopic cross sections as a function of depletion (MWD/MTI for each assembly. The fuel shuffling capability in the 2DB code allowed actual FNR operation to be simulated. The axial BucRling term for the 2DB code used to approximate transverse leakage was based on a buckling and zonal buckling modifiers obtained from three-dimensional VENTURE calculations.

D. Control Rod Worth Calculations

FNR control (shim) rods are boron stainless steel containing 1.5 w/o natural boron. They are essentially black to thermal neutrons and cause a drastic thermal flux depression when inserted. The presence of such strong localized absorbers necessitates the use of transport theory codes to adequately describe the large flux gradients. However, in a small high leakage core like the FNR, control rod effects are not strictly local; therefore, whole core calculations are needed, but are prohibitively expensive for transport theory codes. To accurately treat both local and global

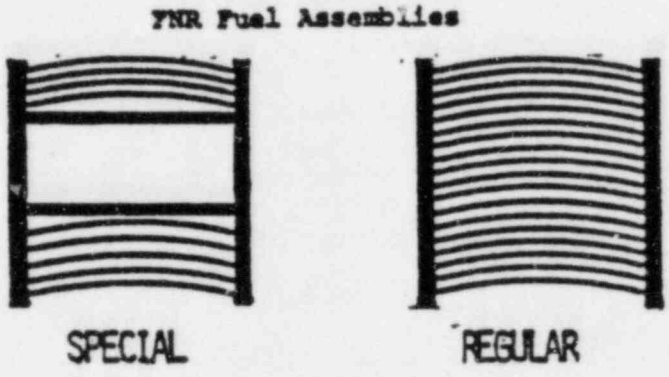

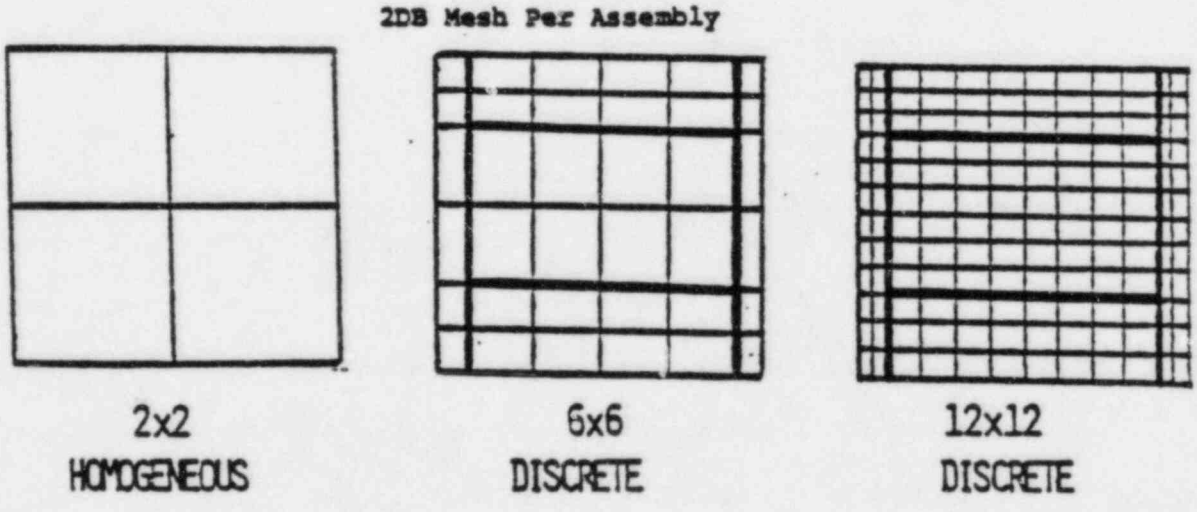

Figure 1. 2DB Mesh Description

effects, transport theory codes were used for assembly level calculations to develop effective diffusion theory constants for global calculations.

Few-group constants for the control rod and surrounding water were obtained from the EPRI-HAMMER code for a cylindricized special assembly. Due to the strong spectral/spatial coupling in the rod it was necessary to obtain few-group cross sections for three control rod regions - a surface layer .1 cm thick, a second layer .3 cm thick, and the central region. Since few thermal neutrons reach the central region, the control rod perimeter, rather than volume, was preserved in the geometric representation. Few-group constants for the special element lattice and side regions were obtained from the EPRI-HAMMER calculations for one half of a special element in slab geometry.

To accurately model the local effects of an inserted rod, the two-dimensional transport code TWOTRAN was used in fine-mesh calculations for a special assembly surrounded on all sides by one half of a regular assembly. Three regions of the rod and the surrounding water were explicitly represented, while the surrounding lattice regions were homogenized.

To develop effective few-group diffusion theory constants for use in global 2DB calculations, the 2DB code was used for the same geometry as in TWOTRAN calculations, except that the control rod and surrounding water were homogenized. Both fast and thermal absorption cross sections were varied until the 2DB calculation yielded the same relative absorption in the control region as the TWOTRAN result in each group. The resulting few-group constants for the control region were then used in global 2DB calculations. Although the flux distribution within the control region differed from the

transport theory results, we believe the relative absorption in the control region and the flux in the surrounding fuel is accurately predicted in this scheme.

Control rod worth was then determined by comparing global 2DB calculations for the 6x6 mesh/assembly description with and without control rod inserted.

E. Calculation Methods for Temperature Coefficient of Reactivity and Xenon Reactivity Worth

Calculations of the temperature coefficient of reactivity and of reactivity worth of xenon poisoning were performed with global 2DB calculations with a 6x6 mesh/assembly description. The two-group cross sections for these 2DB cases were obtained from unit-cell calculations with the LEOPARD or the EPRI-HAMMER code, essentially following the basic scheme outlined in Section II.C. To facilitate the calculation of the various coefficients, several modifications have been made to 2DB and LEOPARD. A microscopic xenon calculation has been added to 2DB which allows the calculation of spatially dependent xenon concentrations and corresponding adjustment of the local macroscopic cross sections in the 2DB calculation.

The calculation of the isothermal coefficient of reactivity does not require any additional modifications because cross sections are simply generated at a different temperature input to LEOPARD. However, the power defect of reactivity represents the total of all reactivity effects induced by taking the reactor from a cold zero-power condition to normal operating conditions. Due to the spatially nonuniform temperature and density changes

involved, the power defect cannot be predicted solely on the basis of an isothermal temperature coefficient. Therefore, additional changes were necessary. In particular a restart capability has been added to LEOPARD to allow the recalculation of the spectrum at any depletion step with one or more variables changed from the base depletion calculation. LEOPARD then calculates the resultant deviation $\Delta\Sigma$ in all cross sections divided by the variable change $\Delta\xi$ and outputs the "derivative" cross section $(\frac{d\Sigma}{d\xi})$ as a function of depletion. The 2DB code then calculates the local change in the variable, e.g., the change in the moderator temperature from the nominal temperature, and multiplies the interpolated derivative cross section by this change and adds the increment to the base macroscopic cross section, which is itself interpolated as a function of depletion and fuel type. Extensive changes to 2DB were not needed because existing mixing routines in 2DB were utilized. The $\frac{d\Sigma}{d\xi}$ cross section is treated as a microscopic cross section, which is multiplied by the "density" $\Delta\xi$ and added to the base macroscopic cross section Σ_o: $\Sigma = \Sigma_o + (\frac{d\Sigma}{d\xi})\Delta\xi$

III. VERIFICATION OF ANALYTICAL METHODS

A. Spectrum Calculations

The two cross section generation codes that have been utilized, LEOPARD and HAMMER, are well-verified codes and further effort to verify them was not warranted except for the application of LEOPARD to slab geometry. Since LEOPARD is a production code for pin cell geometry it was necessary to compare our modified version with a code capable of treating slab geometry. In particular we compared the slab version of LEOPARD with the HAMMER code for both LEU and HEU MTR-type fuel. Table 2. contains a comparison of the various

neutronics parameters and macroscopic cross sections for a unit cell calculation. In addition, the LEOPARD code has been verified against several critical assemblies, including the TRX rodded UO_2 and natural uranium slab lattices.[14] The agreement has been reasonable, and has further increased our confidence in the use of LEOPARD for routine calculations for MTR-type fuel configurations.

B. Global Calculations

To verify the accuracy of the analytic methods used in predicting core physics parameters for the HEU and LEU fuels the calculated results have been compared with experimental data from the Bulk Shielding Reactor (BSR)[15] and for various FNR core configurations. The comparisons for several FNR configurations summarized in Table 4. indicates the adequacy of the methods for calculating core criticality, power and thermal flux distributions, and control rod worth. Results of preliminary calculations simulating the power defect of reactivity data are also presented in this section.

The results presented in Table 4. indicate that core criticality is predicted accurately in our calculations. These calculations have revealed that considerable attention must be given to an accurate representation of the fuel geometry and of trace isotopes, such as U-236. Leakage in the axial direction in our two-dimensional (r-y) 2DB calculations was represented through the use of zone-dependant axial buckling obtained from three-dimensional VENTURE calculations. The resultant 2DB calculations are quite sensitive to the input buckling distribution and care must be taken when determining

Table 4. Experimental and Calculated Results for FNR Cores

Core Criticality

FNR Cycle	Mesh/Assembly	Measured	Calculated
146	6x6	1.000	1.003
183B	8x8	1.000	1.001

Assembly Power and Thermal Flux Distribution

FNR Cycle	Mesh/Assembly	Measurement	Locations Measured	RMS Deviation
67	6x6	Power	35	9.5%
152A	2x2	Thermal Flux	33	6.2%
157B	2x2	Thermal Flux	30	7.7%
159	2x2	Thermal Flux	34	7.1%
167A	2x2	Thermal Flux	33	4.5%
175D	2x2	Thermal Flux	22	7.2%
175D	8x8	Thermal Flux	22	7.4%
175D	12x12	Thermal Flux	22	8.0%
177B	2x2	Thermal Flux	22	5.5%

Total Control Rod Worth (% Δk/k)

FNR Cycle	Mesh/Assembly	Measured	Calculated	Deviation
17	6x6	6.57	6.41	-2.4%
67	6x6	6.24	6.30	+0.9%
91*	6x6	6.39	6.31	-1.1%
119	6x6	6.42	6.37	-0.7%
144	6x6	5.81	6.07	+4.5%
178	6x6	5.66	6.26	+10.4%

*New control rods installed

the transverse buckling for 2DB. The comparison of the calculated flux and power distributions with the FNR data given in Table 4 indicates reasonable agreement with RMS deviations in the range 4 - 10%. The comparison is based on the thermal flux data obtained with self-powered rhodium detectors at the core midplane and center of regular fuel elements. For Cycle 67, the power distribution was obtained from the measured temperature rise across each fuel assembly.

Control rod reactivity worth calculations were performed for six different FNR configurations. The method for obtaining the rod worths was discussed in Sec. II.D, except that the fuel depletion in the special fuel elements was also modeled. Accordingly, isotopic number densities for the lattice regions were taken from a LEOPARD depletion calculation for a special element at the corresponding burnup points. These number densities were then used in place of BOL number densities, and the sequence of HAMMER calculations described in Sec. II.D was repeated. Full-core 6x6 2DB calculations were then performed with all rods out and then separate runs were made with each of the three rods inserted. The calculated and measured rod worths are compared in Table 4.

The measured rod worths were determined from period measurements for rod positions in the upper half of the core. Considerable uncertainty exists in the measured worths due to the conversion from half rod to full rod worth and due to the use of an assumed effective delayed neutron fraction of .755%.[16] The calculated worths are in good agreement, although the increasing differences suggest that neglect of Boron depletion over many years of operation may be a source of error. Despite these uncertainties, the basic approach for computing control rod worth appears valid for comparing rod worths in HEU and LEU cores.

A preliminary calculation of the FNR power defect has been performed using the methods described above. However, the 2DB calculation, being a two dimensional calculation, cannot explicitly account for the effect of axial variations in fuel and moderator temperatures. Therefore, as a first attempt we have neglected axial variations and have represented radial temperature profiles by assuming an average temperature for each fuel assembly, which was determined on the basis of a 2DB calculation (to determine relative power factors) and measured FNR core temperature drops and flow rates. With this model, the power defect was calculated to be -.16% $\frac{\Delta k}{k}$, which may be compared with the experimental value of -.21% $\frac{\Delta k}{k}$. We are currently attempting to improve our model, by including a typical axial power distribution into the analysis by weighting the calculated temperature changes in an appropriate fashion.

IV DESCRIPTION OF BATCH AND EQUILIBRIUM CORE MODELS

To provide meaningful and comprehensive comparisions of HEU and proposed LEU fuels, it is necessary to model both the intrinsic fuel properties and the FNR operating conditions. For this purpose, two core configurations were analyzed for both fuels. The first configuration is a batch core consisting of fresh fuel assemblies, while the second configuration is an equilibrium core. The batch core configuration allows a comparison of undepleted HEU and LEU fuels, while the equilibrium core allows comparison of depletion characteristics and shutdown margin for conditions typical of FNR operation. The batch core model illustrated in Figure 2. has 31 fresh fuel assemblies, with four special assemblies at control rod locations. The configuration is symmetric about the north/south midplane and was analyzed using half-core calculations.

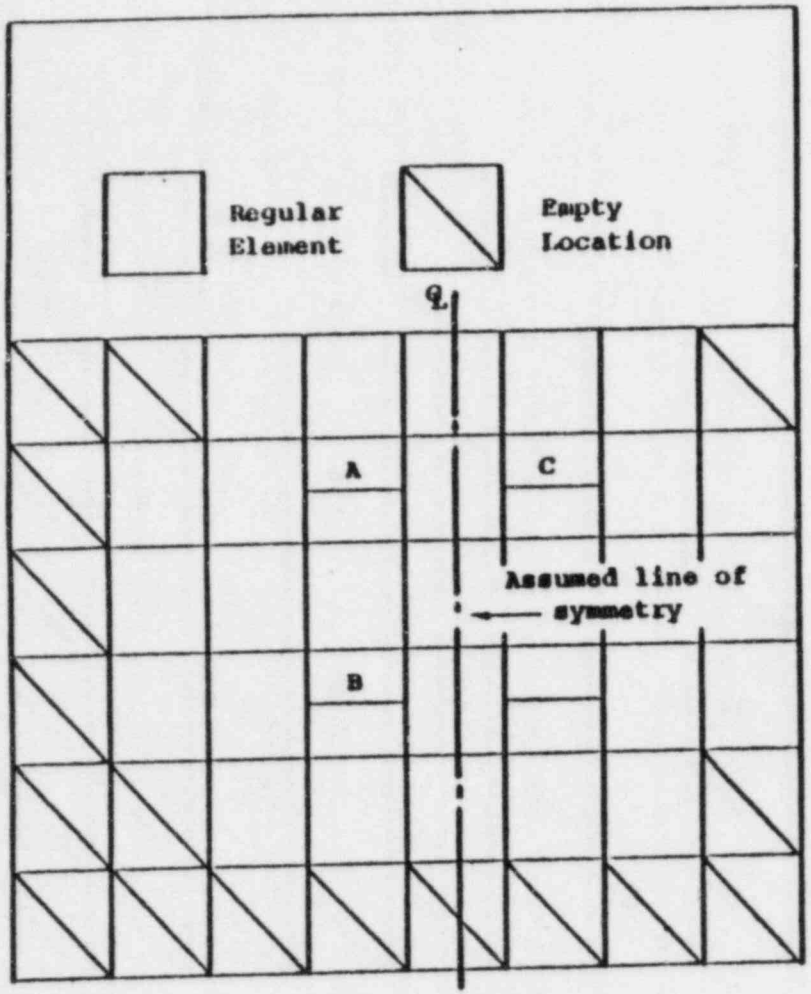

Figure 2. Batch Core Configuration

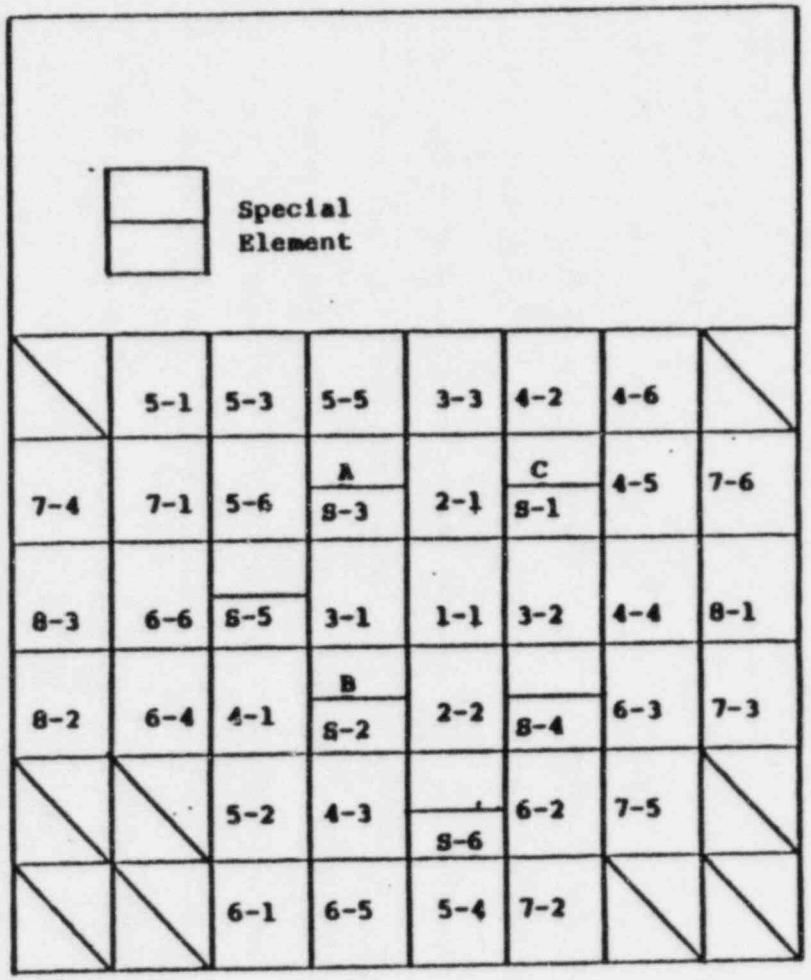

Figure 3. Equilibrium Core Loading Zones

Although the FNR core configuration and fuel shuffling pattern are, in practice, determined by operational requirements, an equilibrium core model was developed to allow a meaningful comparison of operating characteristics for the HEU and the proposed LEU cores. The equilibrium core shown in Figure 3, uses an in/out shuffling scheme with fresh elements loaded at the core center and moved outward to the core edge. This scheme maximizes the reactivity worth at the core center, thus maximizing the control rod worth to achieve the required 3% $\Delta k/k$ shutdown margin. To compare different fuel types in the equilibrium core, the end of cycle (EOC) k_{eff} was preserved between different cases. Preserving EOC k_{eff} provides the most realistic comparison of different fuel types, because it attempts to model actual FNR operation where a core is depleted until the shim rods are nearly fully withdrawn. Along with preserving the EOC k_{eff} the core size is also maintained constant. These two criteria essentially determine the maximum fuel burnup for a given fuel design. To achieve any higher burnup would require that the core size be increased in order to maintain criticality. Once the maximum fuel burnup is determined by preserving k_{eff} with a fixed core size, calculations must be performed to verify that the core configuration has the required 3.0% $\Delta k/k$ shutdown margin. Although the fuel burnup and power distribution are roughly constant during each equilibrium cycle, our equilibrium core configuration is chosen in such a way that the core configuration repeats every sixth cycle.

The shuffling pattern in the equilibrium cycles divides the 33 regular fuel element locations into eight loading zones as shown in Figure 3. Each regular element loading zone corresponds to core locations having

nearly equal fuel burnup, although not necessarily equal burnup rates. New fuel is loaded into Zone 1 and depleted fuel is discharged from Zone 8. At the start of each cycle, one new element is loaded into Zone 1, and the element in Zone 1 is moved to Zone 2. The fuel shuffling continues to Zone 8, where elements are discharged. The eight-zone shuffling pattern for the regular elements is shown in Figure 4.

The shuffling pattern for the special fuel elements is different because there are six special element locations. A new special element is added and a depleted element is discharged only every sixth cycle. With this shuffling pattern a new special element is placed in Special-Zone 1 at the start of cycle 1. The element removed from Special-Zone 1 is placed in ex-core storage for one cycle and then placed in Special-Zone 2 at the start of cycle 2. The sequence continues until the start of cycle 6 when the element from storage is placed into Special-Zone 6 and a depleted special element is discharged from the core. This shuffling pattern for special elements is shown also in Figure 4.

V. CHARACTERISTICS OF THE EQUILIBRIUM CORE MODEL AND FNR OPERATION

The equilibrium core model was designed to be typical of the actual FNR operation. Many characteristics of the FNR operation are well represented in the equilibrium core analysis. In fact, a modified version of the equilibrium core shuffling scheme has been implemented at the FNR and has proven to be a practical and efficient scheme for loading fuel elements. Nonetheless there are differences between the equilibrium core model and actual FNR operation. These differences exist mainly because FNR operation is more flexible than the equilibrium model. Fuel

Figure 4. Equilibrium Core Shuffling Scheme

Regular Fuel Elements

Cycle		Core Loading Zone							
		1	2	3	4	5	6	7	8
	New Fuel								
1	→	1-1	→ 2-1	→ 3-1	→ 4-1	→ 5-1	→ 6-1	→ 7-1	→ 8-1 →
2	→	1-1	→ 2-2	→ 3-2	→ 4-2	→ 5-2	→ 6-2	→ 7-2	→ 8-2 →
3	→	1-1	→ 2-1	→ 3-3	→ 4-3	→ 5-3	→ 6-3	→ 7-3	→ 8-3 →
4	→	1-1	→ 2-2	→ 3-1	→ 4-4	→ 5-4	→ 6-4	→ 7-4	→ 8-1 →
5	→	1-1	→ 2-1	→ 3-2	→ 4-5	→ 5-5	→ 6-5	→ 7-5	→ 8-2 →
6	→	1-1	→ 2-2	→ 3-3	→ 4-6	→ 5-6	→ 6-6	→ 7-6	→ 8-3 →

Discharge

Special Fuel Elements

Cycle	Storage		Core Loading Zone		Storage
1	New fuel	→	S-1	→	X_1
2	X_1	→	S-2	→	X_2
3	X_2	→	S-3	→	X_3
4	X_3	→	S-4	→	X_4
5	X_4	→	S-5	→	X_5
6	X_5	→	S-6	→	Discharge

elements need not be shuffled in any fixed pattern and the core configuration does not repeat periodically. This section describes characteristics of the equilibrium model and actual FNR core configurations, and also explains important differences between the equilibrium analysis and actual operation.

To verify the practicability of the equilibrium model, Table 5. presents a comparison of the calculated equilibrium core parameters and actual core parameters based on FNR operation.. The comparisons indicate that the proposed equilibrium cycle represents a reasonably practical configuration for comparing the HEU and LEU fuel designs. On the average fuel elements are shuffled just as often in both cores. The calculated control rod worths for the equilibrium core compare well with the rod worths measured in the FNR.

The cycle length comparisons for the equilibrium and operating cores in Table 5. point out a difference between analytic models and actual operations. In the equilibrium core model, cycle length is determined by the discharge fuel burnup averaged over the regular and special fuel elements. In contrast, the FNR operating cycle length is the time interval between shim rod calibrations, which are required by technical specifications whenever more than three fuel elements are shuffled. In calculations comparing the HEU and LEU fuels the parameter most indicative of the time between control rod calibrations or operating cycle length is the burnup reactivity change rate, rather than the equilibrium core cycle length. With a constraint on the allowable core excess reactivity, the length of time the core can be maintained critical without shuffling more than three fuel elements, thereby requiring rod recalibration, is determined

Table 5. Comparison of Equilibrium Core and Actual FNR Parameters.

	Operating Experience*	HEU Equilibrium
Operating cycle length (days)	17.6	—
Equilibrium cycle length (days)	—	11.0
Average number of element shuffles/day	.82	.80
Average discharge burnup (MWD/element)		
Regular	19.4	19.2
Special	19.5	16.9
Calculated k_{eff}		
Range	1.022-1.026	1.020-1.032
Average	1.024	1.025
Shim rod worth (%Δk/k)		
Rod A	2.20	2.08
Rod B	2.21	2.24
Rod C	2.00	2.17
Total	6.41	6.49

*Averaged from Oct. 78 to Nov. 79

by the fuel burnup reactivity change rate.

VI. CORE NEUTRONIC ANALYSES FOR THE HEU AND LEU FUELED CORES

The important neutronics parameters analyzed for the HEU and LEU fueled cores are the temperature coefficients of reactivity, xenon reactivity, control rod worth, discharge burnup, and the shutdown margin. Comparisons of these neutronic parameters for the batch core and equilibrium core configurations should provide a basis for assessing the impact of LEU fuel on FNR performance and utilization. Before discussing the results of these comparisons, the actual HEU and LEU fuel configurations will be discussed.

A. LEU and HEU Fuel Description

The selection of the LEU fuel design was based on extensive generic studies and survey calculations carried out by Argonne National Laboratory[17-19], The University of Michigan, and others. In addition, constraints were imposed on the final design as a result of the specific FNR system configuration, FNR operational considerations, and the need to obtain approval from the NRC of an amendment to the current FNR operating license. These constraints, which are unique to the FNR, had to be factored into the final LEU design.

Based on the above considerations, the LEU fuel design selected for the FNR was identical in all external dimensions to the HEU fuel as shown in Table 6 . The conversion to LEU fuel results in an increase in U-238 loading by a factor of nearly 5 and an increased U-235 loading to overcome the increased capture in U-238. To accommodate the additional uranium loading, the fuel meat thickness was increased 50% with a corresponding reduction in the

Table 6. HEU and LEU Fuel Designs

	HEU	LEU
Fissile enrichment	93%	19.5%
Regular element fissile loading (gm)	140.0	167.3
Uranium density in fuel meat (w/o)	14.1%	42%
Fuel plates per element	18	18
Fuel meat thickness (in)	.020	.030
Clad thickness (in)	.020	.015
Fuel plate thickness (in)	.060	.060
Water Channel thickness (in)	.117	.117

cladding thickness, hence keeping a constant fuel plate thickness. The FNR licensing considerations dictated the use of fuel with at most 42.0 w/o uranium loading, which is considered to be an acceptable fuel design based on experience and testing to date. Using 19.5% enriched uranium, the above LEU design has 167.3 g of U-235 per fuel element, and results in the same excess reactivity for the batch core as the HEU fuel design, as desired.

B. Flux and Power Distributions

Calculated power distributions for both HEU and LEU cores are compared in Figures 5. and 6. for batch cores and equilibrium cores, respectively. Examination of these figures reveals only minor changes between LEU and HEU cores. The largest change in assembly power, a 3% relative increase, occurs for special element locations. Additionally, there is a small shift in the power distribution away from the heavy water tank and toward a slightly improved overall symmetry about the center. There is no evidence of changes which would required detailed thermal-hydraulic analysis; in fact, the ratio of peak to average assembly power is slightly reduced.

The calculated fast and thermal flux distributions are compared in Figures 7. and 8. for the batch and equilibrium cores, respectively. The figures indicate that the fast flux distribution is perturbed very little with LEU fuel. This is to be expected because the fast neutron production and removal rates are nearly equal for the two cores. The fast neutron production is approximately constant because the core power

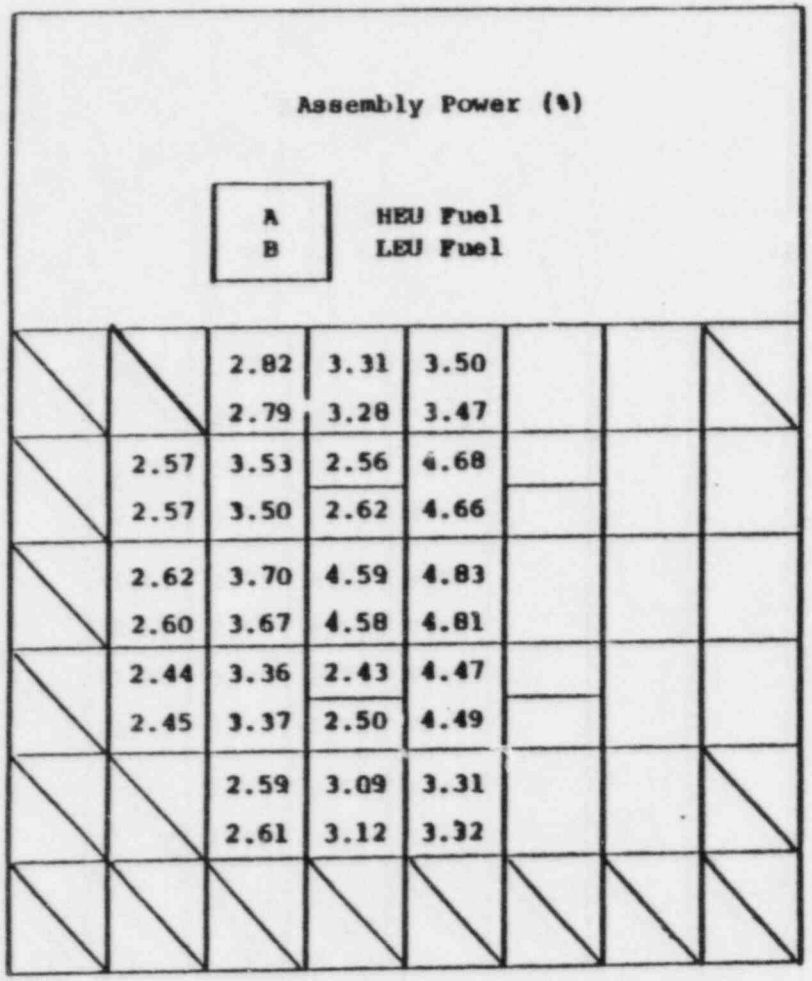

Figure 5. Assembly Power Distribution for HEU and LEU Batch Cores

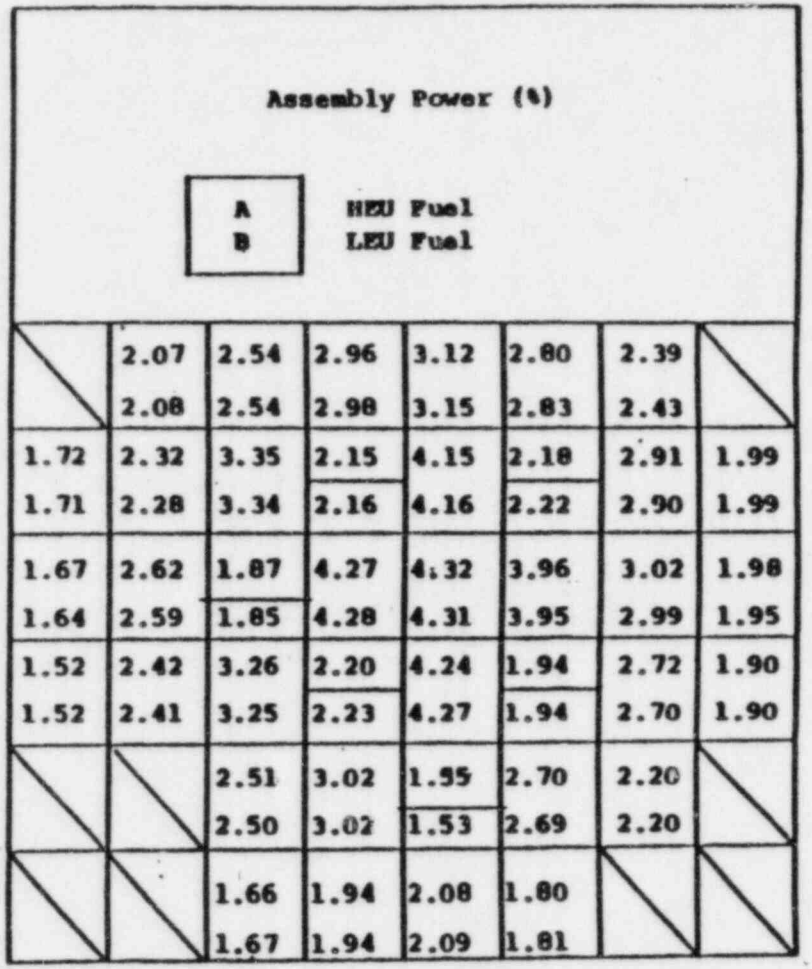

Figure 6. Assembly Power Distribution for HEU and LEU Equilibrium Cores

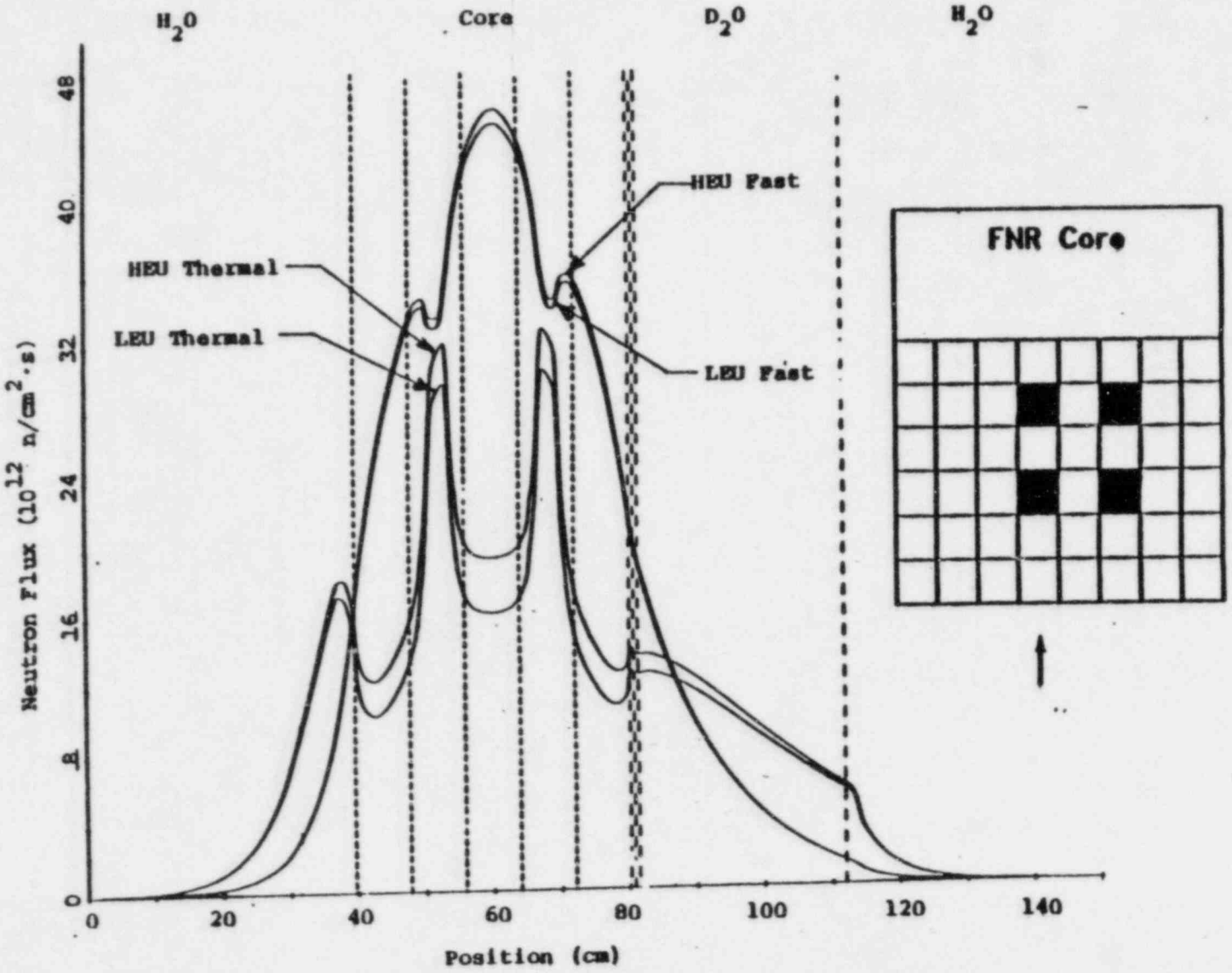

Figure 7. Neutron Flux Distribution for Batch Cores

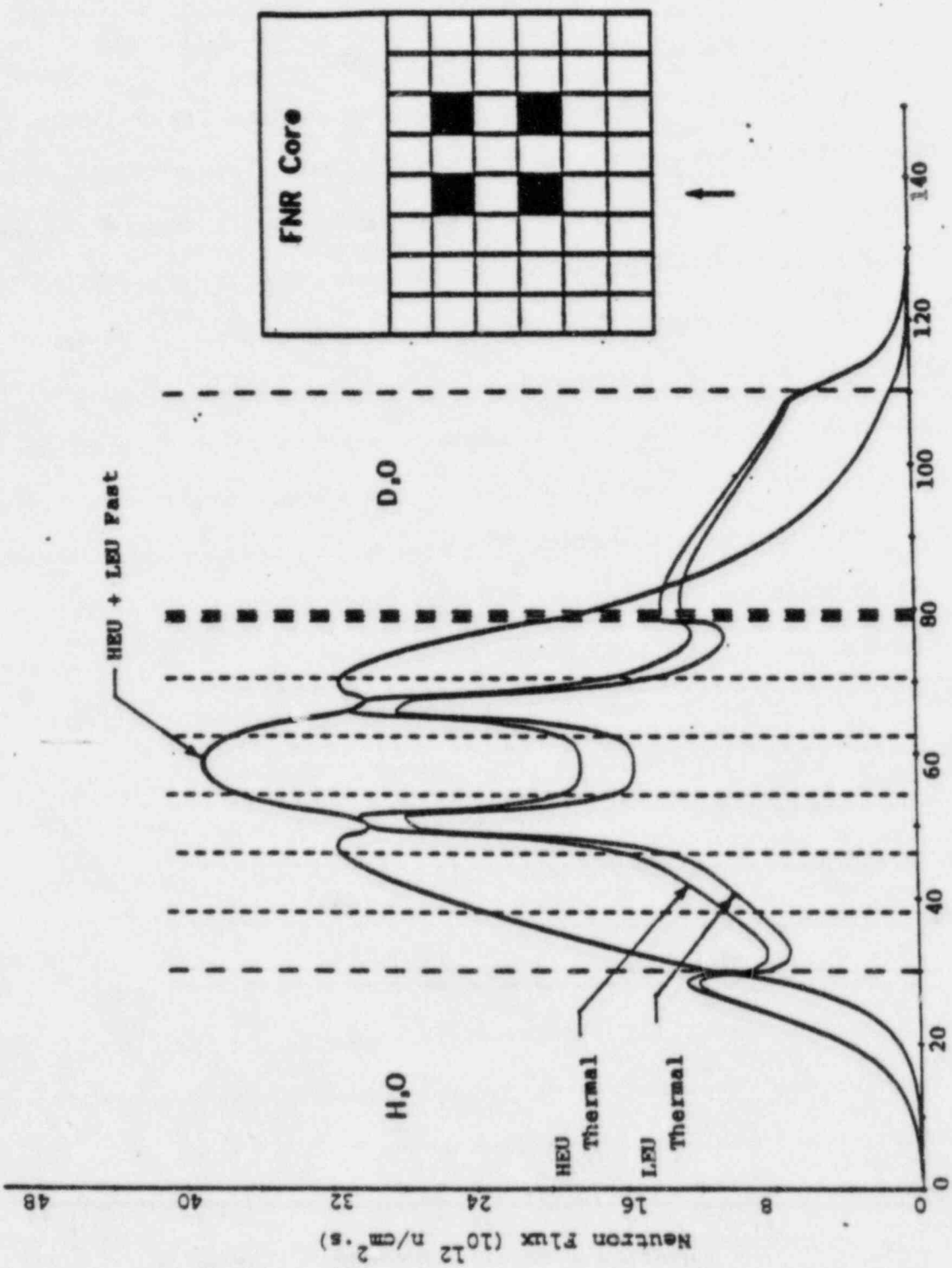

Figure 8. Neutron Flux Distribution for Equilibrium Cores

is held constant at 2 MW, while the fast neutron removal rate is nearly constant due to the similar moderating properties of the two cores. That is, the water channel dimensions are the same.

However, one expects to see significant changes in the incore thermal flux distributions between the HEU and LEU fuels. For a well-moderated thermal reactor at constant power, the thermal flux is nearly inversely proportional to the fissile loading, hence one expects a reduction in thermal flux for the LEU core. This effect is readily apparent in Figures 9. and 10. where the thermal flux in regular fuel elements is seen to decrease by about 18%. For special fuel elements, the reduction in thermal flux is only about 12%. This mitigation in the thermal flux decrease results from the effect of the thermal flux peaking in the large waterhole. This peak is primarily dependent on the fast flux, which is not significantly different between the LEU and HEU fuels. Since the thermal flux level within the special element will be affected by the waterhole peaking, the overall effect is to mitigate the decrease in thermal flux. As noted for the power distribution, there is a slight shift in thermal flux away from the heavy water tank toward a slightly improved overall symmetry about the center.

Excore thermal flux levels are important in the FNR because samples are generally irradiated in the reflector regions. In particular the heavy water reflector is of greatest interest because thermal neutron beam tubes extend from the tank to the laboratory areas. Comparisons of the thermal flux levels in the light water reflector show a flux depression varying from zero to 6%. At distances well into the light water reflector, there is no change because the primary source for

Assembly-Averaged Thermal Flux (10^{13} n/cm^2·sec)

A — HEU Fuel
B — LEU Fuel

		1.22 1.05	1.40 1.20	1.48 1.26			
	1.11 .96	1.51 1.30	2.44 2.21	2.00 1.74			
	1.13 .97	1.55 1.33	1.93 1.66	2.03 1.74			
	1.05 .92	1.44 1.25	2.34 2.14	1.92 1.67			
		1.13 .99	1.32 1.14	1.41 1.22			

Figure 9. Thermal Flux Distribution for HEU and LEU Batch Cores

Assembly-Averaged Thermal Flux (10^{13} n/cm^2·sec)

A — HEU Fuel
B — LEU Fuel

	1.01 .87	1.19 1.02	1.38 1.19	1.37 1.18	1.29 1.11	1.09 .95	
.87 .75	1.16 .98	1.57 1.33	2.40 2.15	1.84 1.58	2.23 1.99	1.33 1.14	1.00 .86
.86 .73	1.27 1.08	2.20 1.97	1.92 1.65	1.84 1.56	1.74 1.48	1.37 1.16	1.02 .87
.79 .69	1.16 1.00	1.53 1.31	2.37 2.12	1.88 1.61	2.20 1.97	1.34 1.14	.97 .83
		1.21 1.04	1.39 1.19	1.92 1.73	1.34 1.15	1.11 .96	
		.83 .72	.94 .81	.98 .84	.93 .81		

Figure 10. Thermal Flux Distribution for HEU and LEU Equilibrium Cores

thermal neutrons is the slowing down of fast neutrons leaking from the core. At locations closer to the core the contribution to the thermal flux due to thermal leakage from the core is larger and, since the thermal leakage is decreased by the increased fuel loading, there is a correspondingly greater decrease in the thermal flux. Consistent with this explanation, the relative thermal flux in the heavy water tank is depressed somewhat more (4-8%) than in the light water reactor due to the increase in the relative contribution of thermal leakage to the heavy water tank thermal flux.

C. Temperature Coefficient of Reactivity and Power Defect

The isothermal temperature coefficient of reactivity was computed for the batch core model to be -8.4 pcm/°F for the HEU fuel and -12.6 pcm/°F for the LEU fuel. The large increase is due almost exclusively to the fuel Doppler effects. For the HEU fuel, fuel Doppler effects are negligible due to the small amount of U-238 present. For the LEU fuel, the large amount of U-238 increases resonance absorptions in U-238, resulting in much larger sensitivity to fuel temperature. The principal contribution to the temperature coefficient of reactivity for both the HEU and LEU configurations is, however, the effect of the reduction in moderator density on leakage and moderation.

As discussed earlier, the procedure for calculating the power defect has not been fully developed, and a comparison of the difference in the power defect for the HEU and LEU cores has not been made. However, a preliminary estimate has been made based on the observation that the increase in the fuel Doppler effect is the principal difference in the temperature effects between the HEU and the LEU designs. The change in

power defect of reactivity is estimated in the present analysis on the basis of calculated temperature coefficients. Based on an average core temperature rise of 7°F, the power defect for the LEU fuel is estimated to be about .03% Δk/k larger in magnitude than for HEU fuel. For a typical FNR configuration, the excess reactivity required to overcome the power defect would thus change from a measured value of .21% Δk/k for HEU to .24% Δk/k for LEU.

D. Xenon Reactivity Worth

The xenon reactivity worths of the HEU and LEU fuels are compared in Tables 7. and 8. for the batch and equilibrium core models, respectively. For these cores the xenon worth is 4-6% lower for the LEU than the HEU fuel. There are two competing effects responsible for this decrease: First, the larger U-235 loading for the LEU core results in lower incore thermal flux levels, with a greater (10-12%) xenon concentration. Second, the increased fuel loading gives the LEU core a larger neutron absorption cross section. As total core absorption is increased, the fractional absorption in xenon, and thus the xenon reactivity worth, is decreased. Although these two effects tend to cancel one another, the latter effect dominates and xenon reactivity worth is lowered by about .1% Δk/k.

E. Fuel Cycle Analyses

Equilibrium fuel cycle analyses have been performed for the HEU and LEU cores and the results are presented in Table 9. The comparison of discharge fuel burnup, which indicates a 50% increase for LEU fuel, should be viewed with some care because of the extreme sensitivity of

Table 7. Batch Core Reactivity Comparisons

	HEU	LEU	Change
Cycle length (days)	10.0	10.0	
Burnup reactivity change rate (%Δk/k/day)	-.028	-.02	-28%
Shim rod worth (%Δk/k)			
A Rod	2.37	2.26	
B Rod	2.23	2.12	
C Rod	2.37	2.26	
Total	6.97	6.64	-4.7%
Excess reactivity required (%Δk/k)			
Xenon poisoning	2.50	2.40	-4.0%
Burnup effect	0.28	0.21	
Power defect	0.21	0.24	
Total	2.99	2.85	-4.7%
Shutdown margin (%Δk/k)	3.98	3.79	-4.0%

Table 8. Equilibrium Core Reactivity Comparisons

	HEU	LEU	Change
Cycle length (days)	11.0	16.5	50%
Burnup reactivity change rate (%Δk/k/day)	-.028	-.021	-24%
Shim rod worth (%Δk/k)			
A Rod	2.20	2.14	
B Rod	2.21	2.15	
C Rod	2.00	1.96	
Total	6.41	6.25	-2.5%
Excess reactivity required (%Δk/k)			
Xenon poisoning	2.26	2.17	-4.0%
Burnup effect	.31	.37	
Power defect	.21	.24	
Total	2.78	2.78	0%
Shutdown margin (%Δk/k)	3.63	3.47	-4.4%

Table 9. Equilibrium Core Fuel Cycle

	HEU	LEU	Change
Cycle length (days)	11.0	16.5	50%
Discharge burnup (MWD/element)			
Regular	19.2	28.7	49%
Special	16.9	25.9	53%
Regular element Fissile loading (gm)			
Fresh	140.6	167.3	20%
Discharge	116.6	134.3	15%
Core loading Beginning of cycle (gm)			
Fissile	4550	5320	17%
U-235	4549	5260	16%
Burnup reactivity change rate (% Δk/k/day)	.0279	.0211	-24%

discharge fuel burnup to core reactivity for the FNR core. For example, in an equilibrium core analysis comparing two LEU core configurations, a 0.5% $\Delta k/k$ change in eigenvalue resulted in a 15% increase in the discharge burnup. This sensitivity is a consequence of the relatively low fissile depletion obtained in the FNR core. Typically only 17% of the initial fissile inventory is depleted from the HEU fuel elements before discharge. A significant change in the discharge fissile depletion can be achieved with only a small relative change in the total core fissile inventory, which is, of course, proportional to core criticality. Thus, the predicted discharge burnup is very sensitive to the calculated core criticality. In addition, this sensitivity is magnified by the in/out shuffling pattern used at the FNR. This shuffling scheme loads the depleted fuel elements into regions of lower neutron importance. Thus, changes in the discharge burnup have a relatively smaller effect on core criticality than with other shuffling schemes. Because core size and core criticality are directly related, discharge fuel burnup is also sensitive to core size. Therefore, to provide valid comparisons a fixed core size was used in our equilibrium core analysis. Calculations for both the batch and equilibrium cores indicate a decrease in the burnup reactivity change rate with LEU fuel. The decrease in reactivity change rate is a consequence of two factors. Most importantly, the core fissile loading is higher with LEU fuel, so that the fractional fuel depletion rate, and the burnup reactivity change rate, are lowered. Production of Pu-239 in the LEU fuel also causes a decrease in the burnup reactivity change rate. Fuel depletion calculations indicate that the Pu-239 production rate is approximately 8% of the U-235 loss rate in the LEU core. This may translate into a 10-15% decrease in the burnup reactivity change rate, depending on the

reactivity worth of Pu-239 vs. U-235. Comparisons of reactivity changes in the HEU and LEU batch cores show that during the first 50 full power days of operation reactivity is lost more rapidly than at later times due to the effects of xenon and samarium, as well as fuel depletion. Once this initial transient has passed the burnup reactivity change rates are nearly constant and approximately 25 to 30% lower in the LEU core. In the equilibrium core calculations the burnup reactivity change rate is affected by the fuel burnup distribution as well as total core fissile inventory. For this equilibrium core model the burnup reactivity change rate is decreased by 24% with the LEU fuel. Thus, as explained earlier a 30% increase in the FNR operating cycle length is expected.

F. Control Rod Worth

Shim rod reactivity worth comparisons for the A, B, and C rods are given in Tables 7 and 8. The LEU batch core comparison shows a 5% relative decrease in shim rod worth. This decrease in rod worth may be explained qualitatively by noting that, to a good approximation, the FNR rods are black and, for a black rod control, rod worth is nearly proportional to the product of the control surface area and the thermal diffusion length in the surrounding fueled region.[20] Since the thermal diffusion length in the LEU core is 2.05 cm vs. 2.18 cm in the HEU core, this simple model predicts a decrease in rod worth of approximately 6%, which may be compared with the calculated 5% decrease in rod worth for the batch core configuration. In the equilibrium configuration the total rod worth decreases by only 3%. This smaller decrease in rod worth indicates that factors other than the shorter thermal diffusion length are also affecting the calculated rod worth. Rod worth calcu-

lations for various equilibrium cores show that rod worth is also affected by the discharge fuel burnup. As discharge burnup in the outer fuel elements is increased, the core fissile loading and core reactivity worth distribution shift toward the core center causing the rod worth to increase. Thus the higher discharge burnup in the LEU equilibrium core has a mitigating effect on the decrease in rod worth, and the net effect is a 3% decrease in total worth.

G. Comparison of Shutdown Margin

The most significant safety parameter related to core physics analysis is the shutdown margin. This parameter is obtained by subtracting the positive core excess reactivity required to overcome xenon poisoning, fuel depletion, and the power defect from the total control rod reactivity worth. The present technical specifications require that the shutdown margin be at least 3.0% Δk/k. Any difference between the estimated shutdown margin and the limiting value represents excess reactivity available for experiments.

For the LEU batch core, it is seen from Table 7, that the lower excess reactivity requirement is overshadowed by the decrease in control rod reactivity worth. The shutdown margin of 3.79% Δ k/k is lower than for the HEU core, but is still well above the 3% Δk/k requirement. Additionally, with the most reactive rod fully withdrawn, the shutdown margin is 1.53% Δk/k, well in excess of the .75% Δk/k required.

Comparing the HEU and LEU equilibrium core results in Table 8. shows that the shutdown margin decreases slightly for the LEU core. The computed value of 3.47% Δk/k is well in excess of the 3.0% Δk/k requirement. Also, the shutdown margin with the most reactive control rod fully withdrawn is 1.32% Δk/k, well above the .75% Δk/k required.

VII. ALTERNATIVE LEU FUEL DESIGNS

The LEU fuel design was selected for the full core demonstration based on a criterion of creating minimum perturbations in reactor performance. To determine effective ways of improving core performance, e.g., the core fuel burnup, control rod worth, and excore flux levels, several alternative LEU fuel designs have also been studied.

This section presents results of an equilibrium core study comparing the LEU fuel with an alternative higher loaded fuel design. The two fuel designs are compared in Table 10 . The fissile loading for the alternative fuel design has been increased to 175 gm by increasing the uranium density in the fuel meat, without changing element dimensions. The important conclusion of this alternative fuel design study is that it may be possible to significantly increase fuel burnup without degrading other reactor performance characteristics.

The equilibrium core power and thermal flux distributions for the two fuels are compared in Figures 11, 12 and 13. The power distribution comparisons show only a slight shift for the higher loaded fuel, despite the increase in fuel burnup at the core edges. A maximum increase of about 2% in assembly power occurs near the core center and the heavy water tank. The thermal flux distribution comparison shows a maximum decrease of less than 3%, suggesting that the flux depression caused by the higher loading is partially mitigated by the higher fissile depletion.

Equilibrium core calculations predict a 26% increase in cycle length and discharge burnup for the 175 gm fuel. As explained earlier, the higher discharge burnup results because the fuel can be depleted longer while maintaining a critical equilibrium configuration. The 175 gm fuel

Table 10. LEU Fuel Design Comparisons

	Reference Design	Alternative Design	Change
Enrichment	19.5%	19.5%	0%
Regular element fissile loading (gm)	167.3	175.0	4.6%
Uranium density in fuel meat	42.0%	43.9%	4.6%
Element dimensions	——	——	0%
Equilibrium cycle length (days)	16.5	20.8	26%
Discharge burnup (MWD/element)			
Regular	28.7	36.4	27%
Special	25.9	32.5	24%
Burnup reactivity change rate (%Δk/k/day)	.0211	.0207	-2%
Shim rod worth (%Δk/k)			
A Rod	2.14	2.15	
B Rod	2.15	2.14	
C Rod	1.96	2.00	
Total	6.25	6.29	0.6%
Excess reactivity required (%Δk/k)			
Xenon poisoning	2.17	2.15	
Burnup effect	.37	.43	
Power defect	.24	.24	
Total	2.78	2.82	1.4%
Shutdown margin (%Δk/k)	3.47	3.47	0%

Assembly Power (%)

A 167.3 gm LEU
B 175 gm LEU

	2.08	2.54	2.98	3.15	2.83	2.43	
	2.07	2.55	3.01	3.22	2.88	2.48	
1.71	2.28	3.34	2.16	4.16	2.22	2.90	1.99
1.68	2.24	3.36	2.14	4.23	2.26	2.95	1.99
1.64	2.60	1.85	4.28	4.31	3.95	2.99	1.95
1.59	2.56	1.79	4.34	4.40	4.01	3.01	1.93
1.52	2.41	3.25	2.23	4.27	1.94	2.70	1.90
1.48	2.38	3.25	2.22	4.34	1.90	2.68	1.87
		2.50	3.02	1.53	2.69	2.20	
		2.48	3.02	1.46	2.66	2.17	
		1.67	1.94	2.09	1.81		
		1.65	1.92	2.08	1.77		

Figure 11. Power Distribution for 167.3 and 175 gm LEU Equilibrium Cores

Assembly-Averaged Thermal Flux(10^{13} n/cm^2-sec)

A 167.3 gm LEU
B 175 gm LEU

	.87	1.02	1.19	1.18	1.11	.95	
	.86	1.01	1.18	1.17	1.10	.95	
.75	.98	1.33	2.15	1.58	1.99	1.14	.86
.73	.96	1.31	2.14	1.56	1.98	1.12	.86
.73	1.08	1.97	1.65	1.56	1.48	1.16	.87
.71	1.05	1.96	1.62	1.53	1.46	1.14	.86
.69	1.00	1.31	2.12	1.61	1.97	1.14	.83
.67	.97	1.29	2.10	1.58	1.96	1.13	.82
		1.04	1.19	1.73	1.15	.96	
		1.02	1.16	1.72	1.13	.95	
		.72	.81	.84	.81		
		.71	.79	.83	.79		

Figure 12. Thermal Flux for 167.3 and 175 gm LEU Equilibrium Cores

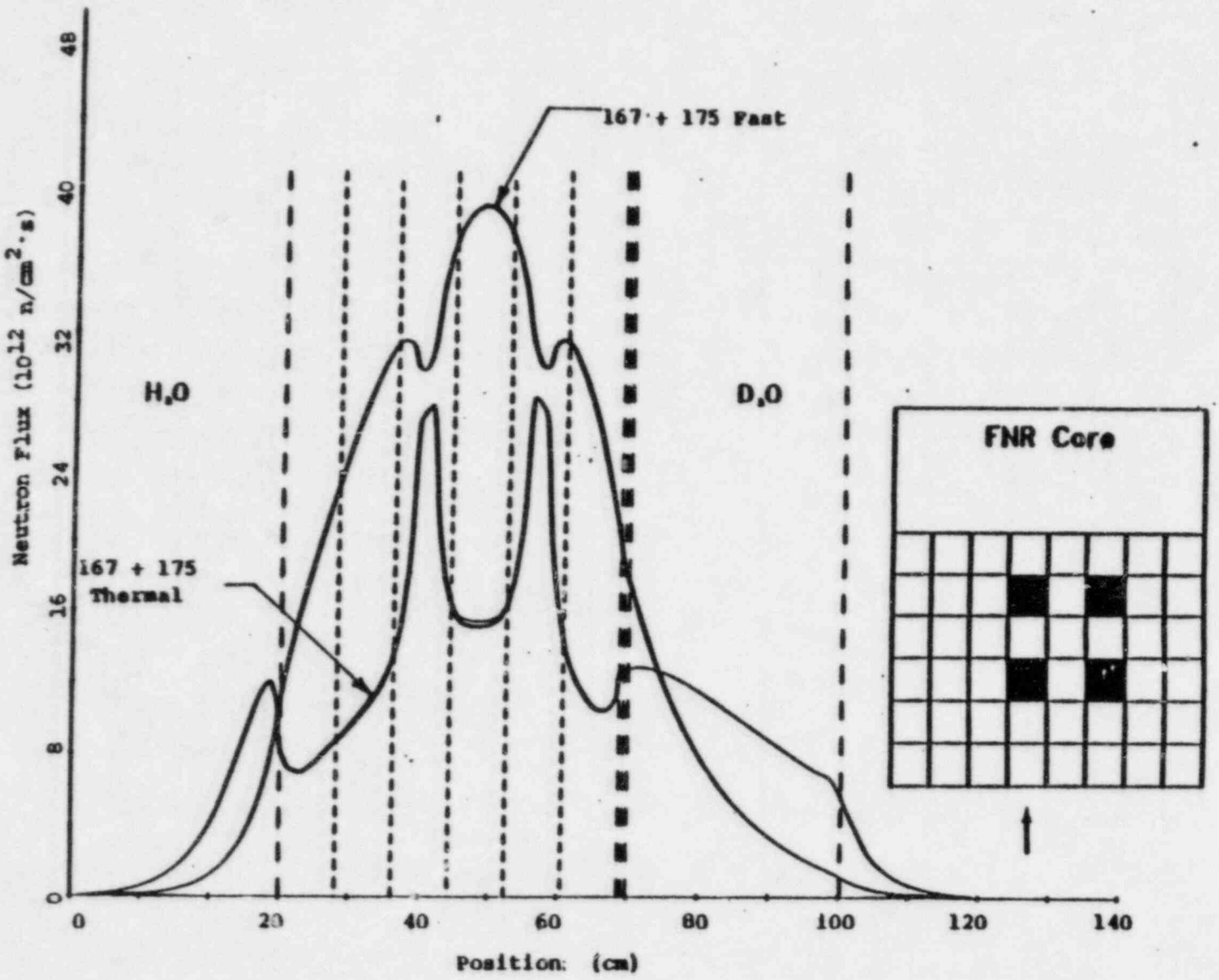

Figure 13. Neutron Flux Distribution for 167.3 and 175 gm LEU Fuels

is initially more reactive because of the higher fissile loading, and loses reactivity due to fuel burnup at a slower rate, as seen by the 2% decrease in burnup reactivity change rate. As noted earlier, however, care must be taken in interpreting these results because of the extreme sensitivity of discharge fuel burnup to core reactivity for the FNR.

Calculations of the reactivity effects for the two LEU fuels predict no change in shutdown margin with the higher loaded fuel. The control rod worth increases by an almost insignificant amount because the higher core edge depletion tends to increase core center reactivity worth. Thus the shutdown margin, as well as the core power and thermal flux distribution, are not significantly degraded even though the discharge burnup is considerably higher for the 175 gm fuel design.

VIII. SUMMARY

A 19.5% enriched fuel design was selected and is being fabricated as part of the FNR demonstration project. The fuel has a 167.3 gram fissile loading and 18 fuel plates per assembly. To accommodate the increased uranium content without changing fuel plate or assembly dimensions, the uranium loading in the fuel meat has been increased to 42 w/o and the fuel thickness has been increased 50% while decreasing the clad thickness.

Extensive efforts have been devoted to developing calculational methods for analyzing HEU and LEU fueled research reactors. These methods make use of existing well verified computer codes whenever possible and have been verified by comparison with data from several research reactor configurations.

To study all expected effects, the HEU fuel and LEU fuel were analyzed and compared in both batch and equilibrium core models. These comparisons serve to quantify predictions made on physical grounds: The higher fissile loading required to overcome the additional U-238 absorptions results in a large decrease in the in-core thermal flux. Thermal flux levels in the reflector are depressed to a lesser degree because the fast neutron leakage is nearly constant. The power distribution is not perturbed to a significant degree. The equilibrium cycle length and discharge fuel burnup are predicted to increase because the LEU core can be depleted longer while maintaining core criticality. There is a small decrease in the xenon worth and control rod worth caused by higher core absorption. Comparisons for the equilibrium cores indicate that the reduction in rod worth may be mitigated by the increased fuel burnup of the LEU core. Most importantly the comparisons predict no significant change in the core shutdown margin.

The analytic methods described in the paper have provided a reasonable assessment of the impacts of LEU fuel on FNR performance. However, there remain areas which deserve further study and additional refinement. Some specific items currently being investigated at The University of Michigan are:

1) Development of a new data library for the LEOPARD code based upon ENDF/B-IV data.
2) Investigation of optimal equilibrium core configurations using linear/dynamic programming concepts.
3) Continued investigation of discrepancies between measured and predicted rod worths, with a careful examination of possible boron depletion effects.
4) Calculation of β_{eff}, the effective delayed neutron fraction, for both HEU and LEU cores.

5) Refinement of the power defect calculation to include non-uniform axial effects.

6) Refinements in the determination and use of burnup dependent non-lattice peaking factors for the LEOPARD code.

7) Extensive analysis of the leakage flux levels in the FNR heavy water tank and beam port locations. Calculations are planned using both discrete ordinates and Monte Carlo methods.

REFERENCES

1. D. Wehe and J. S. King, "The FNR HEU-LEU Demonstration Experiment", (to be presented at this conference).

2. H. Komoriya, J. C. Lee, and W. R. Martin, Trans. Am. Nucl. Soc., 32, Suppl. 1, 31 (1979).

3. F. B. Brown, D. C. Losey, D. K. Wehe, J. C. Lee and W. R. Martin, Trans. Am. Nucl. Soc., 33, 746 (1979).

4. D. C. Losey, F. B. Brown, W. R. Martin, J. C. Lee, and H. Komoriya, Trans. Am. Nucl. Soc., 33, 748 (1979).

5. W. Kerr, et al., "Low Enrichment Fuel Evaluation and Analysis Program, Summary Report for the Period January 1979-December 1979", University of Michigan Report (Jan. 1980).

6. D. C. Losey, F. B. Brown, J. C. Lee and W. R. Martin, Trans. Am. Nucl. Soc., 34, 569 (1980).

7. R. F. Barry, "LEOPARD - A Spectrum Dependent Non-Spatial Depletion Code", WCAP-3269-26, Westinghouse Electric Corporation (Sept. 1963).

8. J. Barhen, W. Rothenstein, E. Taviv, "The HAMMER Code System", NP-565, Electric Power Research Institute (October 1978).

9. W. W. Little, Jr. and R. W. Hardie, "2DB User's Manual-Revision I", BNWL-831 REV1, Battelle Pacific Northwest Laboratory (February 1969).

10. W. W. Engle, Jr., "A User's Manual for ANISN, a One-Dimensional Discrete Ordinates Transport Code with Anisotropic Scattering", K-1693, Oak Ridge Gaseous Diffusion Plant (March 1967).

11. K. D. Lathrop and F. W. Brinkley, "TWOTRAN-II - An Interfaced Exportable Version of the TWOTRAN Code for Two-Dimensional Transport", Los Alamos Scientific Laboratory, LA-4848-MS (1973).

12. D. R. Vondy, T. B. Fowler, and G. W. Cunningham, "VENTURE: A Code Block for Solving Multigroup Neutronics Problems Applying the Finite-Difference Diffusion Theory Approximation to Neutron Transport", ORNL-5062 (1975).

13. M. H. Theys, Nucl. Sci. Eng., 7, 58 (1960).

14. J. Hardy, D. Klein, and J. J. Volpe, "A Study of Physics Parameters in Several Water-Moderated Lattices of Slightly Enriched and Natural Uranium:, WAPD-TM-931, Westinghouse Electric Corporation (March 1970).

15. E. B. Johnson, "Power Calibration for BSR Loading 33", CF-57-11-30, Oak Ridge National Laboratory (1957).

16. J. L. Shapiro, "The Void Coefficient in an Enriched, Water Reactor", Nucl. Sci. Eng., 12, 449 (1962).

17. H. Komoriya to J. L. Snelgrove, "Reduced Enrichment Fuel Element Loading Calculations for the Ford Nuclear Reactor", Argonne National Laboratory Internal Memorandum (February 14, 1979).

18. J. E. Matos and K. E. Freese, Trans. Am. Nucl. Soc., 33, 739 (1979).

19. H. Komoriya, Trans. Am. Nucl. Soc., 33, 745 (1979).

20. J. J. Duderstadt and W. R. Martin, Transport Theory, Wiley-Interscience, New York (1979).

APPENDIX C

DOCUMENTATION FOR DATA BANK

In this appendix we present a limited selection of the data describing the current and proposed FNR fuel elements. These data are included to provide documentation for our calculations and hopefully are sufficiently detailed to allow others to make similar calculations. Vendor drawings of both the HEU and LEU fuels and also the FNR control rods are presented first. By using information gathered from vendor drawings, fuel specifications, and a number of other sources, Table C-2 has been made which summarizes the fuel element dimensions and composition. There is considerable uncertainty in the entries of this table because of the large tolerances in the fuel element specifications and because there is very little information describing actual as-built fuel element geometry and composition. The data represent our best estimates of actual fuel element geometry and composition, and are consistent in that different fuel element types are compared on an equal basis.

We also include a limited selection of a reference cross section library in Table C-4. The library was generated with the LEOPARD code using the data from Table C-2. describing fuel element dimensions and composition.

Table of Contents for Appendix C

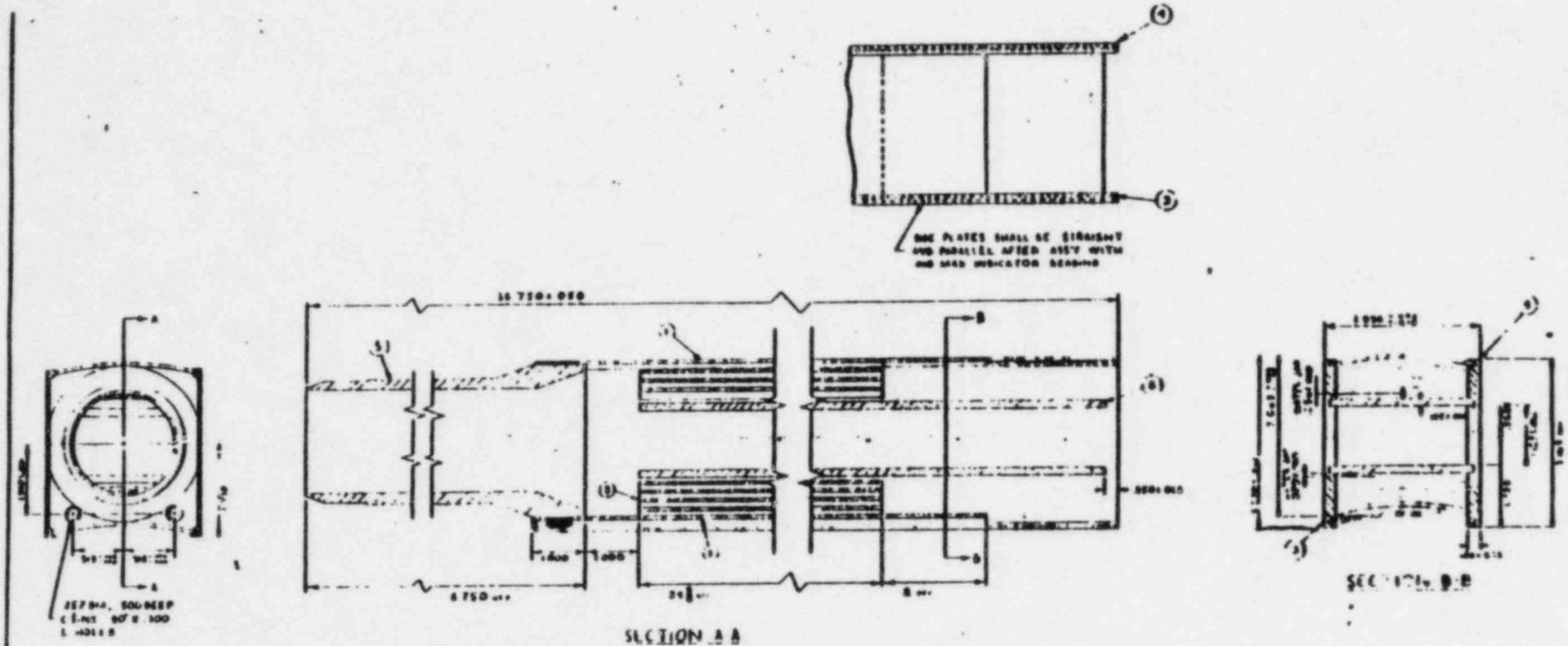

Fig. C-1. HEU Alloy Special Element

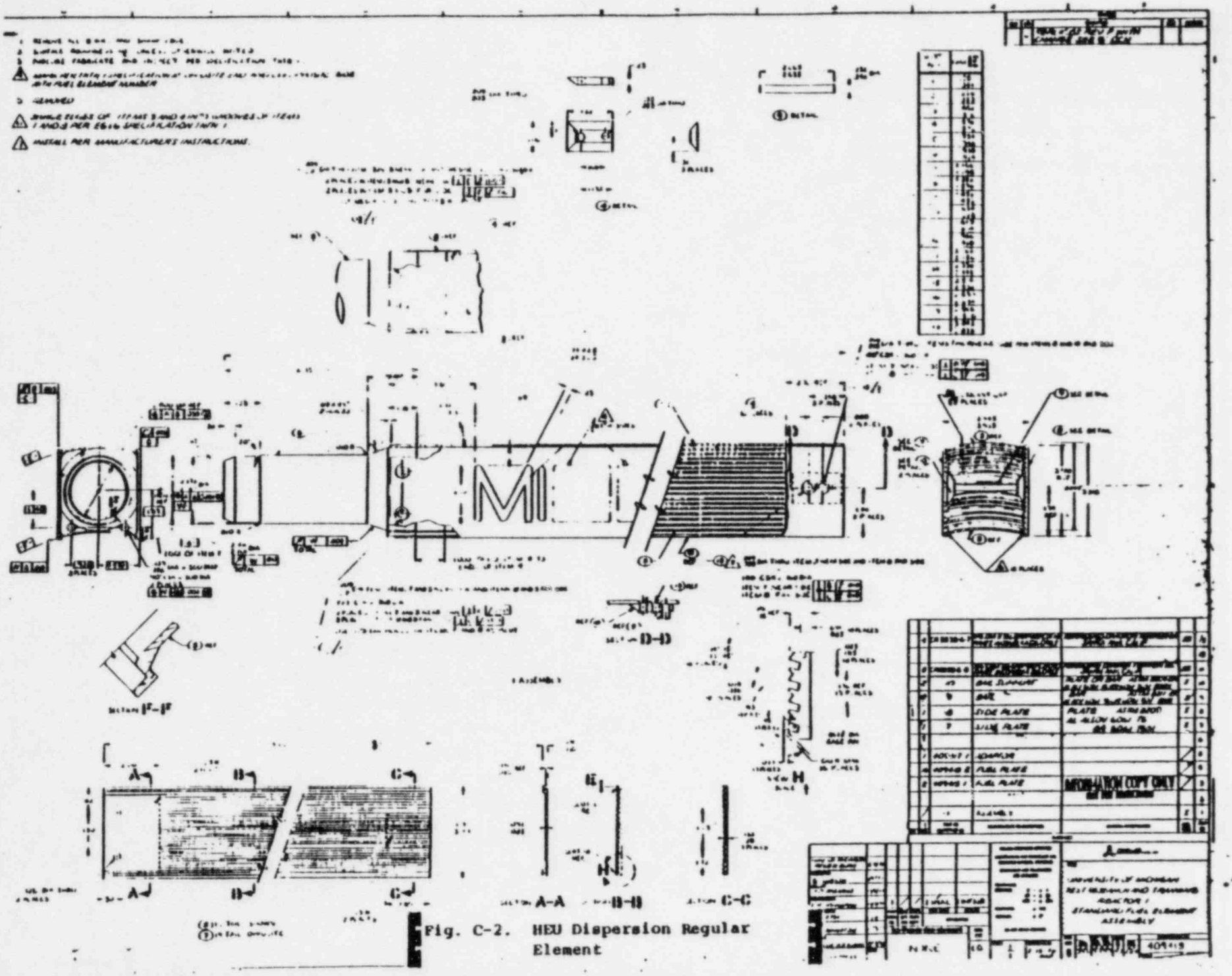

Fig. C-2. HEU Dispersion Regular Element

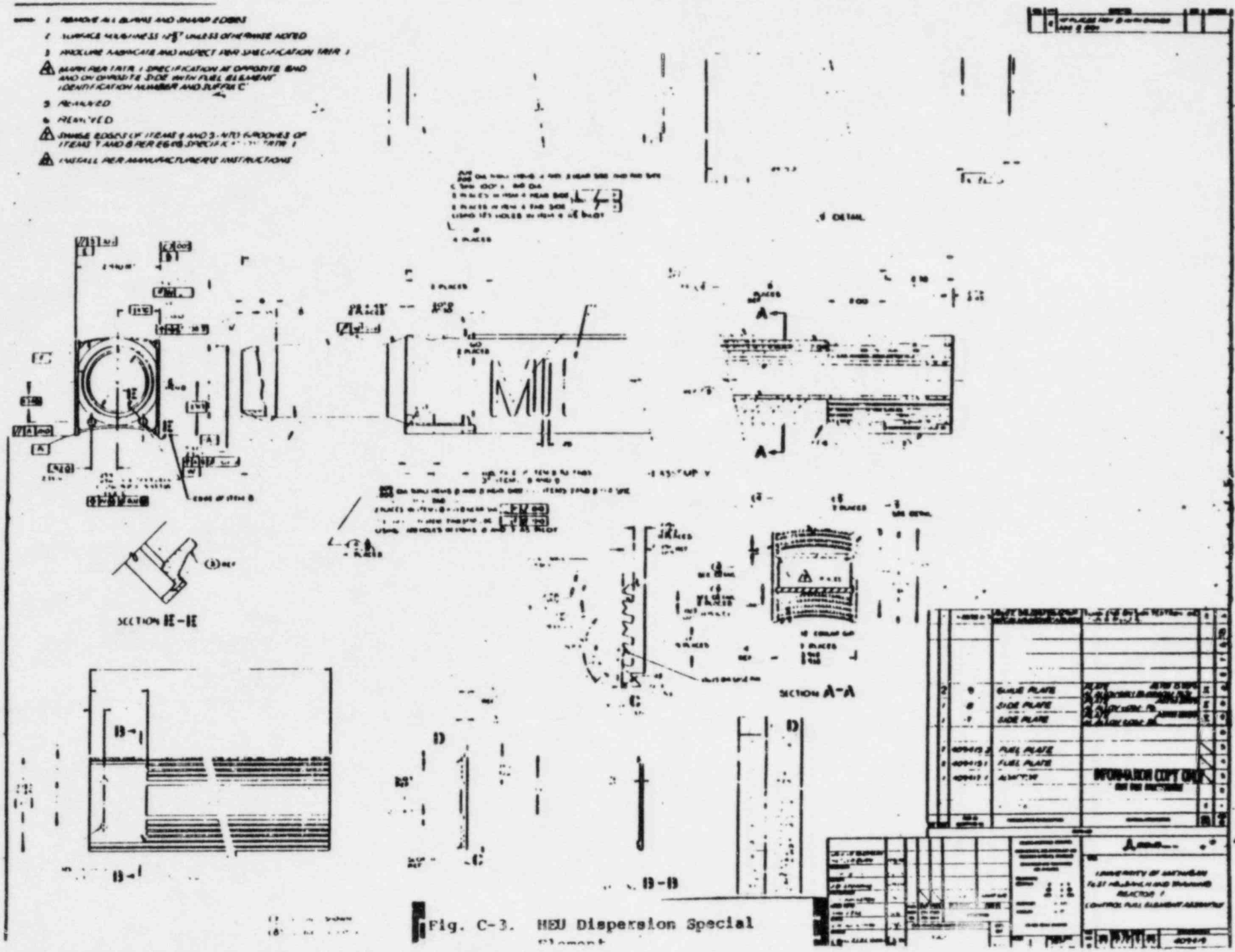

Fig. C-3. HEU Dispersion Special Element

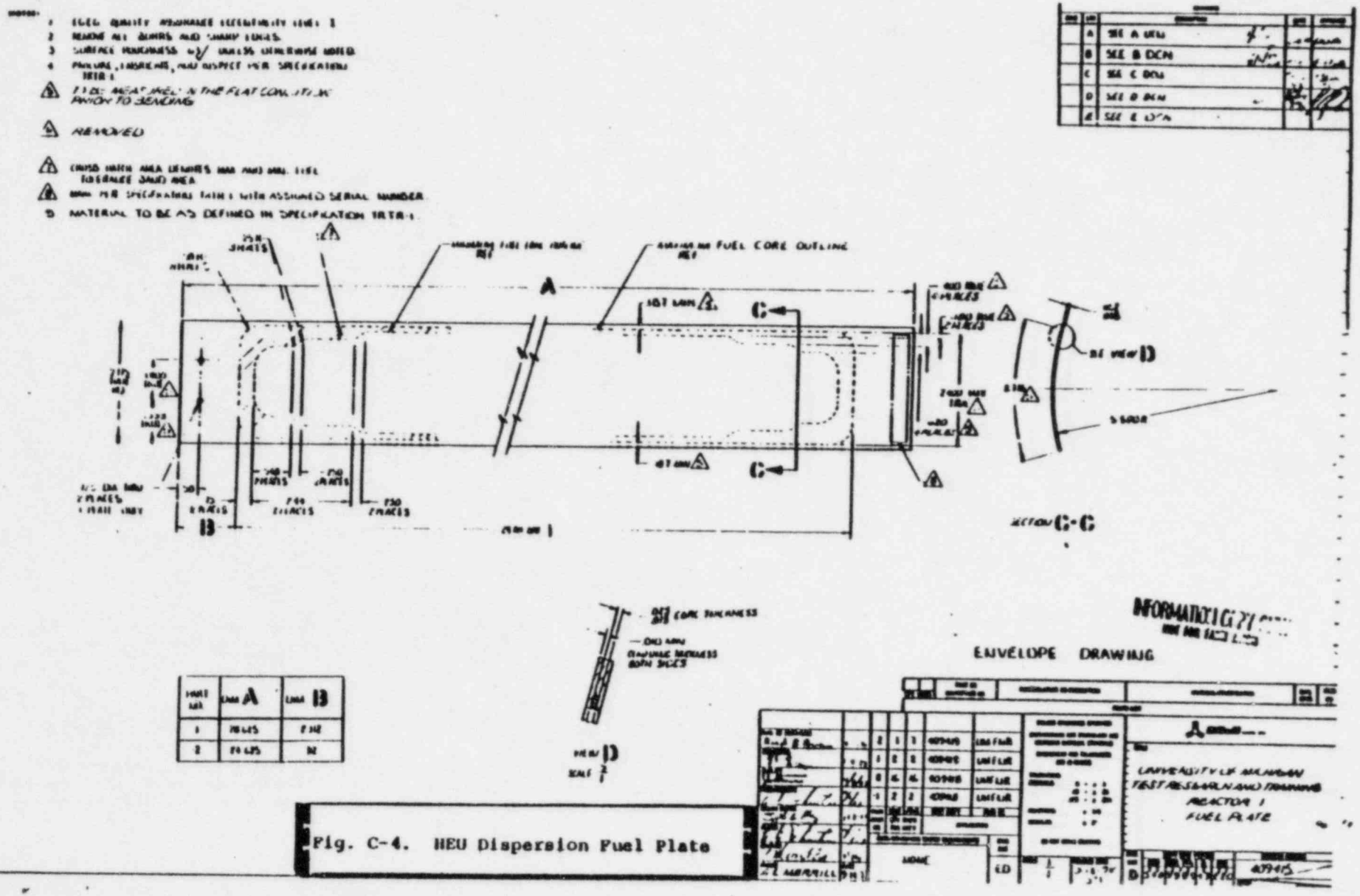

Fig. C-4. HEU Dispersion Fuel Plate

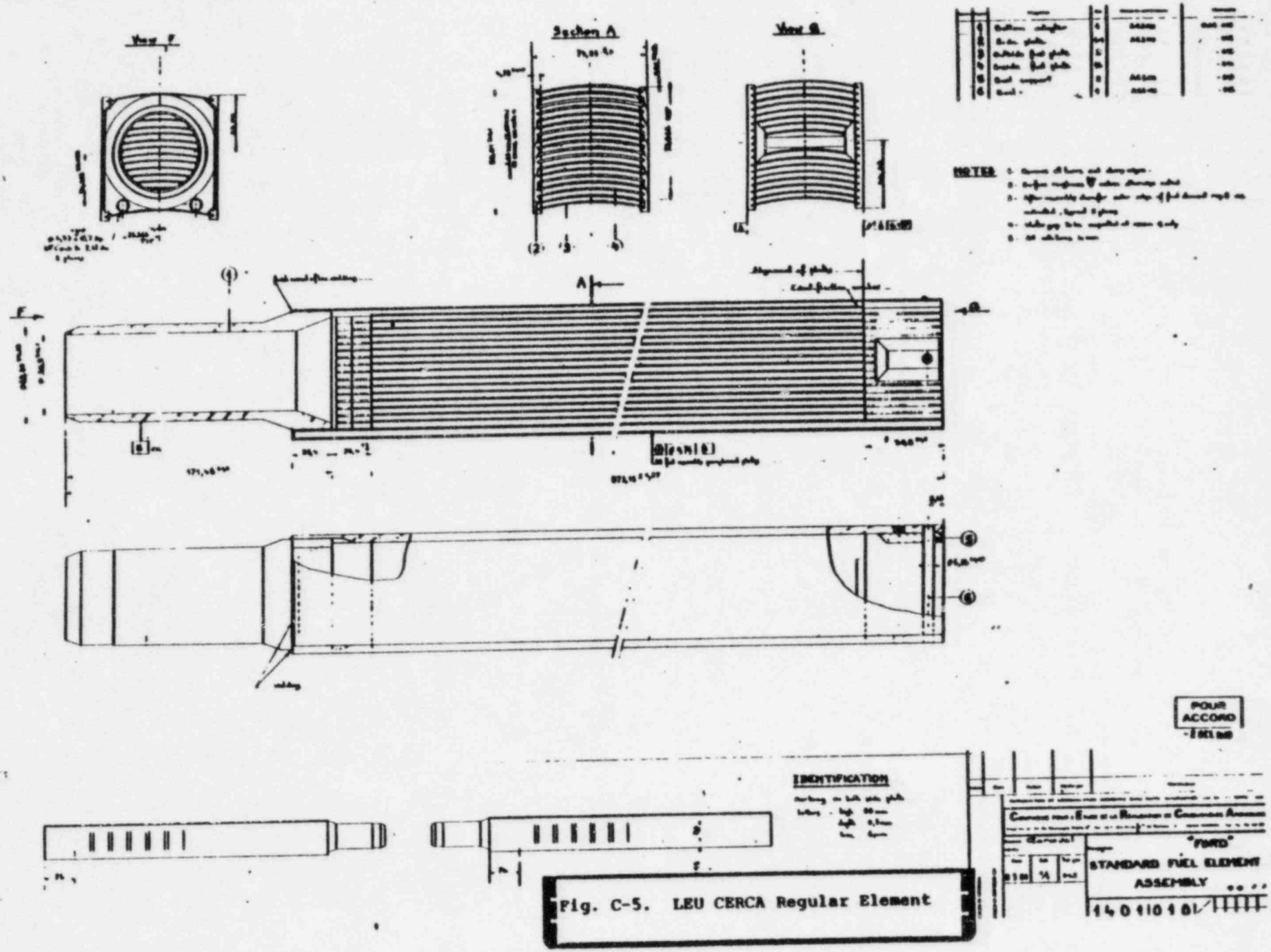

Fig. C-5. LEU CERCA Regular Element

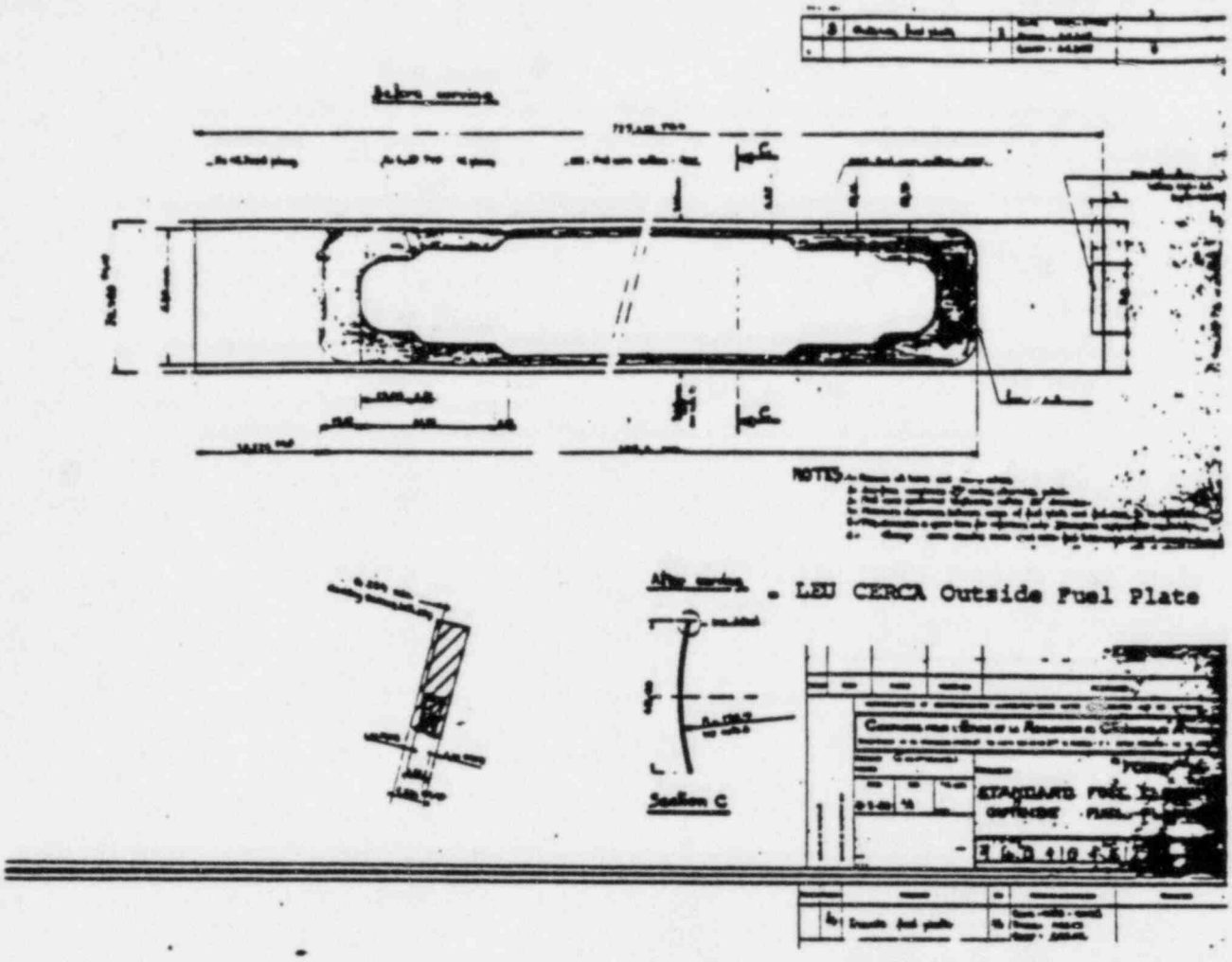

LEU CERCA Outside Fuel Plate

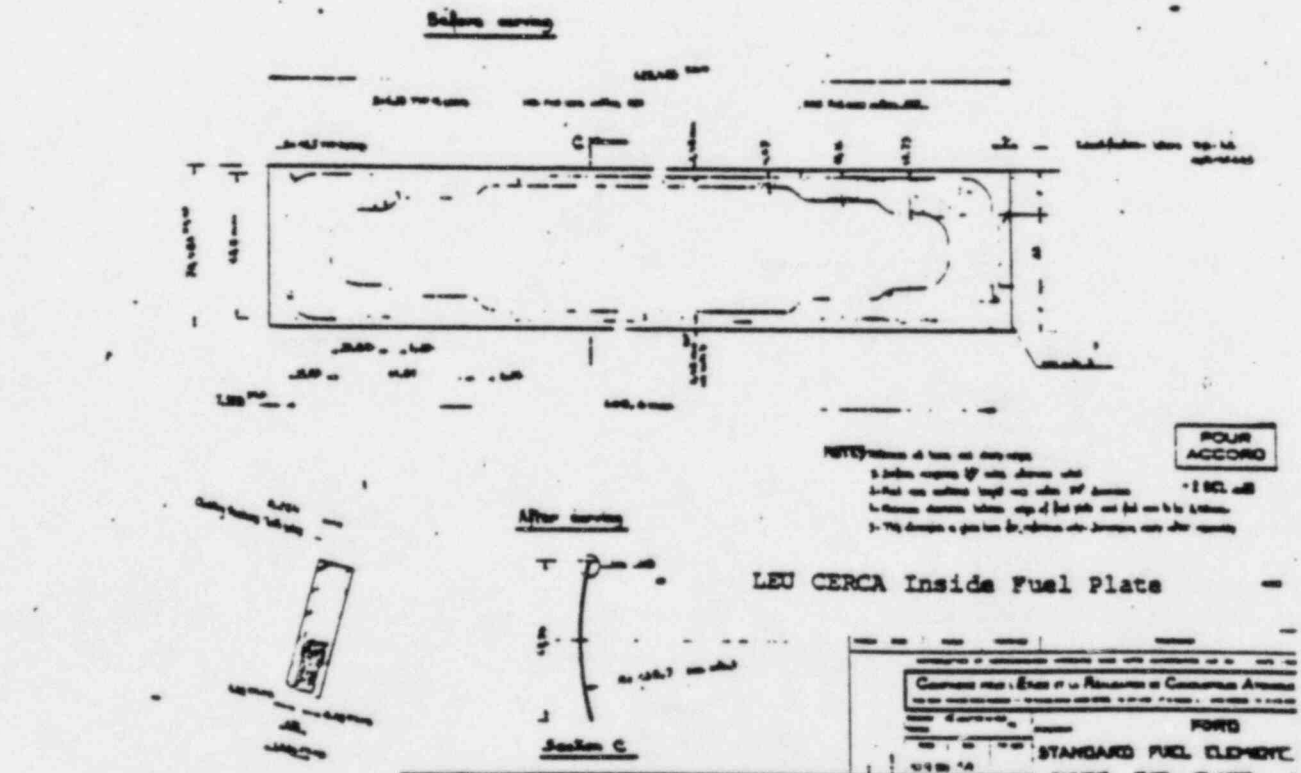

LEU CERCA Inside Fuel Plate

Fig. C-6. LEU CERCA Fuel Plates

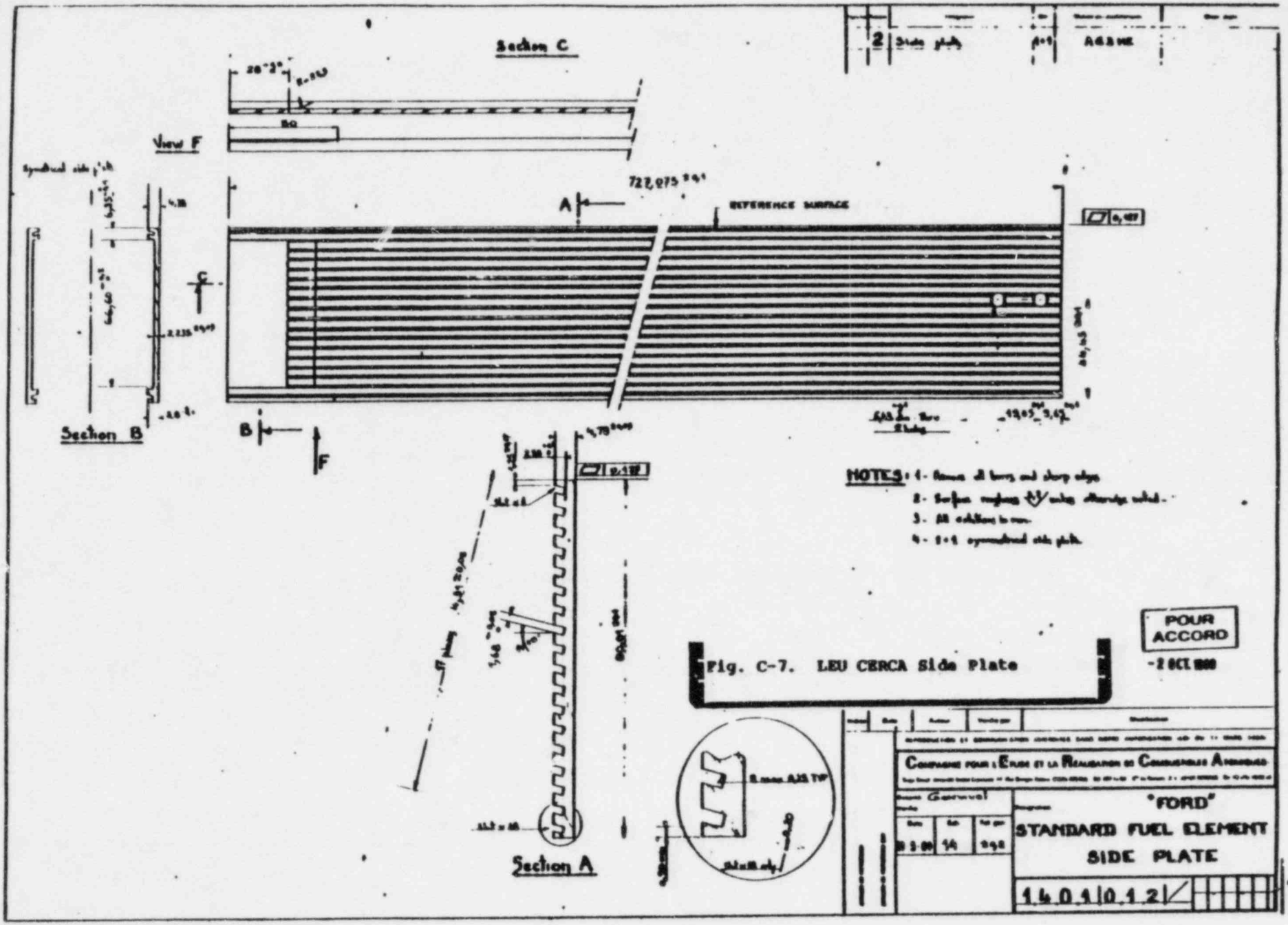

Fig. C-7. LEU CERCA Side Plate

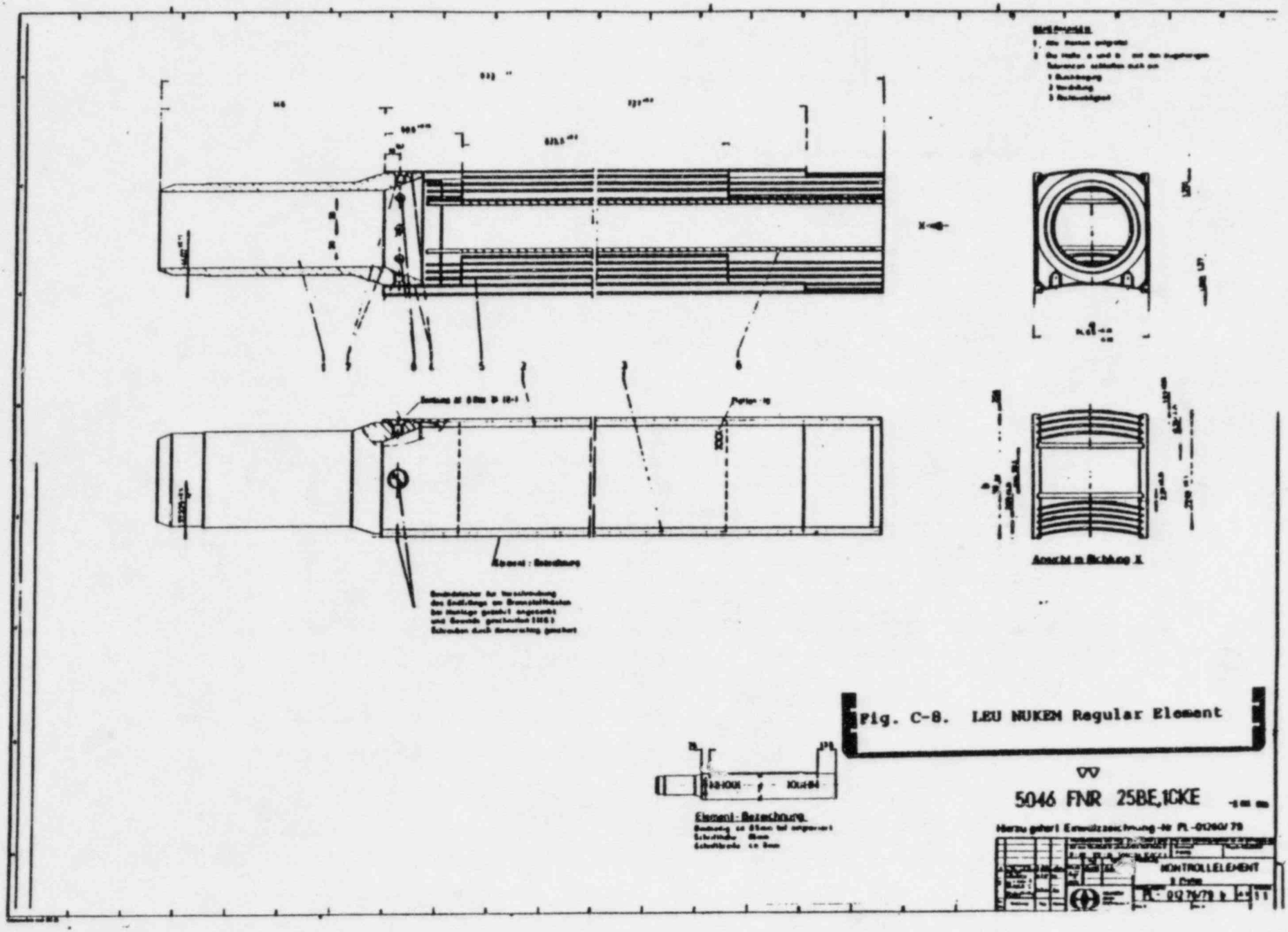

Fig. C-8. LEU NUKEM Regular Element

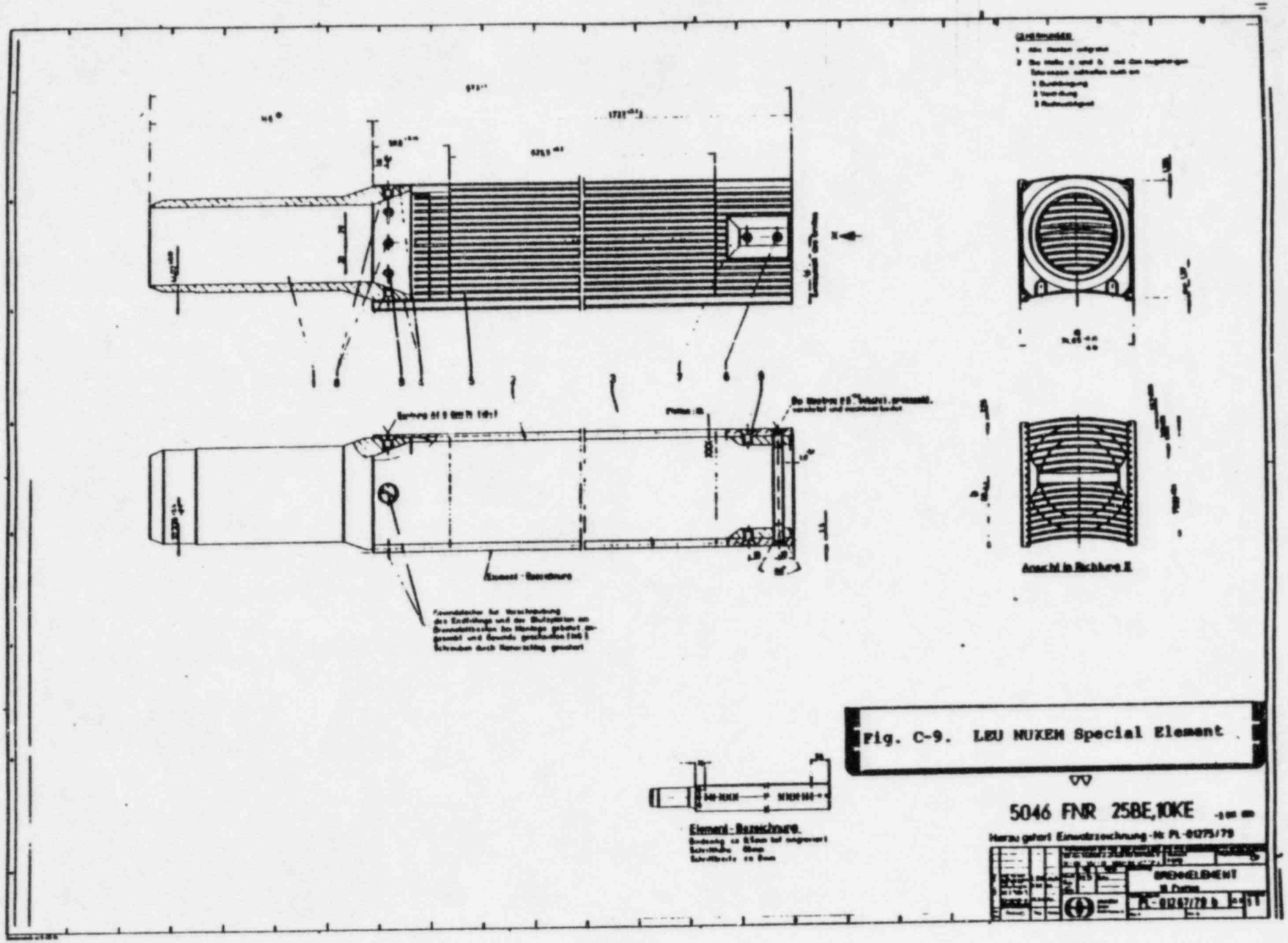

Fig. C-9. LEU NUKEM Special Element

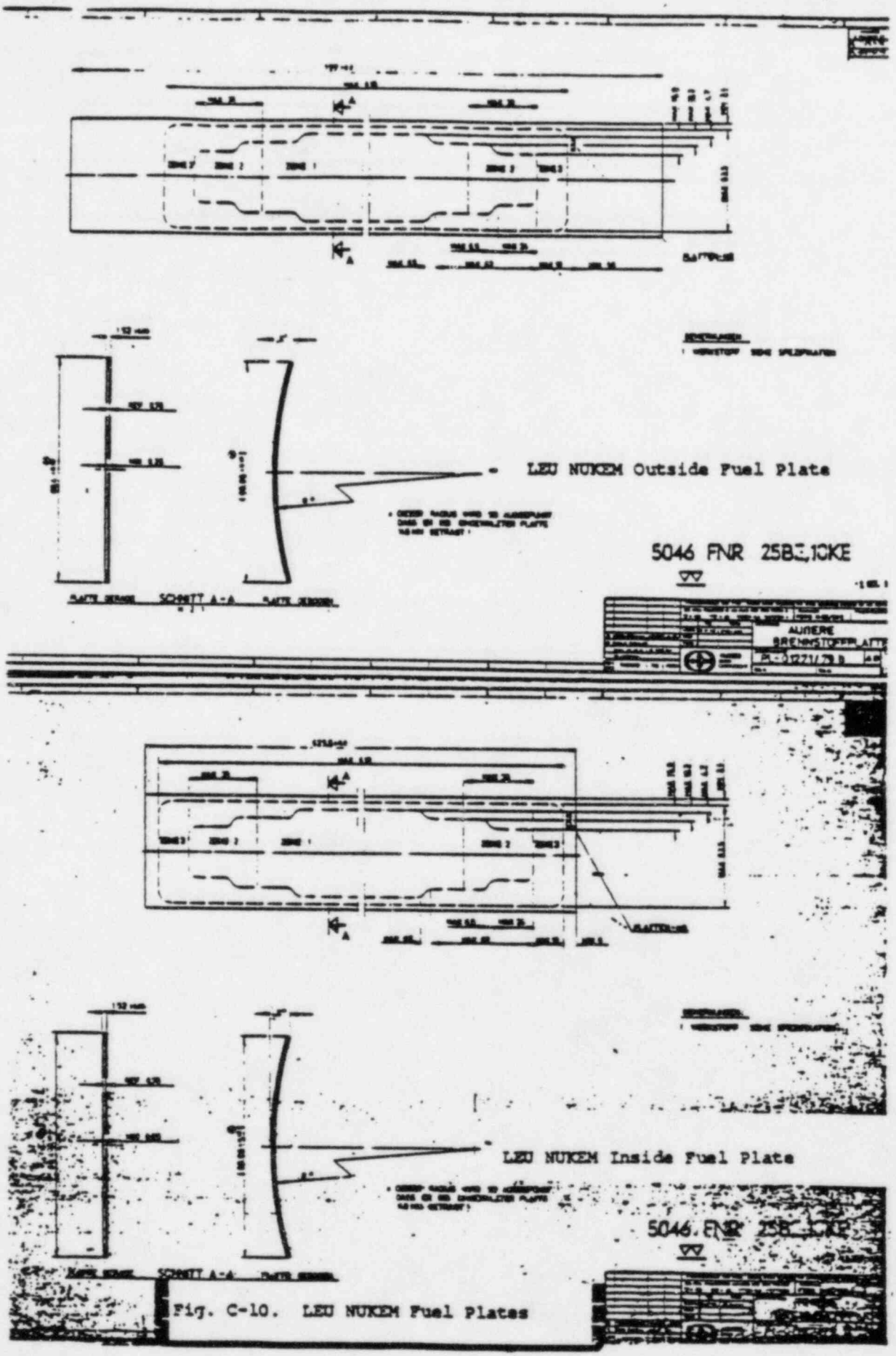

Fig. C-10. LEU NUKEM Fuel Plates

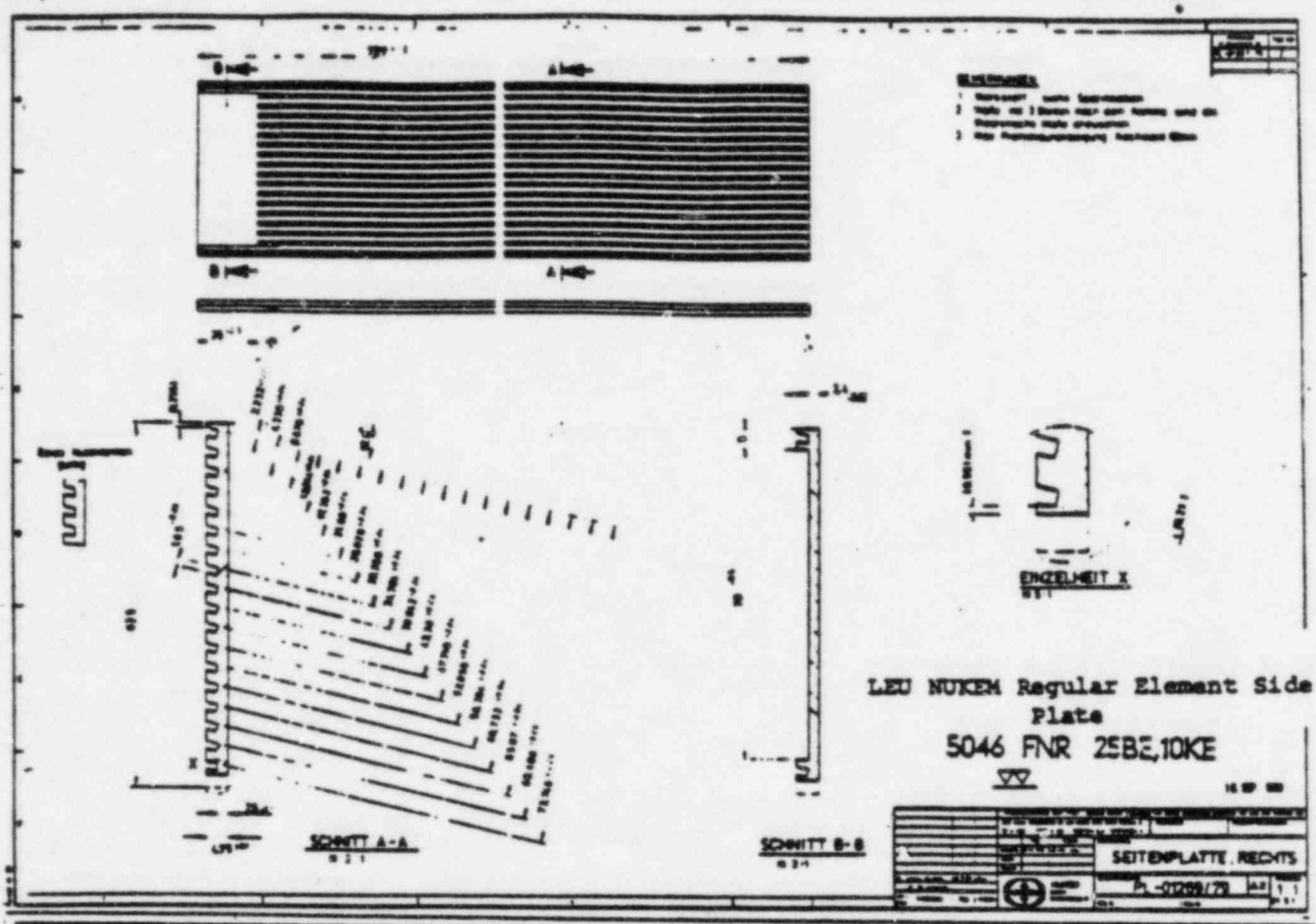

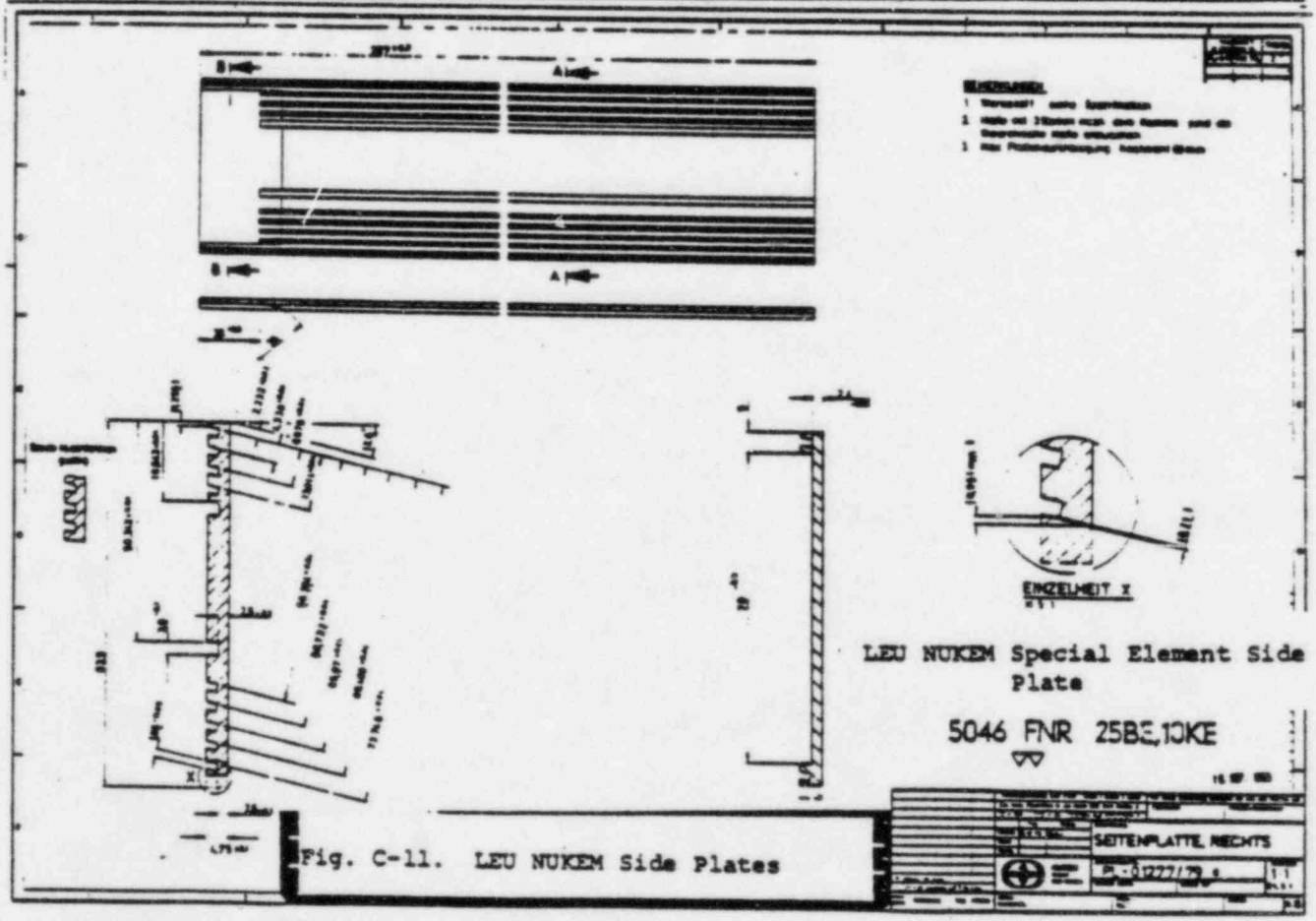

Fig. C-11. LEU NUKEM Side Plates

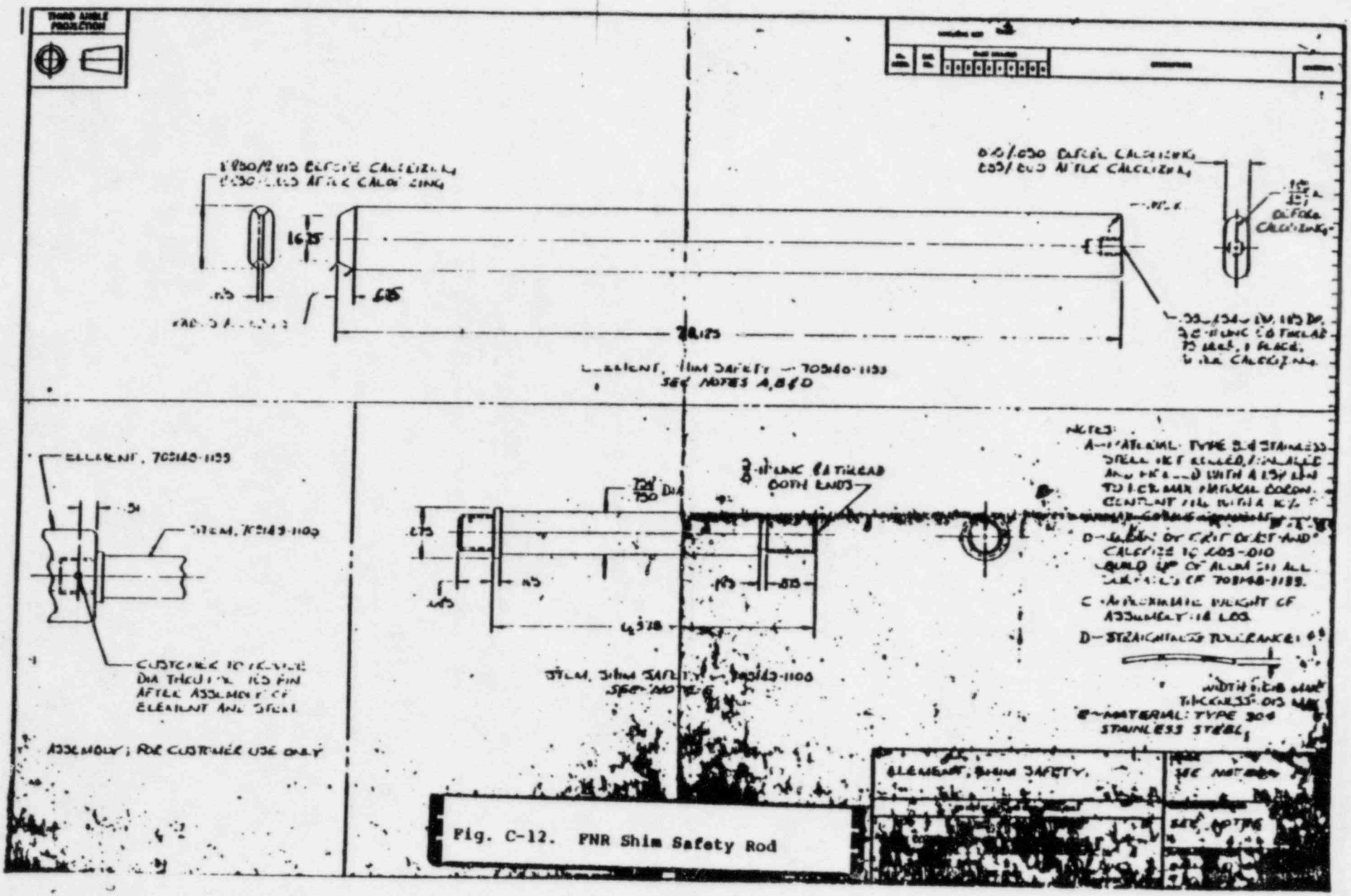

Fig. C-12. PNR Shim Safety Rod

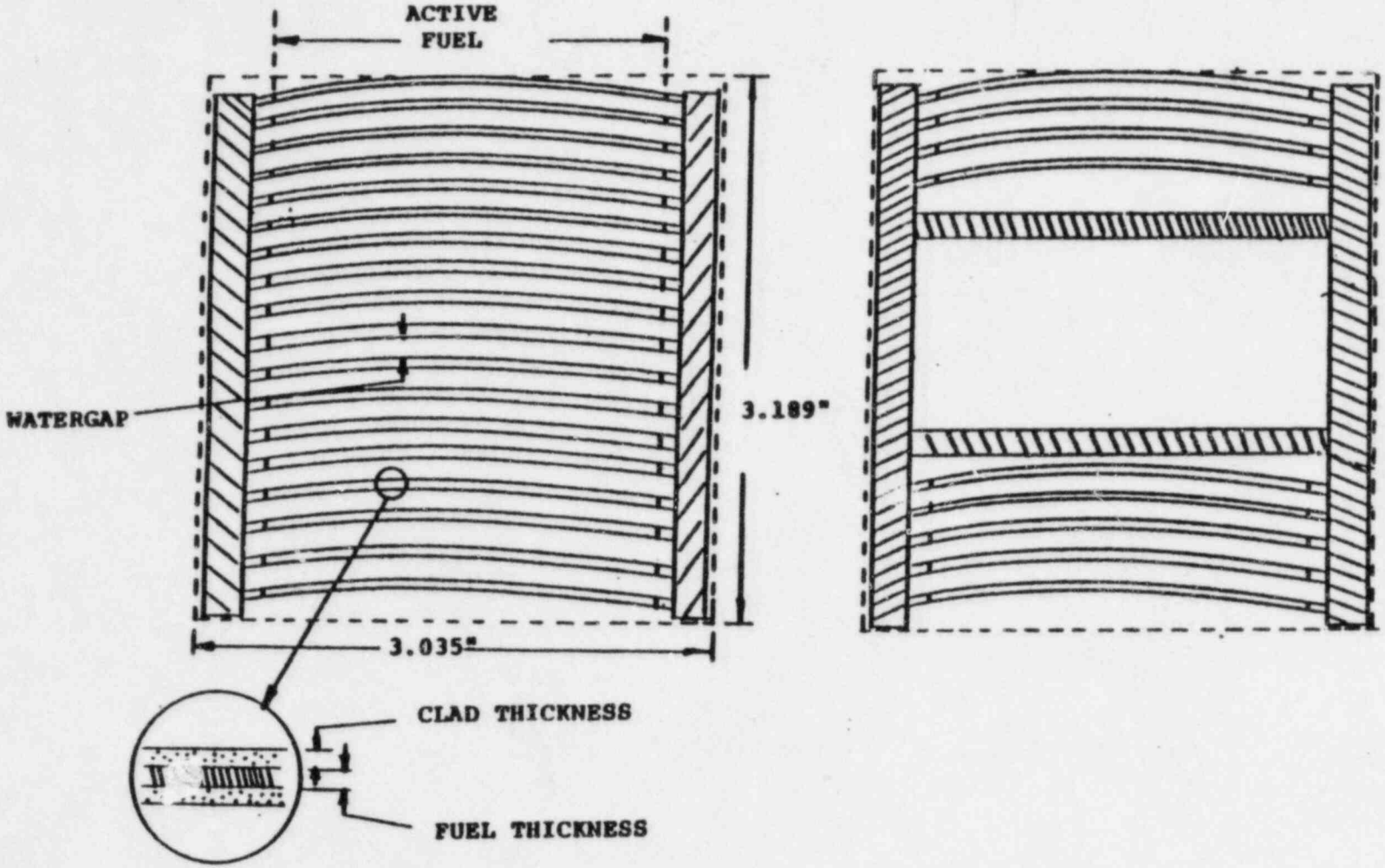

Fig. C-13. PNR Fuel Element Schematics

Table C-1.

FNR Shim Safety Rod Geometry and Composition

composition	boron stainless steel, 1.5 w/o natural boron
number densities*	(10^{24} atoms/cm^3)
10_B	.001108
11_B	.005184
Fe	.05644
Ni	.0113
Cr	.0164

*based on composition and density of boron stainless steel from:

W. K. Anderson, R. L. Eichinger, R. A. Harlow, and G. J. Cosgrove, "Boron-Stainless Steels", Neutron Absorber Materials for Reactor Control, W. K. Anderson and J. S. Theilacker, Eds., p. 235-269 U.S. Gov. Printing Office (1962).

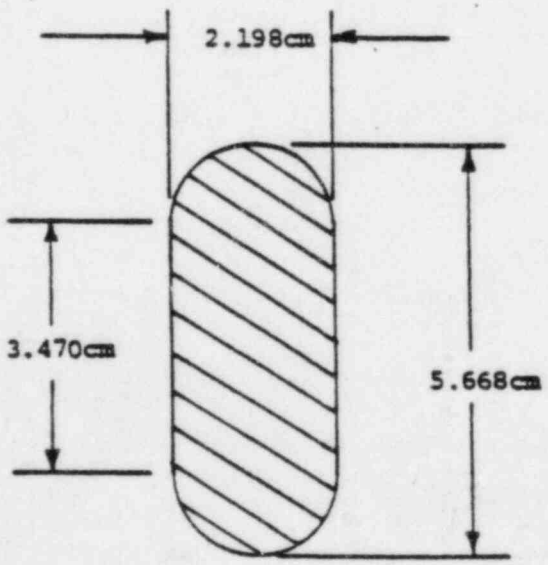

Table C-2. FNR Fuel Element Dimensions and Composition

	HEU Alloy Regular[1]	HEU Alloy Special	HEU Dispersion Regular[2]	Penn State Regular	LEU Regular	LEU Special
Fuel Meat Length (in)	23.5[3]	23.5[3]	23.0[3]	23.5[4]	23.5[4]	23.5[4]
Fuel Meat Width[5]	2.40[3]	2.40[3]	2.26[3]	2.40[4]	2.40[4]	2.40[4]
Fuel Meat Thickness[6]	.022	.022	.025	.022	.032	.032
Water Gap	.115[7]	.115[7]	.122[7]	.257	.115[4]	.115[4]
Clad Thickness[8]	.020	.020	.015	.020	.015	.015
Unit Cell Thickness[9]	.177	.177	.177	.319	.177	.177
Fuel Plates	18	9	18	10	18	9
Side Plate Width[3]	3.170	3.170	3.180	3.126	3.180	3.180
Side Plate Thickness[3]	.189	.189	.189	.1875	.189	.189
Side Plate to Plate Spacing[4]	2.562	2.562	2.564	2.614	2.564	2.564
Fuel Curvature Radii[3]	5.5	5.5	5.5	5.5	5.5	5.5
Special Guide Plate Width[4]	---	2.562	---	---	---	2.564
Special Guide Plate Thickness[4]	---	.125	---	---	---	.125
Fuel Meat Composition (gm)						
^{234}U	140.61[10]	69.86[10]	139.89[10]	166.79	167.3[11]	83.65[11]
^{235}U	1.51	.75	.82	1.79	.00	.00
^{236}U	.75	.38	.63	.80	.00	.00
^{238}U	8.04	4.00	8.68	9.54	691	345
Aluminum	908	451	878	434	1180	590
Iron	3.7	1.8	3.6	1.7	8.2	4.1
Weight % Uranium in Fuel Meat[12]	14.2%	14.2%	14.85%	29.1%	42.0%	42.0%
Cross Sectional Areas(in^2)						
Total Element[4]	9.666	9.666	9.666	9.666	9.666	9.666
Lattice	7.654	3.827	7.207	7.654	7.654	3.827
Non-Lattice	2.012	5.840	2.459	2.012	2.012	5.840
Metal in Non-Lattice[12]	1.381	1.930	1.510	1.305	1.374	1.924
Water in Non-Lattice	~~.664~~ 631	3.910	.949	.707	.638	3.916

1. FNR core grid spacing is 3.188" x 3.035"
2. New regular fuel elements added to the FNR core after December 4, 1978 were dispersion fuel elements. The last alloy regular fuel elements are expected to be discharged from the core during the summer of 1981. As of April 1981 no dispersion special elements have been placed in the core, although a few of these elements are on site.
3. Fuel plate dimensions measured from radiographs of 7 alloy and 17 dispersion fuel plates.
4. Dimensions chosen to be consistent with HEU regular fuel element data.
5. Fuel meat width is for a flat fuel plate.
6. Fuel meat thickness calculated as: unit cell thickness - 2 x clad thickness - water gap e.g. HEU alloy, .177" - 2 x .020" - .115" = .022"
7. Water gap width averaged from vendor measurements of the actual fuel plate spacing.
8. Data represents the nominal dimension on vendor drawings.
9. Unit cell thickness calculated as: FNR grid spacing/ number of fuel plates e.g. HEU alloy, 3.189"/18= .177"
10. Uranium mass taken from vendor measurement data.
11. Uranium mass taken from fuel specifications.
12. Modeling trace elements in the aluminum alloy is important.

Table C-3.

Chemical Composition of Aluminum Alloys Used in Fuel Element Manufacture by United States, French (CERCA), and German (NUKEM) Suppliers

	Fuel Core Powder				Fuel Plate Covers			Fuel Element Structure		
Maximum Percentage or Alloy Range	1100 (US)	5214 (US)	A5NE (CERCA)	(NUKEM)	6061 (US)	AG2NE (CERCA)	AL-MG-1 (NUKEM)	6061 (US)	AG3NE (CERCA)	AL-MG-Si-1 (NUKEM)
Al_2O_3	-	-	-	.70	-	-	-	-	-	-
Boron	-	.001	.001	.001	-	.001	.001	-	.001	.001
Cadmium	-	.002	.001	.001	-	.001	.001	-	.001	.001
Chromium	-	-	-	-	.15-.35	-	.10	.15-.35	-	.25
Cobalt	-	-	-	.001	-	-	.003	-	-	.003
Cooper	.20	.20	.008	.008	.15-.40	.008	.008	.15-.40	.008	.05
Iron	-	.05	.40	.20-.40	.70	.20-.40	.45	.70	.20-.40	.50
Lithium	-	.008	.001	.001	-	.001	.001	-	.001	.001
Magnesium	-	-	-	.015	.80-1.2	1.8-2.3	.70-1.1	.80-1.2	2.5-3.0	.60-1.2
Manganese	.05	-	-	-	.15	-	.15	.15	-	.40-1.0
Oil and Grease	-	-	-	.20	-	-	-	-	-	-
Silicon	-	-	.30	.30	.40-.80	.30	.30	.40-.80	.30	.70-1.3
Silcon and Iron	1.0	.25	.50	-	-	.20-.50	-	-	.20-.50	-
Titanium	-	-	-	.02	.15	-	-	.15	-	.10
Volatiles	-	-	-	.10	-	-	-	-	-	-
Zinc	.10	.10	.03	.03	.25	.03	.05	.25	.03	.05
Others	.15	0.0	.03	0.0	.15	.03	.15	.15	.03	.15
Minimum Percentage										
Aluminum	99.0	99.7	99.4	98.5	Remainder			Remainder		

Table C-4.

Two-Group Cross Sections
Generated with the LEOPARD Code

Grp (g)	Fissile Depletion	Σ_f	Σ_a	$\nu\Sigma_f$	Σ_{tr}	$\Sigma_{s1\to2}$
		TABLE FORMAT				
		LIGHT WATER REFLECTOR				
1	--	0.0	8.691-4	0.0	2.776-1	
2	--	0.0	1.853-2	0.0	2.112	5.267-2
		HEAVY WATER REFLECTOR				
1	--	2.729-4	4.698-4	5.478-4	1.803-1	
2	--	0.0	6.651-5	0.0	3.075-1	5.466-3

HEU DISPERSION REGULAR FUEL ELEMENTS

1	0.00%	8.629-4	2.074-3	2.109-3	2.328-1	
2		3.965-2	6.099-2	9.670-2	1.225	2.710-2
1	0.10%	8.651-4	2.080-3	2.114-3	2.323-1	
2		3.949-2	6.220-2	9.630-2	1.2235	2.725-2
1	10.00%	7.876-4	2.055-3	1.923-3	2.311-1	
2		3.590-2	5.918-2	8.756-2	1.2285	2.762-2
1	20.00%	7.074-4	2.023-3	1.728-3	2.299-1	
2		3.226-2	5.554-2	7.868-2	1.234	2.796-2

HEU ALLOY REGULAR FUEL ELEMENTS

1	0.00%	8.512-4	2.066-3	2.079-3	2.305-1	
2		3.890-2	6.000-2	9.487-2	1.163	2.574-2
1	0.10%	8.533-4	2.072-3	2.084-3	2.300-1	
2		3.874-2	6.119-2	9.448-2	1.1611	2.588-2
1	10.00%	7.771-4	2.047-3	1.900-3	2.290-1	
2		3.522-2	5.823-2	8.590-2	1.1660	2.623-2
1	20.00%	6.981-4	2.016-3	1.706-3	2.279-1	
2		3.164-2	5.466-2	7.719-2	1.172	2.656-2

HEU ALLOY SPECIAL FUEL ELEMENTS

1	0.00%	4.454-4	1.462-3	1.085-3	2.320-1	
2		1.858-2	3.750-2	4.530-2	1.374	3.169-2
1	0.10%	4.458-4	1.465-3	1.086-3	2.315-1	
2		1.852-2	3.803-2	4.517-2	1.373	3.179-2
1	18.00%	3.717-4	1.443-3	9.034-4	2.280-1	
2		1.538-2	3.525-2	3.750-2	1.379	3.245-2
1	36.00%	2.951-4	1.416-3	7.147-4	2.294-1	
2		1.216-2	3.192-2	2.966-2	1.386	3.317-2

LEU REGULAR FUEL ELEMENTS

1	0.00%	1.056-3	3.622-3	2.606-3	2.315-1	
2		4.544-2	6.812-2	1.108-1	1.157	2.472-2
1	0.10%	1.059-3	3.634-3	2.613-3	2.310-1	
2		4.524-2	6.946-2	1.103-1	1.155	2.487-2
1	10.00%	9.706-4	3.633-3	2.401-3	2.299-1	
2		4.143-2	6.652-2	1.013-1	1.161	2.518-2
1	20.00%	8.794-4	3.636-3	2.180-3	2.289-1	
2		3.749-2	6.284-2	9.201-2	1.167	2.538-2

LEU SPECIAL FUEL ELEMENTS

1	0.00%	5.562-4	2.275-3	1.370-3	2.337-1	
2		2.198-2	4.167-2	5.360-2	1.366	3.078-2
1	0.10%	5.569-4	2.280-3	1.371-3	2.332-1	
2		2.191-2	4.233-2	5.343-2	1.365	3.089-2
1	18.00%	4.702-4	2.272-3	1.159-3	2.300-1	
2		1.832-2	3.925-2	4.482-2	1.372	3.152-2
1	36.00%	3.806-4	2.271-3	9.426-4	2.276-1	
2		1.461-2	3.549-2	3.589-2	1.379	3.219-2